Test of Feasibility of a Novel High Precision Test of Time Reversal Invariance

Dissertation

zur

Erlangung des Doktorgrades (Dr. rer. nat.)

der

Mathematisch–Naturwissenschaftlichen Fakultät

der

Rheinischen Friedrich–Wilhelms–Universität Bonn

vorgelegt von

Deepak Samuel

aus

Chennai, Indien.

Bonn 2007

Abstract

The first results of a feasibility test of a novel high precision test of time reversal invariance are reported. The Time Reversal Invariance test at COSY (TRIC) was planned to measure the time reversal violating observable $A_{y,xz}$ with an accuracy of 10^{-6} in proton-deuteron (p-d) scattering. A novel technique for measuring total cross sections is introduced and the achievable precision of this measuring technique is tested. The correlation coefficient $A_{y,y}$ in p-d scattering fakes a time-reversal violating effect. This work reports the feasibility test of the novel method in the measurement of $A_{y,y}$ in p-p scattering. The first step in the experimental design was the development of a hard real-time data acquisition system. To meet stringent latency requirements, the capabilities of Windows XP had to be augmented with a real-time subsystem. The remote control feature of the data acquisition enables users to operate it from any place via an internet connection. The data acquisition proved its reliability in several beam times without any failures. The analysis of the data showed the presence of 1/f noise which substantially limits the quality of our measurements. The origin of 1/f noise was traced and found to be the Barkhausen noise from the ferrite core of the beam current transformer (BCT). A global weighted fitting technique based on a modified Wiener-Khinchin method was developed and used to suppress the influence of 1/f noise, which increased the error bar of the results by a factor 3. This is the only deviation from our expectations. The results are presented and discussed.

Contents

1 Introduction

Symmetries play an important and fundamental role in physics. It was not before 1917 that the profound implications of symmetries were understood when Emmy Noether published her famous theorem. It states that all symmetries yield a conservation law and vice-versa. A symmetry can be defined to be a mathematical operation that leaves a system invariant, a state that is indistinguishable from the original. In the standard model, the symmetries charge conjugation (C), parity transformation (P) and time reversal (T) are linked through the CPT theorem. The CPT theorem states that the product of the symmetries C, P and T is invariant [1]. Though the product of these symmetries (CPT) is invariant, individual violations of these symmetries are found in nature [2][3]. Parity violation was first seen in the beta decay experiment of C.S Wu et al.[4]. Later, CP violation was discovered by Gell-Man and Pais in the neutral kaon system[5]. CP or T violation is a necessary condition for the explanation of the predominance of matter over anti-matter and thus, our very own existence [6][7]. CP violation is accommodated in the standard model by the δ parameter in the Cabibbo-Kobayashi-Maskawa (CKM) matrix. Various tests of CP violation have been carried out so far by measuring the electric dipole moment (edm) of the neutron, the electron and atoms[8][9][10]. A non-zero edm is a sign of CP violation. Due to CPT invariance, a violation of CP implies the violation of T and vice-versa. The first direct evidence for time-reversal violation was also found in the neutral kaon system [11].

The origin of CP or T violation is not clear and this necessitates further tests of CP or T invariance [12]. In this context, further studies of T invariance are needed for the following reasons:

(a) The origin of the processes that contribute to T violation is not well understood.

(b) For a system to possess a permanent edm, P and T must be violated simultaneously and so edm experiments do not yield an unique T violation signal [13][14].

(c) The δ parameter in the CKM matrix explains only the P odd violations of CP [15]. So far no experimental evidence has been found for a P even CP violation. Therefore, it is interesting to search for time reversal invariance (TRI) in P even T odd reactions.

A P even, T odd nucleon-nucleon interaction is mediated by a $J \neq 0$ single meson exchange (e.g., $\rho^{\pm}, a_1$ etc.,)[16]. A theoretical upper bound on the P-even/T-odd ρNN coupling strength Φ_ρ is given from the analysis of edm measurements as $1 \cdot 10^{-3}$[17].

In general, tests of TRI in nuclear reactions are carried out by comparing the observables like cross section in the "time-forward" reaction with those in the "time-reversed" reaction. These types of experiments face considerable difficulty in instrumentation and also in relative normalization of the two measurements. Even in the case of self-conjugate reactions, in which the forward reaction is equal to the inverse reaction, time reversal constraints equate two different observables in the forward and inverse reaction. For example, in proton-proton (p-p) elastic scattering, the analysing power A is equal to the polarizing power P [18].

Due to the problems mentioned above, TRI tests have rarely reached accuracies better than 1%. On the other hand, null tests of parity conservation have been conducted with very high precision (in the order of 10^{-8})[19]. Thus one can expect that a null test for TRI would enhance the experimental precision by several orders of magnitude.

The proposed Time Reversal Invariance experiment at COSY (TRIC) is a P even T odd null test of TRI. The experiment intends to measure the TRI violating observable $A_{y,xz}$ in proton-deuteron forward scattering with an accuracy of 10^{-6}. This accuracy is compatible to the theoretical upper bound from edm measurements mentioned earlier.

The initial set up for the experiment and the following progress with regard to data acquisition and the analysis of the data acquired thereof is the main focus of this thesis work. The work also presents a novel method to measure total cross sections and reports the first results of the test of feasibility of the TRIC experiment in a measurement of $A_{y,y}$ in p-p scattering. The achievable accuracy and the limitation with respect to noise of this novel measuring technique is presented. The work is organised as follows:

- The foundations of the experiment and the figure of merit is discussed in the following chapter.

- In Chapter 3, the experimental part namely the measurement of the figure of merit, the accuracy of the experiment and the experimental needs are discussed.

- Chapter 4 focuses on the experimental setup wherein the design and concepts of the data acquisition are discussed.

- The analysis of the data acquired during the alloted beam time is discussed in Chapter 5.

- The results are summarized finally.

2 Foundations of the TRIC Experiment

2.1 Null Tests of Symmetry Violations

Time reversal invariance tests in nuclear systems have never been able to achieve the precision that null tests of parity violation could achieve. This is attributed to the fact that there exists a proof of non-existence of null tests in T violating reactions with two particles in and two particles out, as long as bilinear amplitudes like differential cross sections are involved[20]. However, total cross section observables were not explicitly included in this proof.

Usually, in a time reversal invariance (TRI) test, an observable in the forward reaction is compared with a different observable in the inverse reaction[18]. Often, one of these is difficult to measure with high precision which has constrained the precision of TRI tests. On the other hand, the parity violation tests have achieved remarkable precision in the measurement of the parity non-conserving (PNC) observable. This is largely due to the existence of null tests of parity. In a null test of parity conservation (PC), one compares an experimental observable in a process to the same observable in the mirrored reaction. Thus any P odd observable should vanish for a parity conserving (PC) reaction. Since only one observable is measured the effect of systematic errors is minimal. Especially for polarization observables one can test for systematic errors by switching off the polarization.

H.E Conzett could prove the existence of TRI null tests using the optical theorem because the total cross section asymmetry is non-bilinearly related to a T odd amplitude in forward scattering[21]. In tests of symmetry violations, one prefers the use of polarization observables since a plethora of experiments are possible via the polarization observables. A suitable experiment is chosen such that the influence of competing observables faking the symmetry violation is minimal. A brief account of polarization observables and their properties with respect to symmetries can be found in Appendix A. A possibility of existence of vanishing P-even T-odd observable in forward elastic scattering in polarized nuclear systems with spin structures of the form $\frac{1}{2} + \frac{1}{2} \rightarrow \frac{1}{2} + \frac{1}{2}$ and $1 + \frac{1}{2} \rightarrow 1 + \frac{1}{2}$ are discussed in the following sections.

2.2 Spin Structure of the Form $\frac{1}{2} + \frac{1}{2} \rightarrow \frac{1}{2} + \frac{1}{2}$

The transition matrix M connects the initial spin states X_i to the final spin states X_f such that $X_f = MX_i$. The transition matrix can be expanded in terms of direct product of Pauli spin matrices σ_j and σ_k and can be written as [18]:

$$M(\theta) = \sum_{j,k} a_{j,k}\sigma_{j,k}, \quad j,k = 0, x, y, z \tag{2.1}$$

The projectile helicity frame is used here wherein the coordinate axes are taken to be:

$$\mathbf{z} = \mathbf{k_i}, \ \mathbf{y} = \mathbf{k_i} \times \mathbf{k_f}, \ \mathbf{x} = \mathbf{y} \times \mathbf{z} \tag{2.2}$$

where $\mathbf{k_i}$ and $\mathbf{k_f}$ are along the initial and final momenta of the projectile and where $\sigma_{jk} = \sigma_j \otimes \sigma_k$, is a 4 x 4 matrix and the 16 invariant matrix amplitudes are:

$$a_{0,0},\ a_{0,x},\ a_{0,y},\ a_{0,z},\ a_{x,0},\ a_{x,x},\ a_{x,y},\ a_{x,z},$$
$$a_{y,0},\ a_{y,x},\ a_{y,y},\ a_{y,z},\ a_{z,0},\ a_{z,x},\ a_{z,y},\ a_{z,z}, \tag{2.3}$$

In forward scattering ($\theta = 0$), the corresponding forward-scattering matrix M(0) is invariant under rotations about the z axis. The terms which remain in the matrix M after imposing the symmetry conditions described in Appendix A are:

$$\begin{aligned} M(0) =& a_{0,0} + a_{0,z}\sigma_0\sigma_z + a_{z,0}\sigma_z\sigma_0 \\ &+ a_{x,x}(\sigma_x\sigma_x + \sigma_y\sigma_y) + a_{z,z}\sigma_z\sigma_z \\ &+ a_{x,y}(\sigma_x\sigma_y - \sigma_y\sigma_x) \end{aligned} \tag{2.4}$$

From Appendix A, an observable is parity non-conserving (PNC) if $n_x + n_z$ is odd and time reversal violating (TRV) if n_x alone is odd. n_j is the number of times the subscript j appears in a particular observable. In equation 2.4, the only amplitude that is odd under TRV is $a_{x,y}$, but this amplitude is also odd under PNC. Thus in this system there can be no unique P-even T-odd test of TRI. A detailed description of this system can be found in [21].

2.3 Spin Structure of the Form $\frac{1}{2} + 1 \rightarrow \frac{1}{2} + 1$

The scattering matrix in this case takes the form[18]:

$$M(\theta) = \sum_{j,k} a_{j,k}\ \sigma_j \otimes \mathbf{P}_k + \sum_{j,lm} a_{j,lm}\ \sigma_j \otimes \mathbf{P}_{lm} \tag{2.5}$$
$$j, k = 0, x, y, z; lm = xx, yy, xy, xz, yz (\text{the only independent terms})$$

where $\mathbf{P}_k$ is the vector polarization component and $\mathbf{P}_{lm}$ is the tensor polarization component as described in Appendix A. Again, imposing invariance and symmetry conditions as in the previous section, the forward scattering matrix is given by[1]

$$\begin{aligned} M(0) =& a_{0,0} + a_{0,z}\sigma_0\mathbf{P}_z + a_{z,0}\sigma_z\mathbf{P}_0 + a_{y,y}(\sigma_y\mathbf{P}_y + \sigma_x\mathbf{P}_x) + a_{z,z}\sigma_z\mathbf{P}_z \\ &+ a_{y,x}(\sigma_y\mathbf{P}_x - \sigma_x\mathbf{P}_y) + a_{0,zz}\sigma_0\mathbf{P}_{zz} + a_{z,zz}\sigma_z\mathbf{P}_{zz} \\ &+ a_{y,yz}(\sigma_y\mathbf{P}_{yz} + \sigma_x\mathbf{P}_{xz}) + a_{y,xz}(\sigma_y\mathbf{P}_{xz} + \sigma_x\mathbf{P}_{yz}) \end{aligned} \tag{2.6}$$

The relation between the total cross section and the forward scattering amplitudes is given by the optical theorem. It is only through this relation that a null test of TRI can be established in nuclear systems [20],[21]. The optical theorem is written as:

$$\sigma_{tot} = K\ Im\ Tr[\rho_{j,k}M(0)] \tag{2.7}$$

where, $K \equiv \frac{4\pi d}{k}$, d being the target density and k the wave number. $\rho_{j,k}$ is the direct product density matrix of the initial polarization and M is the forward scattering matrix described in equation 2.6. The direct product density matrix contains information about the population of the sub-states of the circulating beam and the target in COSY. Using

---

[1]The generalized Pauli principle requires an equality of experiments related by interchanging beam with target states and momenta[22]. Thus for a general pure experiment, $a_{pq} = -1^{[x][z]}a_{qp}$, with [j] being the number of times the superscript j appears in an observable.

the symmetry conditions in Appendix A, the only PC and TRV amplitude in equation 2.6 is $a_{y,xz}$. In elastic scattering, where the inverse reaction is equal to the forward reaction, this amplitude vanishes. The relationship between this amplitude and the measurable quantity, namely the figure of merit of our experiment is discussed below. The total cross section can be written in terms of the analyzing powers and the spin correlation coefficients as follows [23]:

$$\sigma_{tot} = \sigma(1 + \sum_j p_j A_j + \sum_k p_k^T A_k^T + \sum_{j,k} p_j p_k A_{j,k})$$

(2.8)

$$j = x, y, z; k = x, y, z, xx, yy, xy, xz, yz, zz$$

Where A_j is the analysing power and $A_{j,lm}$ are the spin correlation coefficient. The superscript T refers to the target analysing power. σ is the unpolarized cross section. Since $a_{y,xz}$ is the amplitude of interest, the target tensor polarization is aligned to be at 45° with respect to the x and z axis and the beam polarization to be along the y direction (cf. Fig 2.1). If the cross section for which the beam polarization is p_y $(-p_y)$ is denoted by σ_{tot}^+ (σ_{tot}^-) then, the relative difference between these cross sections after canceling quantities that are rotationally invariant and noting that $p_x = p_z = 0$ is:

$$\frac{\sigma_{tot}^+ - \sigma_{tot}^-}{\sigma_{tot}^+ + \sigma_{tot}^-} = (\frac{3}{2}p_y p_y^T A_{y,y} + \frac{3}{2}p_y p_x^T A_{y,x}$$

(2.9)

$$+ \frac{2}{3}p_y p_{yz}^T A_{y,yz} + \frac{2}{3}p_y p_{xz}^T A_{y,xz})$$

The factors in equation 2.9 are due to the normalisation of spin 1 operators [23]. If we
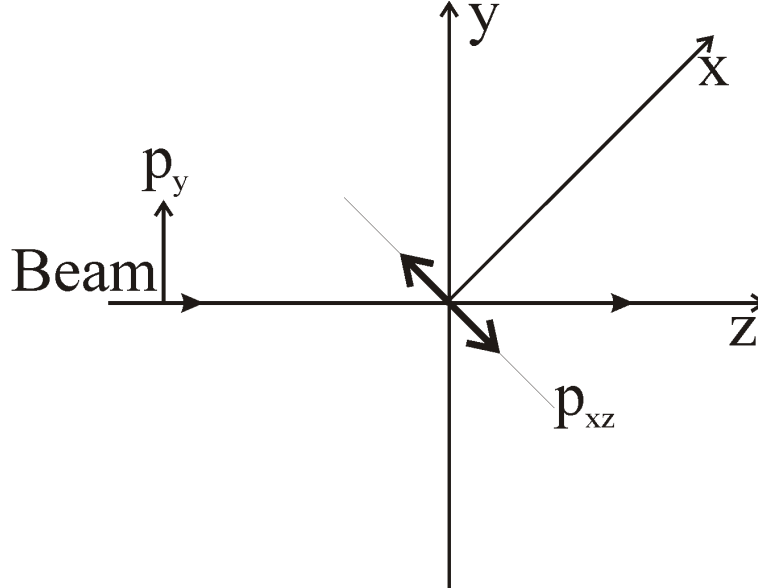
Figure 2.1: The polarization setup for the determination of the spin-correlation coefficient. The beam is polarized in the y direction and passes along the z direction. The target tensor polarization is aligned at 45 degrees with respect to the x and z axis.

assume the quantities other that $A_{y,xz}$ in equation 2.9 to be zero, the reason for which will be stated in the next chapter, and relate this observable to the forward scattering matrix

amplitudes through the optical theorem, we get,

$$A_{y,xz} = \frac{3}{4}(Im\ a_{y,xz}/Im\ a_{0,0}) \qquad (2.10)$$

Thus the figure of merit and the observable of interest for a P even T odd null test of TRV
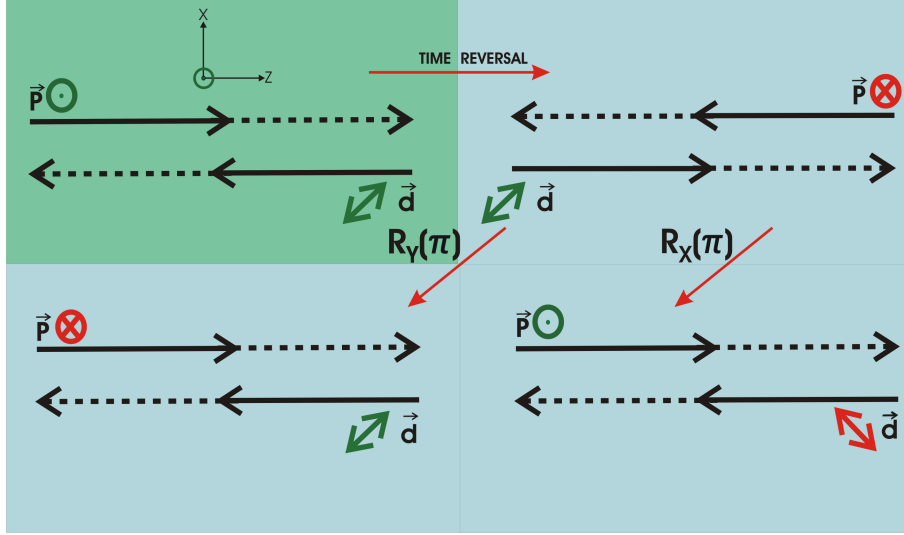
Figure 2.2: Time reversal corresponds to flipping of the spin of the proton beam or deuteron target alignment. The block with the green background represents the reaction in the "time-forward" world and the others represent the same reaction in the "time-reversed" world.

is $A_{y,xz}$. This is also the result if one would consider the flipping the target alignment instead of the beam polarization. This is shown in figure 2.2. The figure depicts the p-d scattering in the CM frame. In the normal world (shown in green background), a vector polarized (along the y direction) proton beam from the left reacts with a tensor polarized (along x=z direction) deuteron target from the right. In the time-reversed world, the momentum vectors change direction. The tensor polarization does not change, though the vector polarization changes. A rotation of the system about the x or the y axis through 180° leaves the system identical to the normal world in terms of momentum. Thus the flipping of either the target tensor alignment or the beam vector polarization corresponds to the time reversed world. The simplest hadronic system in this configuration is the proton-deuteron system.

A recent experiment of this kind has been reported in the literature[24]. Gould *et al.* have measured this spin correlation coefficient using a polarized neutron source transmitted through a rotating, cryogenically aligned,[165]Ho target. The precision of the result is orders of magnitude higher than previous experiments. But, the accuracy of this experiment is limited due the tensor polarization in the [165]Ho target which is given by the single valence nucleon only. Thus the effect is diluted by the other 164 nucleons. This drawback is minimized in the TRIC experiment since vector polarized protons scatter off a tensor polarized deuteron target.

Measurement	Remarks	Violated Symmetry
EDM of the neutron	$g_{PT} \leq 10^{-11}$[8]	PT
$\gamma - \gamma$ correlation in ^{57}Fe	$\alpha_T \leq 5 \cdot 10^{-6}$[25, 26]	T
P-A in p-p scattering	$g_T \leq 3 \cdot 10^{-2}$[27]	T
Detailed balance in		
p + ^{27}Al$\leftrightarrow$ ^{4}He + ^{24}Mg	$\alpha_T \approx g_T \leq 10^{-3}$[28]	T
n-transmission through ^{139}La	Hope for enhancement[29]	PT
n-rotation in ^{139}La	Enhancement$\approx 10^{-5}$[30]	P
A_z in p-p scattering	Error $(A_z) \approx 2 \cdot 10^{-8}$[19]	P
A_5 in n-transmission through^{165}Ho	$\alpha_T \leq 7.1 \cdot 10^{-4}$[24]	T
$A_{y,xz}$ in p-d scattering	TRIC	T

Table 2.1: Comparison of tests of P and T violations. g: strength of T-odd NN potential, α: strength of an effective T-odd N-core potential.

3 The Experiment

The TRIC experiment intends to measure the P even, T odd TRV observable - the figure of merit $A_{y,xz}$ - with an accuracy of 10^{-6}. The experiment was planned to be run at the Cooler Synchrotron (COSY) at the Research center in Juelich. As discussed in the previous chapter, the figure of merit is the relative difference between the cross section for the two different proton polarization states $p_y = \pm 1$. This is also equivalent to flipping the alignment of the deuteron target. In this respect, the figure of merit is proportional to the asymmetry in the total cross section measured in the normal and the time-reversed world.

3.1 The TRI Faking Observable

The figure of merit is directly related to the total cross section as given in equation (2.9). In that equation one finds that the difference of the cross section involves not only the figure of merit but also other extra terms which are not the observables of interest. They are $A_{y,x}$, $A_{y,yz}$ and $A_{y,y}$. Amongst these terms $A_{y,x}$ and $A_{y,yz}$ are parity violating observables since $n_x + n_z$ is odd. These quantities are expected to be in the order of 10^{-7} for simple nuclear systems and thus can be neglected for the intended accuracy of the TRIC experiment. The only other term in the cross section is $A_{y,y}$ which can fake a TRI effect in our experiment and can be measured the same way as $A_{y,xz}$. The first stage of the experiment is to measure $A_{y,y}$ since its value in the energy range of the TRIC experiment is not known. The TRIC experiment is set up in a way that the measurement of $A_{y,y}$ also gives information about the feasibility of the achievable accuracy in the measurement of $A_{y,xz}$. The target is polarized in the y=y direction so that the resulting cross section corresponding to equation (2.8) is:

$$\sigma_{tot} = \sigma(1 + \frac{3}{2}p_y A_y + \frac{1}{2}p_{yy}^T A_{yy}^T + p_y^T A_y^T + \frac{3}{2}p_y^T p_y A_{y,y} + \frac{1}{2}p_{yy}^T p_y A_{yy,y}) \qquad (3.1)$$

with σ_{tot} being the total polarized cross section, σ being the total unpolarized cross section. In the above equation, imposing rotational invariance condition as discussed in Appendix A, all the terms with odd number of y subscripts cancel. The only remaining terms are A_{yy} and $A_{y,y}$. A_{yy} and σ can be measured by using a unpolarized proton beam and flipping the target holding field. $A_{y,y}$ can then be measured by using a polarized proton beam and flipping the proton polarization [31]. This is similar to the method followed in arriving at equation 2.9.

In the present work, the feasibility of the TRIC experiment is tested in the measurement of $A_{y,y}$ in p-p scattering by comparing it with the existing results.

3.2 The Novel Technique to Measure Total Cross Sections

In general, the measurement of total cross section is rendered to a scattering experiment. The usual methods to measure total cross section are:

- Measure all particles which are scattered off the target at all energies and in all directions.

- Utilize the Optical Theorem to determine the total cross section from the forward scattering amplitude i.e, measure the number of particles that remain in the beam after scattering.

The first method suffers from the disadvantage that the detector has to be calibrated with respect to various conditions (eg. energy, particle type). The second method requires the measurement of the forward scattering amplitude which is made by measuring the number of scattered particles along the forward direction (i.e, $\theta = 0$). This can be done in two ways. The scattered particles in an infinitesimally small solid angle around zero are measured, in which case the detector should have a small acceptance and the experiment suffers from low count rates. The other possibility is by opening up the solid angle and measuring the differential cross section in the neighborhood of zero scattering angle and calculating the forward scattering amplitude by analytical continuation. This method requires high statistics to keep the resulting errors small. In all these methods, the situation is even more complicated in case the scattering involves polarized particle in which the count rates are not rotationally symmetric and consequently the detector has to be calibrated for every solid angle element (cf. Fig 3.1).

3.2.1 Comparison of External and Internal Targets in Total Cross Section Measurements

Scattering experiments can be classified into external target experiments and internal target experiments. External target experiments need to use thick targets to increase the luminosity which might increase the probability of multiple scattering and can lead to systematic errors. Also, external target experiments are "one- chance" experiments since the beam interacts only once with the target. On the other hand, internal target experiments can afford to have thin targets due to the high revolution frequency of the beam. The beam particle suffers only one interaction in such a target which allows a high accuracy in detection of the energy loss and scattering angle. Further, the interaction between the beam and the target is not an "one-chance" process as any particle in the beam that has not interacted yet has another chance in the next turn when it passes through the target (cf. Fig 3.2). Internal target experiments do not require special calibration as the total cross section is measured from the remaining particles in the beam. The TRIC experiment is an internal target experiment. The measurement of the total cross section is made by measuring the number of particles that remain in the beam (i.e., forward scattering) after interacting with the target. The transmission factor T is defined to be the ratio of the current I_n after passing n times through a target of thickness d and density ρ to the initial current I_0 i.e.,

$$T = \frac{I_n}{I_0} = \exp\left(-\sigma_{tot} n \rho d\right) \tag{3.2}$$

where, σ_{tot} is the total cross section.

The total cross section is thus related to the slope of the current. This is a novel technique to measure total cross sections. The measurement of the slope is rendered to a current measuring device. Thus, apart from the dynamical parameters of the experiment, the accuracy depends ultimately on the precision of this current measuring device.
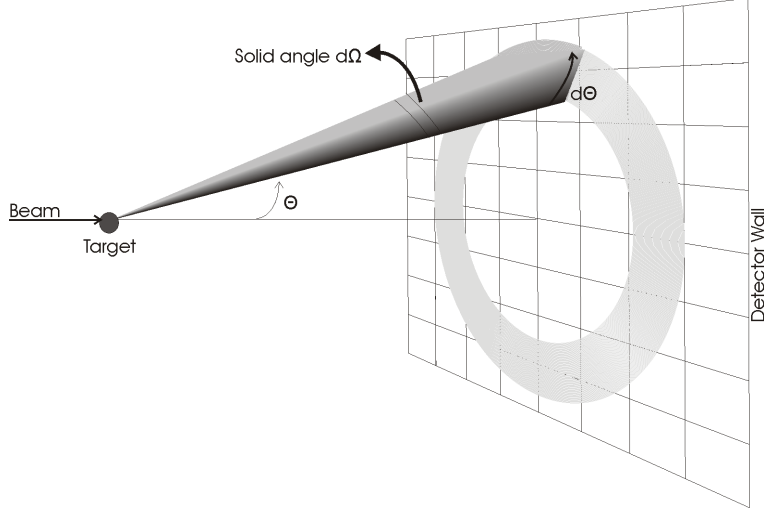
Figure 3.1: Measurement of cross section using an external target. This is an "one-chance" experiment. The detectors need special calibration with respect to particle type, energy and direction and the detector response has to be known for each solid angle element in the case of polarized particles.

3.3 Accuracy of the Figure of Merit

An estimate of the the achievable accuracy of the figure of merit from the first principles in presented in this section. The figure of merit $A_{y,xz}$ is measured in a transmission experiment. In a typical measurement, the polarized proton beam is injected into the COSY ring and is accelerated to the desired energy. The atomic beam source is switched on to give a pure tensor polarized (x=z) deuteron target. The slope of the current is determined during this period and finally the beam is decelerated and dumped. In the next cycle the beam polarization or the target alignment is flipped and the loss rate is determined once again. The relation between the beam current I_n after a time t and the initial current I_0 is also given by the equation,

$$I_n = I_0 \exp\left(\frac{-t}{\tau}\right) \tag{3.3}$$

where τ is the decay time constant or the beam lifetime. In general, the cross section for a scattering of a beam of spin $\frac{1}{2}$ particles by a target nucleus of spin 1 particles is given in equation 2.8. For the TRIC experiment the above equation reduces to:

$$\sigma_{tot} = \sigma(1 + A_{y,xz}\ p_y p_{xz}) + \sigma_{loss} \tag{3.4}$$

where, σ_{loss} is the loss cross section, which takes beam losses in the COSY ring into account, $A_{y,xz}$ is the spin correlation coefficient and p_y and p_{xz} are the proton and deuteron polarizations respectively. The figure of merit is derived from the transmission factor by introducing a ratio called the transmission asymmetry, which also eliminates the loss cross section, if the loss cross section (coulomb interaction, for instance) is independent of the polarization of the beam. The transmission asymmetry is defined as:

$$\Delta T_{y,xz} = \frac{T^+ - T^-}{T^+ + T^-} \tag{3.5}$$

Where, T^+ is the transmission factor for the proton spin configuration $p_y > 0$ and deuteron spin alignment $p_{xz} > 0$, T^- is the transmission factor for the time reversed configuration
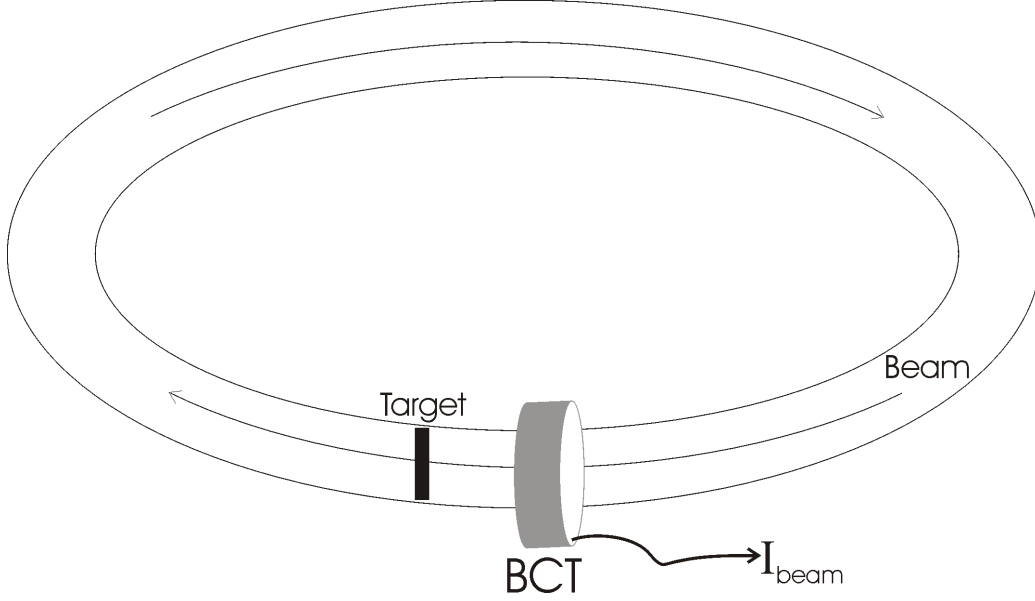
Figure 3.2: The novel technique of measuring total cross section. The beam interacts with the target during each revolution and some particles are lost. The total cross section is calculated from the slope of the current which is measured by the Beam Current Transformer (BCT).

i.e., either $p_y < 0$ or $p_{xz} < 0$. Using equation 3.2, the transmission asymmetry can now be written as,

$$\Delta T_{y,xz} = \frac{\frac{I^+}{I_0^+} - \frac{I^-}{I_0^-}}{\frac{I^+}{I_0^+} + \frac{I^-}{I_0^-}} \tag{3.6}$$

with $I^{\pm}$ being the current after it has passed through the target for t seconds, for the spin configurations described by the superscript and $I_0^{\pm}$ is the initial current for the respective spin configuration. Also, from equations 3.2 and 3.4, the transmission asymmetry can be written as,

$$\Delta T_{y,xz} = \frac{\exp(-\chi^+) - \exp(-\chi^-)}{\exp(-\chi^+) + \exp(-\chi^-)} \tag{3.7}$$

$\chi^{\pm}$ is the product of the factors in the exponent of equation 3.2 with respect to the proton/deuteron spin configuration. From equation 3.7 we get,

$$\Delta T_{y,xz} = -\tanh(SA_{y,xz}) \tag{3.8}$$
$$= SA_{y,xz} \text{ (If the argument of tanh is small)}$$

where $S = -\sigma\rho dn p_y p_{xz}$ is the sensitivity, which is assumed to be a constant. Using equations 3.2 ,3.6 and 3.8, the cross section asymmetry $A_{y,xz}$ can be written in terms of the transmission factor and the sensitivity as,

$$A_{y,xz} = \frac{\Delta T_{y,xz}}{S}$$
$$= \left(\frac{1}{S}\right) \frac{e^{-h/\tau^+} - e^{-h/\tau^-}}{e^{-h/\tau^+} + e^{-h/\tau^-}} \tag{3.9}$$

h is the spin flip period and $\tau^{\pm}$ is the beam lifetime for the respective spin configuration. Using the trigonometric relationship,

$$\frac{e^{-x1} - e^{-x2}}{e^{-x1} + e^{x2}} = -\tanh(\frac{x1 - x2}{2})$$

$$= \frac{(x2 - x1)}{2} \text{ (If the argument of tanh is} << 1)$$

$$A_{y,xz} = \frac{1}{2\sigma\rho \; d\nu p_y p_{xz}}[\frac{1}{\tau^+} - \frac{1}{\tau^-}] \tag{3.10}$$

In the TRIC experiment, the lifetime of the beam is estimated by approximating the exponents in equation 3.9 by a straight line $I_0 - bt$. Then the ratio of the intercept to the slope is the lifetime $\tau = I_0/b$. So,

$$A_{y,xz} = \frac{1}{2\sigma\rho \; d\nu p_y p_{xz}}[\frac{b^+}{I_0^+} - \frac{b^-}{I_0^-}] \tag{3.11}$$

The cross section asymmetry is thus proportional to the difference in the slopes normalised to their respective initial currents $I_0^{\pm}$, as shown in figure 3.3. From Appendix C,
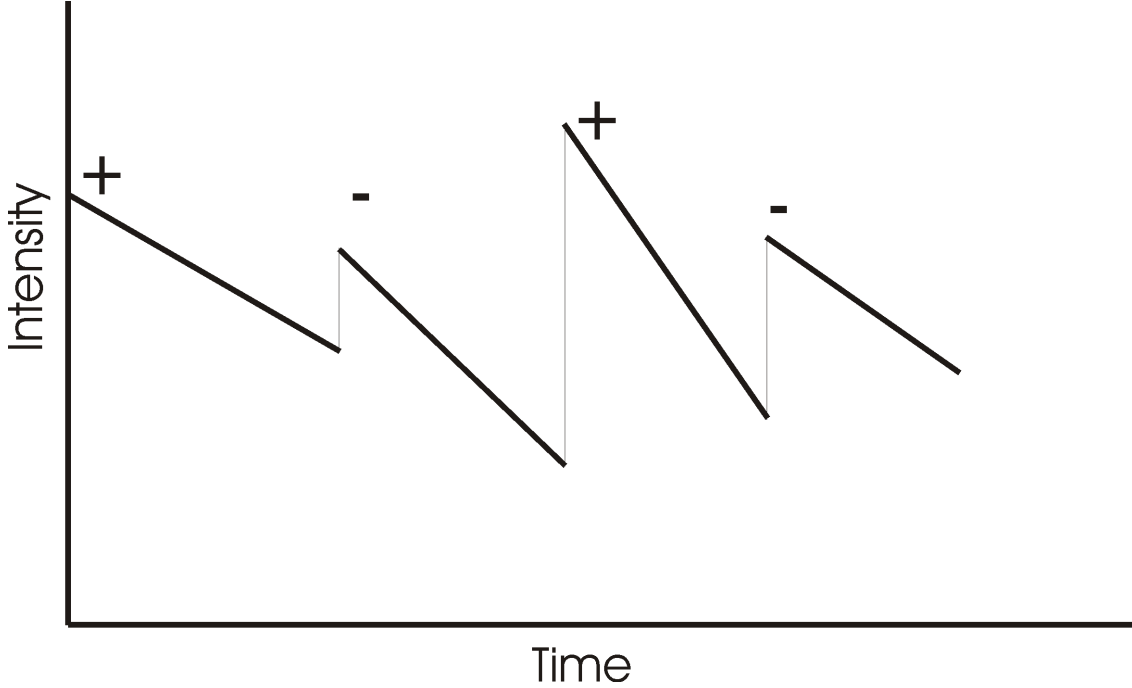
Figure 3.3: The asymmetry $A_{y,xz}$ is proportional to the difference in the slopes between the two polarization states (+/-) of the beam or target.

the accuracy of the figure of merit is :

$$\delta A_{y,xz} = \frac{1}{(\sqrt{2}I_0\sigma\rho d\nu p_y p_{xz})}\sigma_b \tag{3.12}$$

The accuracy in the figure of merit thus depends on the accuracy with which the slope of the beam current can be measured. The above equation written in terms of the total beam time H and the spin flip period (from Appendix C):

$$\delta A_{y,xz} = \frac{4 \cdot 10^{-12}}{(I_0\sigma\rho d\nu p_y p_{xz})} \frac{1}{h\sqrt{H}} \tag{3.13}$$

For a 10 days beam time with $I_0 = 50mA$, $\sigma = 80mb$, $\rho d = 1.2 \cdot 10^{14} atoms/cm^2$, $\nu = 1.5MHz$ and $p_y = p_{xz} = 1$, the following table shows the improvement in the precision in the figure of merit, with the increase in the spin flip period.

Spin flip period (s)	Number of Measurements in 10 days	Accuracy of $A_{y,xz}$ in 10 days
600	1440	$2 \cdot 10^{-6}$
1200	720	$1 \cdot 10^{-6}$
3600	240	$3.3 \cdot 10^{-7}$
5 days	2	$2.6 \cdot 10^{-9}$

Table 3.1: The dependence of the accuracy of the figure of merit on the spin flip period.

3.3.1 The Shot Noise Limit

From equation C.10 in Appendix C, it is evident that the accuracy can be improved either by increasing the total beam time H or by increasing the spin flip period h. On the other hand, an ultimate lower limit for the accuracy is set by the shot noise of scattering processes itself. Since shot noise is a poisson process, the uncertainty associated with the measurement of the number of scattered particles N is $\sqrt{N}$. The number of scattered particles per unit time $\dot{N}$ (i.e, event rate) is given by $L \cdot \sigma_{tot}$, where L is the luminosity given by $\rho dN\nu$, N being the number of injected particles and σ_{tot} the total cross section. The other terms have their usual meanings. The total cross section in terms of the event rate is:

$$\sigma_{tot}^{\pm} = \frac{\dot{N}^{\pm}}{\rho dN_0\nu} \tag{3.14}$$

where $\pm$ indicates the beam or target polarization. The total cross section in terms of the figure of merit is given by (using $p_y p_{xz} = 1$ in equation 3.4):

$$\sigma_{tot}^{\pm} = \sigma(1 \pm A_{y,xz}) \tag{3.15}$$

which implies,

$$A_{y,xz} = \frac{\sigma_{tot}^{+} - \sigma_{tot}^{-}}{\sigma_{tot}^{+} + \sigma_{tot}^{-}} \tag{3.16}$$

which is also equivalent to, from equation 3.15:

$$A_{y,xz} = \frac{\dot{N}^{+} - \dot{N}^{-}}{\dot{N}^{+} + \dot{N}^{-}} \tag{3.17}$$

The error in the event rate, is $\sqrt{\dot{N}h}$ (for a poisson procees), where h is time interval in seconds. The accuracy of the figure of merit calculated from the shot noise contribution in a time interval h is:

$$\delta A_{y,xz} = \frac{1}{\sqrt{2\dot{N}h}} \tag{3.18}$$

For a spin flip time of h seconds and for a total beam time of H seconds, a total of H/2h measurements can be made for each polarization state. Therefore, the accuracy due to

the combination of statistics is:

$$\delta A_{y,xz} = \frac{1}{\sqrt{2\dot{N}h}}\sqrt{\frac{2h}{H}}$$ (3.19)

$$\delta A_{y,xz} = \frac{1}{\sqrt{\dot{N}H}}$$ (3.20)

The ratio of equation 3.13 and 3.20 is the ultimate limit that has to be considered. For, $\sigma = 80 \cdot 10^{-27} cm^2$, $\rho d = 1.2 \cdot 10^{14} atoms/cm^2$ [32][33] and $\nu = 1.5 MHz$, $\dot{N} = 9.6 \cdot 10^6$ particles/s, the simplified version of the ratio is given by the equation:

$$\frac{\delta A_{y,xz}}{\delta A_{y,xz}^{shot}} = \frac{1115}{h}$$ (3.21)

where in the above equation h, the spin flip period is in seconds.

3.4 Beam Time Requirements and Experimental Needs

From the previous section it is clear that to reach an accuracy of 10^{-6} in the figure of merit, a minimum of 10 days beam time is required, which is equally shared between the two polarization states. An optimal spin flip period of 20 minutes was chosen for the spin flip period (cf. Fig 3.4), since the ratio defined in equation 3.21 is approximately 1 for 20 minutes. Apart from these considerations, one needs to take utmost care in the data acquisition system of the experiment. The fundamental part of the data acquisition namely the current measuring device, decides the ultimate limit of the precision with which the figure of merit can be measured. A dead-time less real-time data acquisition is mandatory for the acquisition of these signals so as to maintain the precision of the current measuring device in the secondary level. For the TRIC experiment, the current measuring device is a Beam Current Transformer (BCT) which has a resolution of $0.5\mu A$ for 1s integration period. The EDDA data acquisition system, which was in operation before the TRIC experiment was not designed to be a real time data acquisition system and to cover measuring intervals of over an hour as these resulted in non-physical gaps in the lifetime curve. In view of this problem, a new and reliable real-time data acquisition had to be designed and built exclusively for the TRIC experiment.
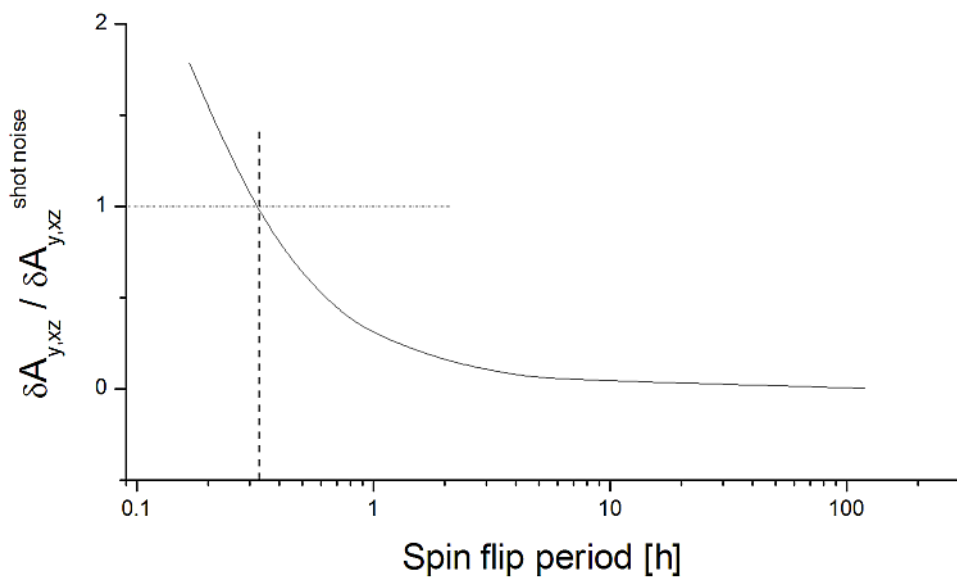
Figure 3.4: The accuracy of the figure of merit normalised to the shot noise limit as a function of the spin flip period.

4 The Experimental Setup

The experimental setup essentially consists of the accelerator (COSY), the Beam Current Transformer (BCT) and the data acquisition system. The vector polarized proton beam in the accelerator is scattered off by the tensor polarized deuteron target and the current remaining in the beam is measured by the BCT. The output of the BCT is a voltage which
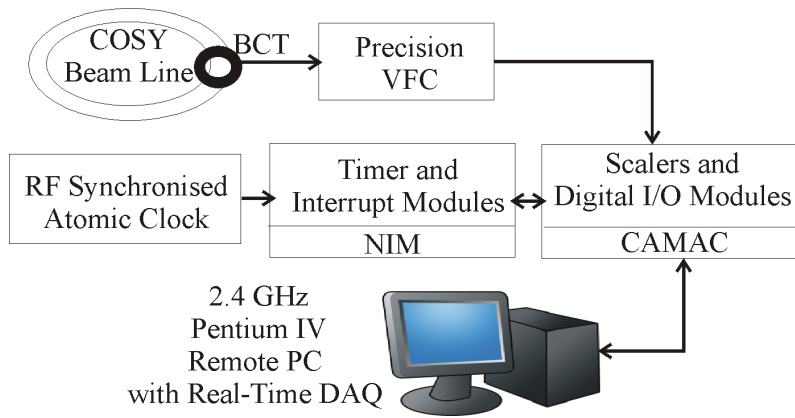
Figure 4.1: The principle of the data acquisition.

is converted into a frequency signal by a voltage to frequency converter (VFC). The VFC is galvanically isolated from the data acquisition via a transformer at its output. The temperature and pressure are measured at suitable places within the ring. The voltage of the holding fields and other parameters are simultaneously measured to check for possible correlations. These signals are fed into scalars that are read in a systematic manner by the data acquisition computer and stored for later analysis. These signals are also displayed in real time by the data acquisition computer. The data flow is shown in Figure 4.1.

4.0.1 The Beam Current Transformer

Since the TRIC experiment is an internal target experiment, the measurement of the current is rendered to a non-destructive current measuring device namely, the BCT. The BCT is a transformer that consists of a coil wound around a ferrite core crossed by the particle beam to be measured (cf. Figure 4.2)[34]. The particle beam constitutes the primary winding of the transformer. A signal is generated in the secondary winding by a time varying magnetic flux due to the beam current. For a coasting DC beam I_{beam}, the BCT is operated as a zero flux transducer. In this case, an additional coil is periodically (≈ 7 KHz) excited and runs the ferrite coil through its typical hysteresis curve. Special electronics compensates any non symmetric hysteresis with a compensation current I_{comp}. The output signal is proportional to I_{comp}, which in turn is proportional to the beam current I_{beam} (cf. Figure 4.2).

17

The resolution of the BCT in the very high resolution mode is $0.5\mu A$ in 1s integration period. A calibration current loop passes through the BCT which can be used for analysis of the BCT using external calibrated current sources.
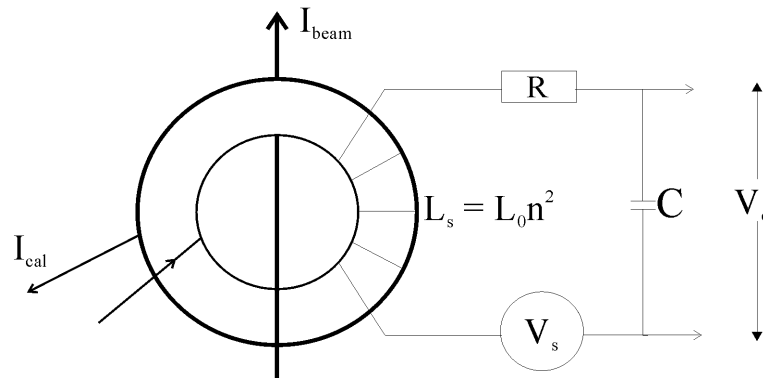
Figure 4.2: The principle of the Beam Current Transformer.

4.0.2 The Voltage to Frequency Converter

The next stage is the VFC which converts the voltage signals from the BCT into pulse trains. The VFC has to equally carry on the precision offered by the BCT. For this purpose a Teledyne Philbrick 5 MHz Hybrid Voltage to Frequency Converter (4743) chip was used. The VFC was tested for its linearity and a drift was seen which was attributed to the temperature dependence of the VFC[35]. This was corrected by a special temperature compensating circuit. The results are shown in Figure 4.3. The VFC with its temperature stabilization circuit offers precision in the required order of 10^{-6}.
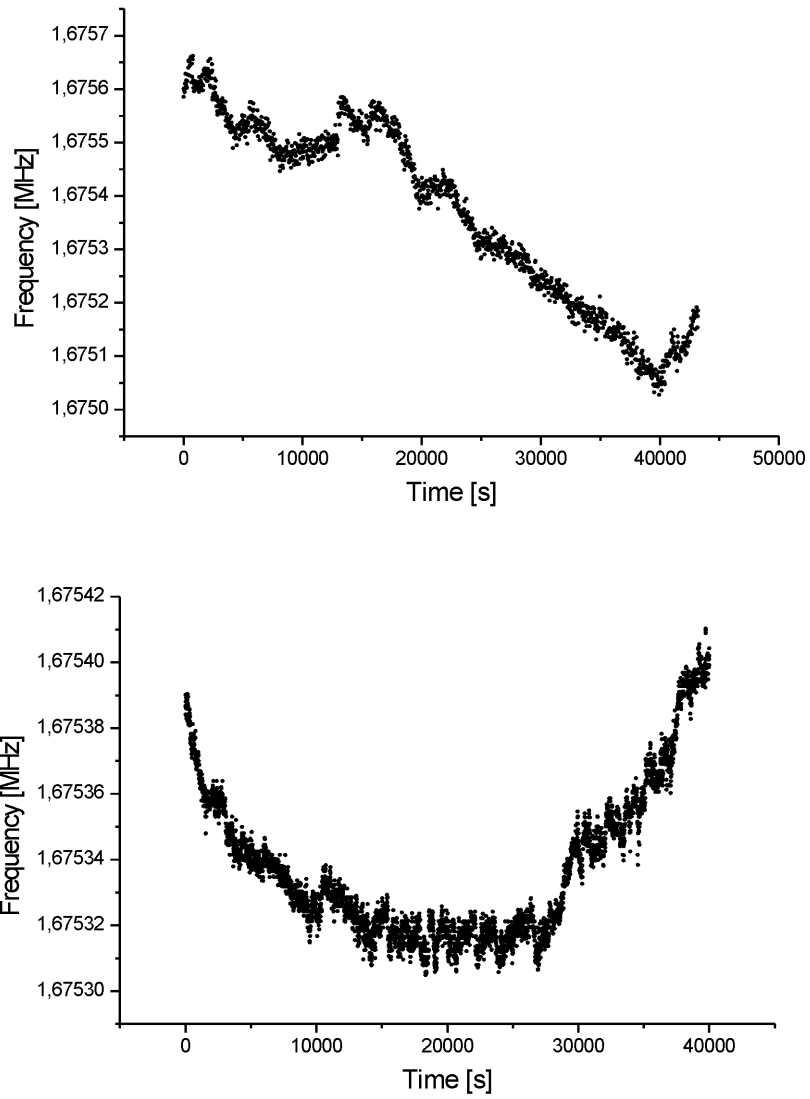
Figure 4.3: Above: VFC output without temperature stabilization. Below: VFC output with temperature stabilization. Note: The y scale is different for the two plots.

4.1 The Real-Time Data Acquisition System

The Data acquisition (DAQ) for the TRIC experiment needs to be a fast and reliable system. The precision that the experiment seeks to achieve demands a data acquisition with negligible dead time. Moreover, the interrupts from the DAQ should be alloted the first priority and should be handled in a deterministic manner. In a deterministic system the maximum response time to an interrupt is fixed. More than the throughput, it is this timing which plays a key role.

The management of different tasks in a multitasking operating system by time slicing, Processor level and Programmable Interrupt Controller (PIC) level interrupt masking or bus conflict due to peripheral devices make a system non-deterministic. A real-time operating system is a deterministic system. Real-time operating systems are classified as hard real time systems and soft real time systems. In a hard real time system, a maximal response time should be met under any circumstances. In a soft real-time system, slight deviations are tolerable. As a consequence, in a high precision measurement environment a soft real-time system is not suitable and one needs a hard real-time system.

Windows XP was chosen as the operating system due to its easy compatibility with third party real time subsystems and graphing and statistical analysis applications (i.e., ORIGIN 7 PRO) and also due to its rich Application Programming Interface (API) and Graphical User Interface (GUI). A GUI provides an easier way to control the DAQ. Though a data acquisition under Windows XP is generally viewed with skepticism, there are enough reasons to believe that ever since the advent of Windows NT 4, Windows as a pure 32 bit system compares well with any other single-processor operating system (cf. Fig 4.4).

Windows XP as such is not a hard real time operating system. To meet stringent latency requirements, the capabilities of Windows XP have to be augmented with a real-time subsystem. It can be modified at the Hardware Abstraction Layer (HAL) level to make it a hard real time operating system. Venturcom's RTX, for instance, provides a real time subsystem (RTSS) for Windows XP by implementing an extended HAL. This extended HAL isolates the interrupts of Windows XP from those of RTSS so that no Windows XP device can interrupt the RTSS. Windows XP processes run as subprocesses under RTSS with respect to interrupts. The RTSS is implemented along with a set of libraries which provide access to real time objects. Win32 processes communicate with the RTSS processes via the Inter Process Communication (IPC) mechanism and a shared memory space.

4.1.1 The Basic Hardware Components

The data acquisition is based on CAMAC with the WIENER CC32 CAMAC crate controller. The CAMAC controller reads/writes to the modules via a fast back plane. The interface to the personal computer (PC) is provided by a PCI card. CAMAC access is performed by mapping the contents of the CAMAC channels to a virtual memory. A CAMAC access (Read or Write) takes via a PC about $1\mu s$.

The data acquisition, during its time of construction underwent major changes in terms of hardware choices. Initially, the PCI CAMAC card was used only for the readout and writing of the modules. A separate PCI card was used for the interrupt handling of the data acquisition. The Keithley KPCI-PIO24 and the Meilhaus 8100A were tested and used as a PCI card for interrupt handling. Though the cards worked perfectly, their performance did not satisfy our experimental needs. One of the reasons were the interrupt response times of these cards which were around $35\mu s$. Later on, the LAM line on the CAMAC PCI card was chosen to handle the interrupts, which outperformed the cards

previously used in terms of its interrupt response time. The interrupt response time was reduced to around $7\mu s$ with this use of the LAM line.
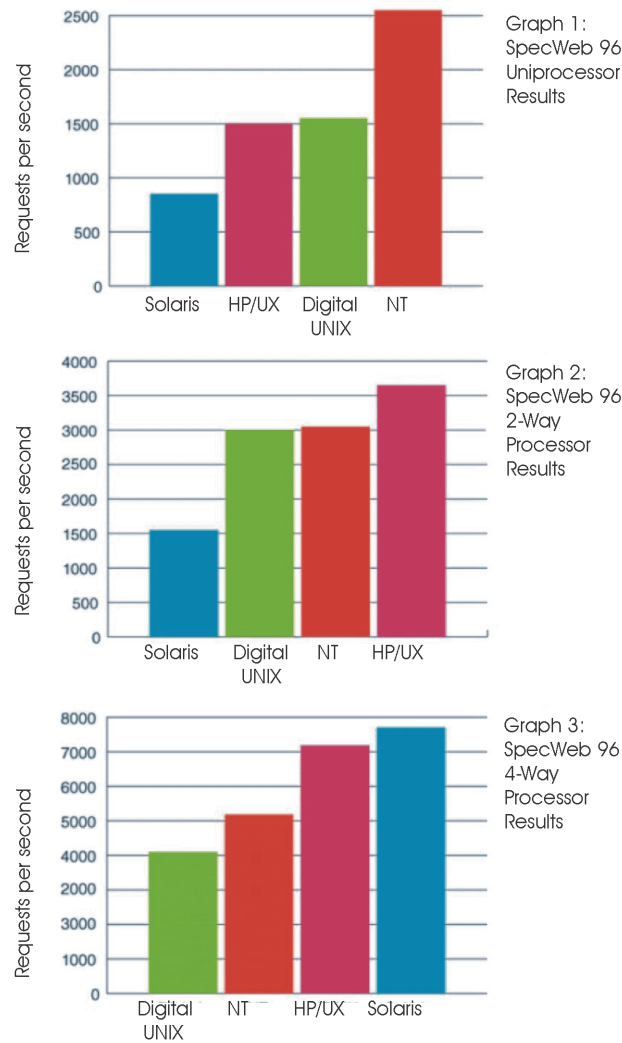
Figure 4.4: Performance of various operating systems [36].

4.2 Deterministic Characters of the Real-Time Kernel and the Test of Reliability.

After the real-time kernel is installed, all real-time processes and interrupts are given the highest priority. This accounts to the deterministic behavior of our real-time system. In order to get a quantitative idea of the performance we could expect from our system with the hardware purchased, a testing procedure was designed and setup. The test measured the time taken from generation of interrupt to the first response of the PCI CAMAC card. Figure 4.5 shows the setup of the hardware used for the test runs.

A control logic was built to monitor and produce the desired signals for the interrupts. The PCI card responded to the interrupts as well as acquired the values of the scaler from the CAMAC crate. On generation of the interrupt(a) triggering the LAM line of an

a-Interrupt (high pulse)
b-Control Signal to Inhibit Scaler (Active High)
c-Scaler Inhibit (Active low)
d-Control Signal to Clear Scaler (Active low),Generate Interrupt & Scaler Enable
e-Clear Scaler (low pulse)
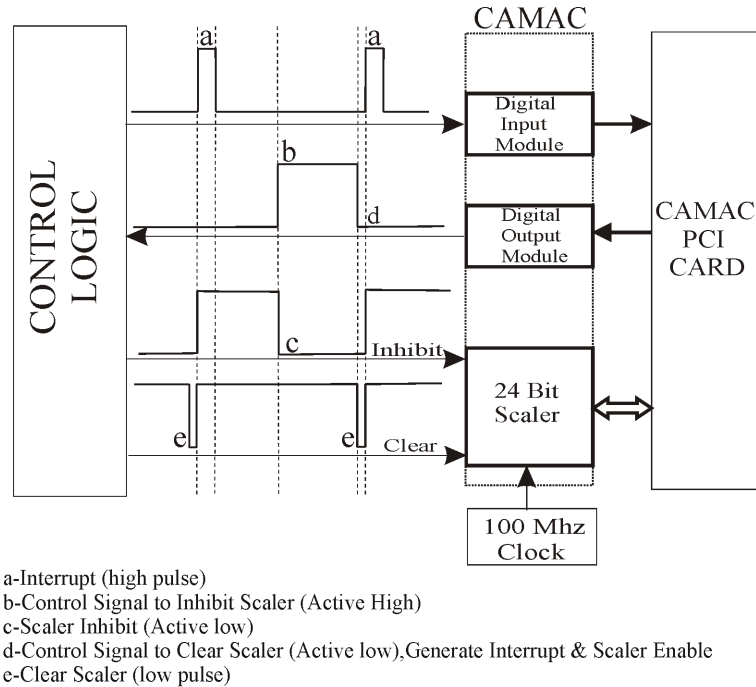
Figure 4.5: Setup for the test of reliability

input module in the crate, which in turn generates a interrupt on the interrupt line in the PCI CAMAC card, the scaler on the CAMAC crate is enabled and starts counting. This scaler is clocked with a 500kHz/10MHz pulse generator. Once the PCI card has processed and acknowledged the interrupt a digital output bit is set high(b). This signal via the Control Logic inhibits the scaler(c). The PC then reads the scaler sorts the data and resets the output (d). This in turn clears the scaler via the control logic and produces a new interrupt(a). With this setup the exact time taken from generation of interrupt(a) to the receipt and service of interrupt(b) is measured. This system is self contained and one single interrupt missed would cause the system to halt.

The hardware and the software from the PC side work as follows. On receipt of an interrupt via the LAM line in the CAMAC PCI card, the Interrupt line A on the PCI bus is set low and therefore is no longer sensitive to any other hardware interrupts. The North Bridge on the Motherboard informs the CPU that an interrupt has been generated. The CPU then stops its current task, saving its active registers and information onto a stack. Since the LAM line is used for the interrupt generation, the Interrupt Service Routine (ISR) is no longer needed to identify the source of the interrupt. The Interrupt Service Thread (IST) does all the time critical jobs like reading the scalar values. Once the IST is completed, the Interrupt line A on the PCI bus is released, ensuring that any further hardware interrupts generated will be seen by the PC. The IST should be kept as short as possible to ensure that the interrupt line A is available as quickly as possible so that no further interrupts will be missed. In case a interrupt was pending while the IST was active, the interrupt buffer module would have noticed it. All time non-critical jobs are handled by a different thread which is triggered inside the IST.

4.2.1 Results of the Test of Determinism

The test of determinism was carried out under different conditions. Tests were conducted with Windows only and Windows with the real-time kernel installed. In both the cases, the test was conducted with and without heavy work load. The non-deterministic behavior of Windows was clearly seen in all cases and especially even in the case with no heavy work load. An audio file with random graphic sequences was used to simulate a heavy work load. The result for the case with heavy work load is presented in figure 4.6. The plot shows the number of interrupt serviced in a specific period. The response for Windows only is shown in black. The thin red needle near the origin is the response for Windows with the real-time kernel installed. The plot shows that the time taken for the interrupts to be serviced is non-deterministic due to the presence of outliers even in the range of 6ms and above but in the case of the real-time system, the maximum latency is restricted to about $10\mu s$. The real-time system is thus a deterministic system.
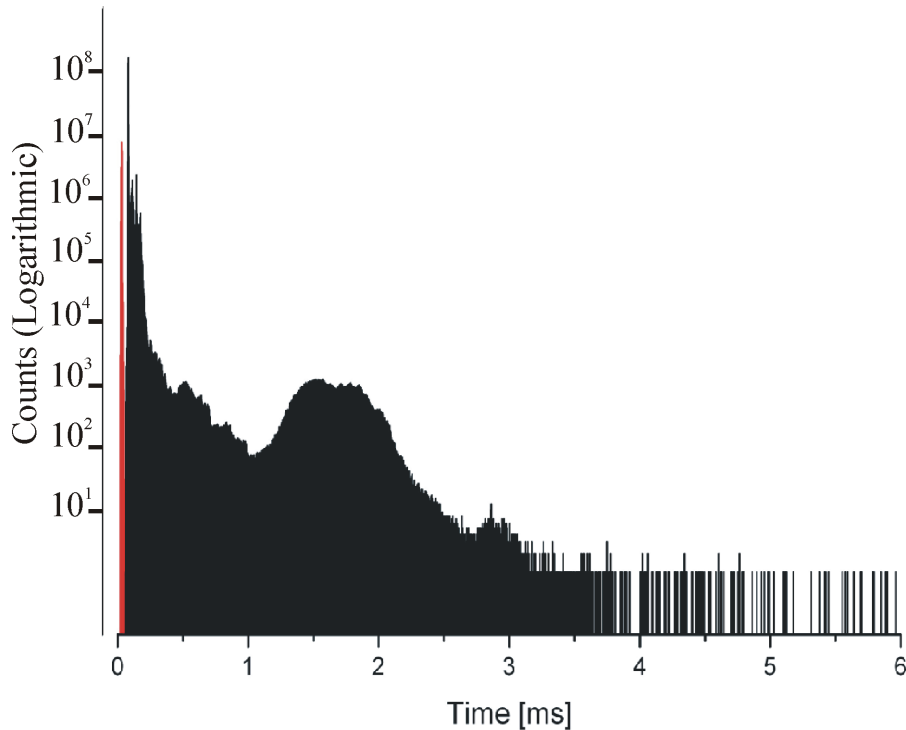
Figure 4.6: The result of the test of determinism. The response for Windows only is shown in black and the response for Windows with RTX installed is seen as a thin needle in red. The determinism of RTX is clearly seen.

4.3 The Structure of the Data Acquisition

4.3.1 The TRIC Timer Module

In a real time environment, it is important that the hardware works in tandem with the software. The indigenously built timer and timer-control form the first stage of the data acquisition. The purpose of the timer is to alternatively control two sets of scalers (L and R) so that when one scaler set (L, for example) is active the other (R) is inhibited and after a preset time interval, an interrupt is generated and the action is toggled. This

allows one scaler to be processed by the PC, while the other scaler accumulates the data. At any point of time, the active scaler reads in data and the data from the inhibited scaler is read out by the computer via the CAMAC PCI card. This is the principle of the hardware double buffer mechanism which reduces the dead-time of the data acquisition (toggle switching time) to around 30 ns. In view of typical measurement intervals of 1 s to 10 s, this is a $3 \cdot 10^{-7}$ to $3 \cdot 10^{-8}$ effect, which makes a virtual dead-timeless data acquisition. The minimum toggle interval that can be set with a 100 KHz clock input is 10 ms. The circuit diagram for the timer and the timer control is given in the appendix.

4.3.2 The TRIC Interrupt Buffer Module

The use of the LAM line restricts one to only one source of interrupt. In order to provide a vectored interrupt mechanism a two stage interrupt buffer module was built for storing the not yet handled interrupt and decoding the interrupts and thus enabling the extension to 8 interrupt sources. When an interrupt is generated the IST reads a digital I/O module which in turn reads the interrupt module. The module incorporates an input latch and an output latch buffer for 8 independent inputs. Each input is latched by a dedicated D-Flip Flop on the leading edge of the respective logic pulse. An interrupt signal is decoded into an unique bit format which accordingly directs the IST to proceed further with the interrupt. This module can be imagined to be a hardware pointer to a specific interrupt associated to one of the 8 interrupt inputs. Thus, the usual time consuming polling of the interrupt source in the CAMAC environment is avoided.

Digital I/O modules from Hytec were used to control the settings of the hardware and to set/reset the control bits like start/stop of DAQ, timer settings, external current source switching etc., of the experiment.

4.3.3 The Software Components of the Data Acquisition

The front end of the data acquisition namely the Graphical User Interface (GUI) was written in Visual C++ (VC++) using the Microsoft Foundation Class (MFC) libraries and dynamic linked libraries (dll). The real-time process was written in C. The real time process takes care of the entire data acquisition. The GUI helps the user to control the settings of the experiment. The two applications communicate via a shared memory in the real time kernel and other Inter-Process Communication (IPC) objects like events. The flow of the interrupt and data from the hardware to the PC is shown in figure 4.7.

4.3.4 Interrupt Management

The RTX interrupt management routines provide interfaces that enable an application to satisfy interrupt requests from devices attached to the computer. The priority assigned to the interrupt handler thread determines the priority execution order of the interrupt handler in both the RTSS and Win32 environments. When an interrupt handler is attached to a particular interrupt, a thread is created which responds to the interrupt. This handling thread is analogous to an Interrupt Service Thread (IST). There are twelve interrupt levels available to RTSS. A special interrupt function call maps RTSS priorities into these twelve interrupt levels. The TRIC data acquisition process is always alloted the highest priority.

4.3.5 Shared Interrupts

The facility of sharing Interrupt lines, though supported by the Real Time Kernel, is not implemented in our case. The reason is, when an interrupt line is shared, the interrupt
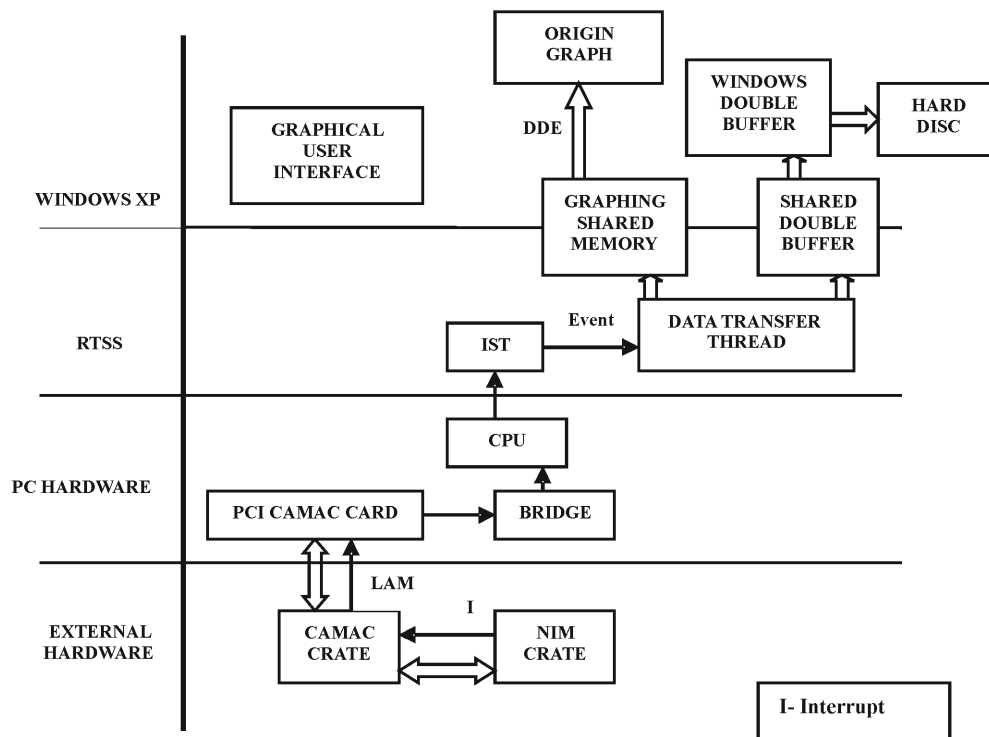
Figure 4.7: The structure of the data acquisition. The timer module and the interrupt buffer module are placed in the NIM crate. The scalers and other digital I/O modules are placed in the CAMAC crate.

handling process becomes complicated and sometimes lengthy. The Interrupt Service Routine (ISR) has to first identify and decode the source of interrupt and then schedule the specific Interrupt Service Thread (IST). This complication has been avoided in this DAQ by using a dedicated interrupt line and thus restricting the Interrupt handler to one IST only. The ISR is no more needed as we know that any interrupt occurring in this dedicated interrupt line must be generated by the CAMAC.

4.3.6 The Interrupt Service Thread

As soon as the INT A line on the PCI card is activated, the process triggers the IST which reads the concerned registers and clears the Look-At-Me (LAM) line. Since the interrupt intervals may be shorter than the service time, there are quite some possibilities of the IST being busy and unable to service the next interrupt. To avoid this, the IST is allowed to do only the time critical jobs like reading the scalers/modules and clearing the LAM etc. Later, a special thread does all the non time critical jobs like transferring the data to the shared memory.

4.3.7 The Graphical User Interface

The GUI was written in Visual C++ (VC++), an object oriented programming language used for interface designing with the use of DLL s provided by the Microsoft foundation classes. The user is given the option of selecting the slots in which the scalers and modules reside in the CAMAC crate and also to choose the identification tags for the data from these

modules. The identification tags are special codes embedded in the data which contain information about the exact source of the data. The default values of the CAMAC slots alloted and settings of the timer and other settings are saved as and when required. The user can also control the TRIC Timer Module and start/stop the data acquisition process. Error messages are displayed to inform the user about the problems that might prevent the data acquisition from proper functioning (e.g., memory overflow, sequence mismatch, CAMAC slot mismatch etc.,). A comment file can also be opened and saved. A separate window manages the windows in the Graphing software. Apart from user interface classes, there are separate threads which run behind the GUI in the Windows environment which manage the data writing to a file, sending data to the graphing software and management of the error display.

4.4 Data Acquisition and Management

Our Data acquisition mechanism ensures a dead time-less operation of the DAQ through the double buffer technique. This is similar in principle to the hardware double scalers (L and R) introduced earlier. The TRIC timer module controls the INHIBIT input of two scalers. Since the outputs are compliments of each other, one of the scalers is inhibited while the other is activated. This sequence is toggled between the two scalers with the toggle frequency pre-chosen by the user. A toggle is also generated whenever the states change, which via the LAM line of one of the modules triggers an Interrupt. The IST routed by the Interrupt, checks for the type of interrupt by reading the contents of the TRIC interrupt module register and other concerned registers. If the Interrupt happens to be from the TRIC timer module, the IST reads the inhibited scaler at that moment, while the activated scaler reads in data. The inhibited scaler is recognized by the bit pattern in one of the input modules. An Interrupt can also occur in case of an scaler overflow, which is dealt accordingly in the IST. This is the principle of our dead-time less (≤ 30 ns while toggling between scalers) data acquisition. The data acquired as such needs to be encoded with identification/timer tags to make the data identifiable under all circumstances. Only these encoded data are written to the disc. The encoding procedure enables one to identify the exact origin of the data. The encoding pattern can be found in Appendix E.

4.4.1 Data Transfer Mechanism

In order to decouple the real time data acquisition from the non-deterministic Windows world, the real time process was used only to acquire the data, while the data storage was executed by Windows. The data transfer between the RTSS and the Win32 process takes place via another shared memory space. A read/write conflict between Win32 process and the RTSS process might lead to unpredictable results. This is prevented by introducing a software double buffer mechanism. Two buffers of equal size are created by the RTSS process at initialization and data are written to one of the buffers. As soon as the Win32 process is ready to read out this buffer, the RTSS process starts writing to the next buffer and the process is repeated. The data is then stored to the hard disc by another thread in Windows. The double buffer mechanism needs right positioning of the memory pointer in the RTSS and Win32 process. The pointers to the double buffer are controlled by an one dimensional array with two elements which can take values 0 or 1. To avoid long waiting states when the disc is busy, a further software double buffer is introduced in the Win32 process, through which the data are transferred to the hard disc. The double buffer mechanism ensures that two different memory operations are executed without hindrance

to each other.
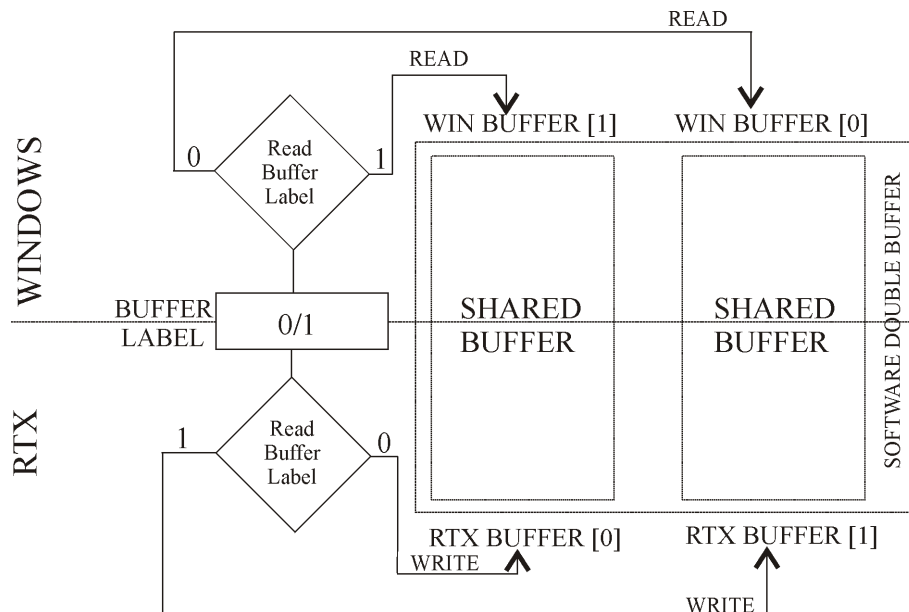
Figure 4.8: Pointer Management in Windows and RTX

4.4.2 Real-Time Graphing of Data and Remote Access

For quick and easy monitoring of the data, a real-time graphing mechanism was needed for the TRIC experiment. Origin PRO 7, a graphing and statistical analysis program was used for the real-time graphing. The real-time process writes data to a pre-alloted shared memory space and Windows sends these data for graphing via the Dynamic Data Exchange (DDE) protocol. DDE is a form of interprocess communication that uses shared memory to exchange data between applications. Applications can use DDE for one time data transfers or for ongoing exchanges and updating data. The Dynamic Data Exchange Management Library (DDEML) provides an interface that simplifies the task of adding DDE capability to an application. Instead of sending, posting, and processing DDE messages directly, an application uses the functions provided by the DDEML to manage DDE conversations. This protocol is much preferred to the Component Object Model (COM), due to the limitations set by the graphing software. Both mechanisms were tested and the performance with DDE was faster and more reliable. The CPU usage was limited to about 16% with 16 layers being updated every 250 ms using DDE while the COM method resulted in 100% CPU usage. A separate window manages the plots in the graph window. Since Origin 7 PRO has in-built DDE server support, all applications have to connect to it as clients.

A remote access to the data and the control of the data acquisition and the TRIC experiment was made available by initiating a secure shell connection between the data acquisition computer and the client computer. The remote desktop connection, an application that is available in all Windows-XP systems comes in handy to directly control the data acquisition computer. However, due to internet security restrictions at the Forschungszentrum Juelich, the remote access is restricted to client computers which have an unique IP address known only to the user and the network administrator.

The data acquisition was tested for its stability under extreme conditions like extra

27

CPU load and fast toggle periods etc. The results were convincing and therefore the DAQ was used for the beam time in September 2004. The data acquisition has been running since then without any malfunction. No unconditional stops were witnessed during its operation. The data acquisition is upgraded frequently to meet the experimentalists need for various measurements.

5 Data Analysis

In the period from 2003 till date, the TRIC experiment was alloted a beam time once in September 2004 and another in October 2006. The run in 2004 lasted for 2 weeks, a major part of which was devoted for machine development. It was in this beam time schedule that the new data acquisition was set into operation. This run was a true test of the feasibility of the TRIC experiment. A vector polarized proton beam was scattered by a vector polarized proton target to measure and compare the spin correlation coefficient $A_{y,y}$ with existing results. The analysis and reduction of the data and the results are presented in this chapter. The main features of the beam time in 2003 is presented in table 5.1.

Total Beam-time alloted	2 weeks
Total Time for $A_{y,y}$ Data	1 day
Beam Momentum	1.6 GeV/c
Target Polarization	90%
Beam Polarization	90%
Target Spin Flip Period (Run section)	20 min
Target Spin Flip Sequence	y,-y,x
Beam Current	≈ 0.5mA
Beam Spin Flip Period (Run)	1 hour
Beam Spin Flip Sequence	y,-y

Table 5.1: Features of the Beam Time in 2004.

During the machine development week, COSY was optimized for the TRIC experiment with respect to beam intensity and cooling. The beam momentum was 1.6 GeV/c. During the actual data taking, the polarized beam was injected, accelerated to the desired momentum and cycled at "flat-top" with this momentum for one hour. At "flat-top" the atomic target was switched on. After one hour of data taking, the target was switched off and the cycling beam in COSY decelerated and dumped finally. During this period, an offset measurement and calibrations with respect to polarizations are made.

For the sake of convenience, the following nomenclature and notation will be used in the rest of this chapter. An one hour run will be called as a run and the 20 minute sections will be called a run section. The polarization setup will be defined using two signs. The first sign represents the polarization of the beam and the second sign represents the polarization of the target. Both the signs represent the polarization in the y direction. For the case of the target polarization in the x direction, the second sign is replaced by x. The notations are explained in table 5.2. The $++$ and $--$ setups are called the parallel configurations and the $+-$, $-+$ setups are called the anti parallel configurations. The $+x$ and $-x$ setups are called the unpolarized configuration since they generate the unpolarized (spin independent) cross section.

Polarization of Beam	Polarization of Target	Notation of Polarization Setup	Configuration
+y	+y	++	Parallel
-y	-y	−−	Parallel
+y	-y	+−	Anti-Parallel
-y	+y	−+	Anti-Parallel
+y	+x	$+x$	Unpolarized
-y	+x	$-x$	Unpolarized

Table 5.2: The notation and the nomenclature used to define the polarization setups.

The beam polarization was flipped between every cycle from y to -y and vice-versa in order to reduce systematic errors. Only the relative beam polarization was available for read out from a bit pattern from the EDDA data acquisition and we assume that we have taken the correct sign of the polarization in our calculations. The target polarization was changed in a specific sequence every 20 minutes. The target polarization sequence started with +y and then flipped to -y and finally to x. The polarization of the target was about 90%. Depending on the beam polarization, the following polarization setups $++, +-, +x$ or $-+, --, -x$ are generated. In the absence of any systematic errors, the lifetime for $++$ ($+-$) should be equal to $--$ ($-+$) and the lifetime for the +x and -x configuration should be the mean of the lifetimes of the parallel and the anti-parallel configurations. Since the temporal positions of parallel and anti-parallel configurations in an 1 hour run are swapped due to the flipping of the beam spin, this constitutes an inherent test for the presence of systematic errors. Thus, with the given polarization setups, there are two conditions that inherently test the presence of systematic errors, one with the comparison within parallel/anti-parallel lifetimes another with the comparison of the mean of the parallel and anti-parallel lifetimes with that of the +x/-x lifetime.

The figure of merit is a quantity that depends on the relative difference of the slope of the beam current between the two parallel and the two anti parallel configurations. Since the accuracy of the slope is inversely proportional to $k^{1.5}$ (refer equation C.1), k being the number of data points, it is advantageous to have runs with measuring periods as long as possible. This is however not possible because the beam decay is no more linear for long measurement periods, which can explain the low lifetimes of the last 20 minute section of each run, where the target polarization is set in the x direction. Therefore, an optimal period of 20 minutes was set for each polarization setup and a run was limited to 1 hour.

Since the slope depends on the initial beam current, a more relevant quantity is the lifetime of the beam. If the exponential decay of the circulating beam is linearized, then the inverse of the lifetime is given by the slope normalized to the initial current. The lifetime is calculated by fitting the data to a straight line (y=I_0+bt), and taking the ratio of the intercept I_0 to the slope b. An equation for $A_{y,y}$ in terms of the beam lifetime can be derived using the approach followed in chapter 3. The spin correlation coefficient is given as:

$$A_{y,y} = \frac{1}{2\sigma\rho \; d\nu p_y p_y^T}[\frac{1}{\tau^+} - \frac{1}{\tau^-}] \tag{5.1}$$

with p_y^T as the target polarization and $\tau^{+/-}$ is the lifetime for the parallel/anti parallel configuration. The other terms have been described earlier. Thus, from the lifetime difference between the parallel configuration and the anti parallel configuration, $A_{y,y}$ can be calculated.

The output of the BCT has a non-zero offset and the first step in the data analysis was to subtract this offset from the data. From these data, the individual lifetimes and their errors were calculated. The individual errors compared well with the value expected from the precision of the BCT as derived from the manual. Since the accuracy of the mean increases with the square root of the number of measurements, the mean of the lifetimes and the standard deviation of the mean was calculated from the distribution of the lifetimes. From statistical considerations, the standard deviation from the distribution of a set of measurements should compare with the standard deviation of a single measurement. A deviation from this prediction is a possible indication of systematic or non-statistical additional noise components in the data. This deviation was seen in the analysis of the lifetime. The standard deviation of the distribution of the lifetimes was a factor 5 to 10 bigger than the error from a single measurement (cf. Figure 5.1).

The intensity of the beam current was found to vary from run to run which has to be taken into consideration in the calculation of the mean and the standard deviation of the lifetimes. It is therefore appropriate to weight the lifetime value by their individual variances. The best estimate of the lifetime is then given by the weighted mean and its weighted error of the lifetimes. Now, the weighted mean and its error became consistent with the expectations from a single lifetime measurement. However, the discrepancy in the standard deviation of the distribution in the unweighted calculations still gave hints on possible additional noise sources. The first observation was that the lifetimes were fluctuating from run to run, far more than the expectations from the standard deviation of a single measurement, which resulted in the widening of the distribution. A FFT of the data revealed substantial 1/f noise components in the data, which caused the slow fluctuations in the data. The slow fluctuations tend to alter the slope which in turn affects the estimate of the lifetime.

The following factors were checked and analyzed with respect to their contributions to the 1/f noise.

- Fluctuations in the clock signal from the atomic clock.

- A current flowing through isolated part of vacuum tube of the ring that passes through the BCT.

- Non-Linearities in the BCT or,

- The Barkhausen noise due to the domain wall motions in the ferrite core of the BCT.

A method to dynamically correct these effects was used, which still did not cure the 1/f noise. Therefore, a new filter based on the Wiener-Khinchin method combined with a global weighted fitting technique was developed to suppress the 1/f noise and simultaneously maintaining the slope. The detailed report of the data analysis is given in the following sections.

5.0.3 Beam Lifetime Analysis

The spin correlation coefficient $A_{y,y}$ is proportional to the difference in the inverse lifetime of the beam for the two opposite polarization settings. The lifetimes and the error in the lifetime were calculated for each run and for the different polarization settings of the beam and target viz.,$(++, --, +-, -+, +x, -x)$.

The analysis showed that the error of the individual lifetime values compared well with the values expected from the precision of the BCT. The statistics were combined to improve the accuracy of the lifetime estimate. Due to this combination, the accuracy

should be improved by a factor $\sqrt{N}$, where N is the number of measurements. But, from the analysis it was seen that the accuracy of the lifetime from the combined statistics (i.e, from the distribution of the lifetimes) was worse by a factor 5 to 10 than that expected from a single lifetime measurement. This behavior is seen in all the polarization setups. The discrepancy for the (++) setup is shown in figure 5.1. In fact, the problem of this type of fluctuations in lifetime has been reported in 2004 by a group[37]. The precision level of the measurements of that group was however substantially less than the TRIC measurements.
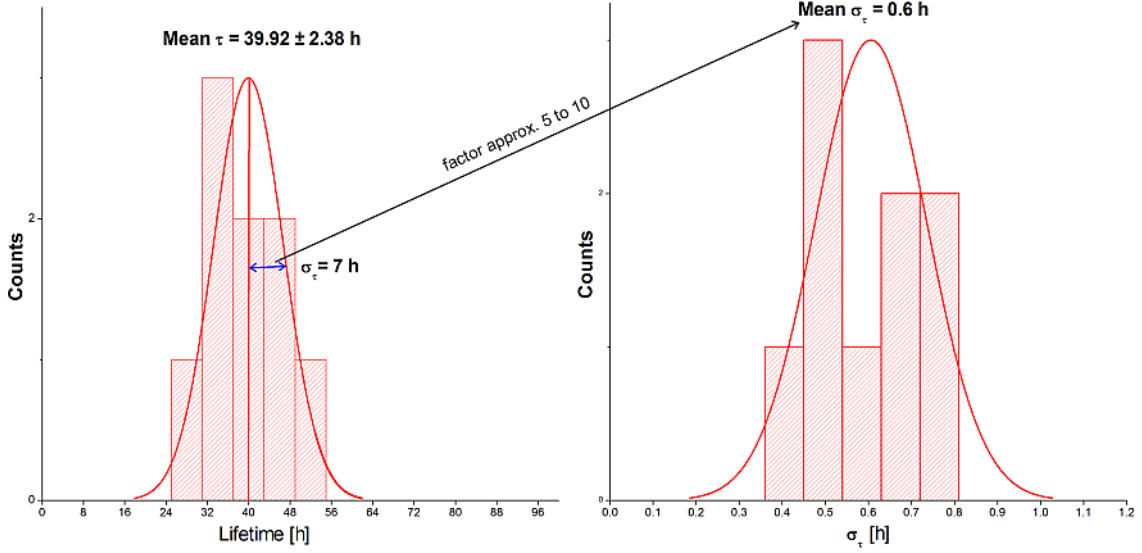
Figure 5.1: The standard deviation of the distribution of the lifetimes is a factor 5 to 10 worse than the error of the single lifetime measurement. The above plot is for the lifetime values for (++) polarization setup. This behavior is seen in the other polarization setups also.

The intensity of the beam current I_0 is related to the error in the lifetime σ_τ as:

$$
\begin{aligned}
\sigma_\tau &= \tau \frac{\sigma_b}{b} \\
&= \tau^2 \frac{\sigma_b}{I_0}
\end{aligned}
\tag{5.2}
$$

where σ_b is the error in the slope. Due to this dependency of the error on the intensity of the beam, the lifetime measured at a higher intensity has a smaller error. From the analysis of the data it was seen that the intensity values varied between runs (by upto a factor 2) which alters the accuracy of the lifetimes. Therefore, the best estimate of the mean lifetime is given by the weighted mean [38]. The weighted mean lifetime is given as:

$$
\tau_{mean} = \frac{\sum(\tau_i/\sigma_{\tau i}^2)}{\sum(1/\sigma_{\tau i}^2)}
\tag{5.3}
$$

where each lifetime value τ_i is weighted by its own variance $\sigma_{\tau i}^2$. The error in the weighted mean is then given by:

$$
\sigma_{\tau_{mean}} = \frac{1}{\sum(1/\sigma_{\tau i}^2)}
\tag{5.4}
$$

The error of the weighted mean of the lifetime compared well with the statistical predictions (i.e, an improvement by a factor $\sqrt{N}$, N being the number of measurements) from a single lifetime measurement. The values of the unweighted lifetimes is shown in figure 5.2 and the values for the corresponding weighted values are given in table 5.3.
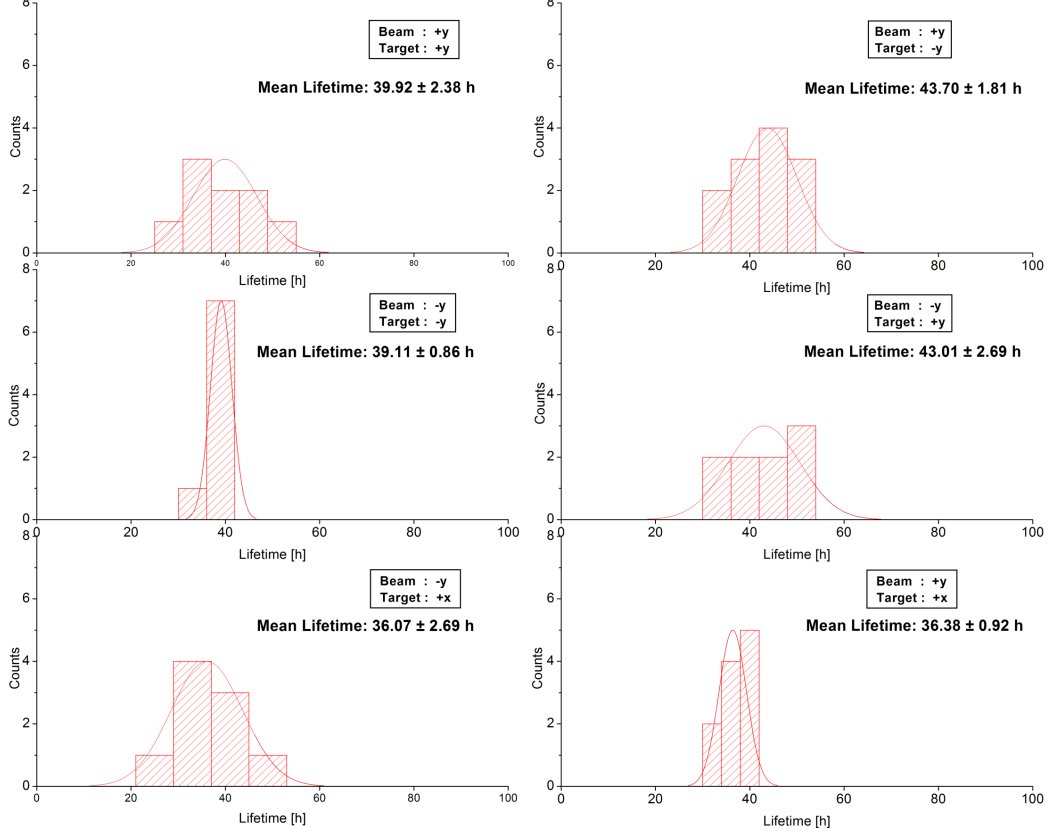
Figure 5.2: The distribution of the unweighted lifetimes of all the polarization setups.

Polarization of Beam/Target	Unweighted Mean of Lifetime [h]	Weighted Mean of Lifetime [h]
-y/+y	39.92 ± 2.38	37.76 ± 0.18
+y/-y	39.11 ± 0.86	38.70 ± 0.21
-y/-y	43.70 ± 1.81	39.94 ± 0.17
+y/+y	43.01 ± 2.69	37.06 ± 0.19
-y/+x	36.07 ± 2.69	35.82 ± 0.14
+y/+x	36.38 ± 0.92	32.92 ± 0.13

Table 5.3: The mean lifetime values for all the polarization setups.

5.0.4 Comparison of Lifetimes of Parallel and Anti-Parallel Polarization Setups

The weighted lifetimes are found to be statistically consistent. However, the inherent test of the reliability of the values by comparing the lifetimes of parallel and anti parallel polarization setups (refer Table 5.3) still displays substantial inconsistencies.

The total cross section σ_{tot} for scattering a spin $\frac{1}{2}$ polarized beam by a spin $\frac{1}{2}$ polarized target is given as [39]:

$$\sigma_{tot} = \sigma + \sigma_{1tot}(\mathbf{P}_B \cdot \mathbf{P}_T) + \sigma_{2tot}(\mathbf{P}_B \cdot \mathbf{k})(\mathbf{P}_T \cdot \mathbf{k}) \qquad (5.5)$$

where, $\mathbf{P}_B$ and $\mathbf{P}_T$ are beam and target polarizations respectively. $\mathbf{k}$ is the unit vector in the direction of the beam. σ is the spin independent total cross section. Both the quantities are positive definite. σ_{1tot} and σ_{2tot} are the spin dependent contributions. For the various polarization setup defined before, the above equation can be written as:

$$\sigma_{tot}(++) = \sigma + \left|\mathbf{P}_B^+\mathbf{P}_T^+\right|\sigma_{1tot}$$
$$\sigma_{tot}(+-) = \sigma - \left|\mathbf{P}_B^+\mathbf{P}_T^-\right|\sigma_{1tot}$$
$$\sigma_{tot}(--) = \sigma + \left|\mathbf{P}_B^-\mathbf{P}_T^-\right|\sigma_{1tot}$$
$$\sigma_{tot}(-+) = \sigma - \left|\mathbf{P}_B^-\mathbf{P}_T^+\right|\sigma_{1tot} \qquad (5.6)$$

and thus,

$$\sigma_{tot}(++) = \sigma_{tot}(--) \text{ and,} \qquad (5.7)$$
$$\sigma_{tot}(+-) = \sigma_{tot}(-+)$$

Comparing equation 5.6 with equation 3.4, σ_{1tot} is related to the figure of merit $A_{y,y}$ as:

$$\sigma_{1tot} = \sigma A_{y,y} \qquad (5.8)$$

From the above equation, if $|\mathbf{P}_B| = |\mathbf{P}_T|$ the lifetimes for the parallel configurations $(++, --)$ should be equal and the lifetimes for the anti-parallel $(+-, -+)$ configurations should be equal. The lifetime for the target polarization along the x direction, should be equal to the unpolarized cross section and thus should be in between the values of the parallel lifetime and the anti parallel lifetime. Thus the lifetime for the target polarization along the x direction provides a measure of consistency of the other lifetimes.

The values of the lifetimes presented in table 5.3, for the unweighted mean suggest that the lifetimes in the respective parallel/anti parallel configurations are almost equal i.e, $(++ \approx --)$ and $(+- \approx -+)$. The significance of the difference between the lifetimes in the same configuration (i.e, parallel/anti parallel) can be tested by a t-test. For a significance level $\alpha = 0.05$, the values from a t-test suggested that the difference is really significant in the case of the weighted mean. The difference in the case of the unweighted lifetimes was not significant. This is a result of the wider distribution in the case of the unweighted lifetimes.

The width of the distribution of the unweighted lifetimes provides information about the variation of the lifetime from run to run. This variation was also seen in parasitic measurements during the COSY 11 and ANKE experiments. The reason for this variation can be attributed to fluctuating slope values. The correlation studies of temperature and pressure in the ring showed that the variations were not related to the fluctuations in these dynamic parameters (cf. Fig 5.3 and 5.4).

Another subject of concern is that the lifetimes (weighted and unweighted) for the target polarization in the x direction are much lower than the lifetimes of the other polarization setups. This is in contrary to the expectations from equation 5.5. It can be explained by the non-linear behavior of the beam in the last 20 minutes of the run. This effect was not seen clearly in a single run but could only be verified in the curvature seen in the sum spectrum where all the available datasets are summed up which is shown in figure 5.5. The curvature increases the slope thus decreasing the lifetime.

Figure 5.3: Correlation of temperature with lifetime.
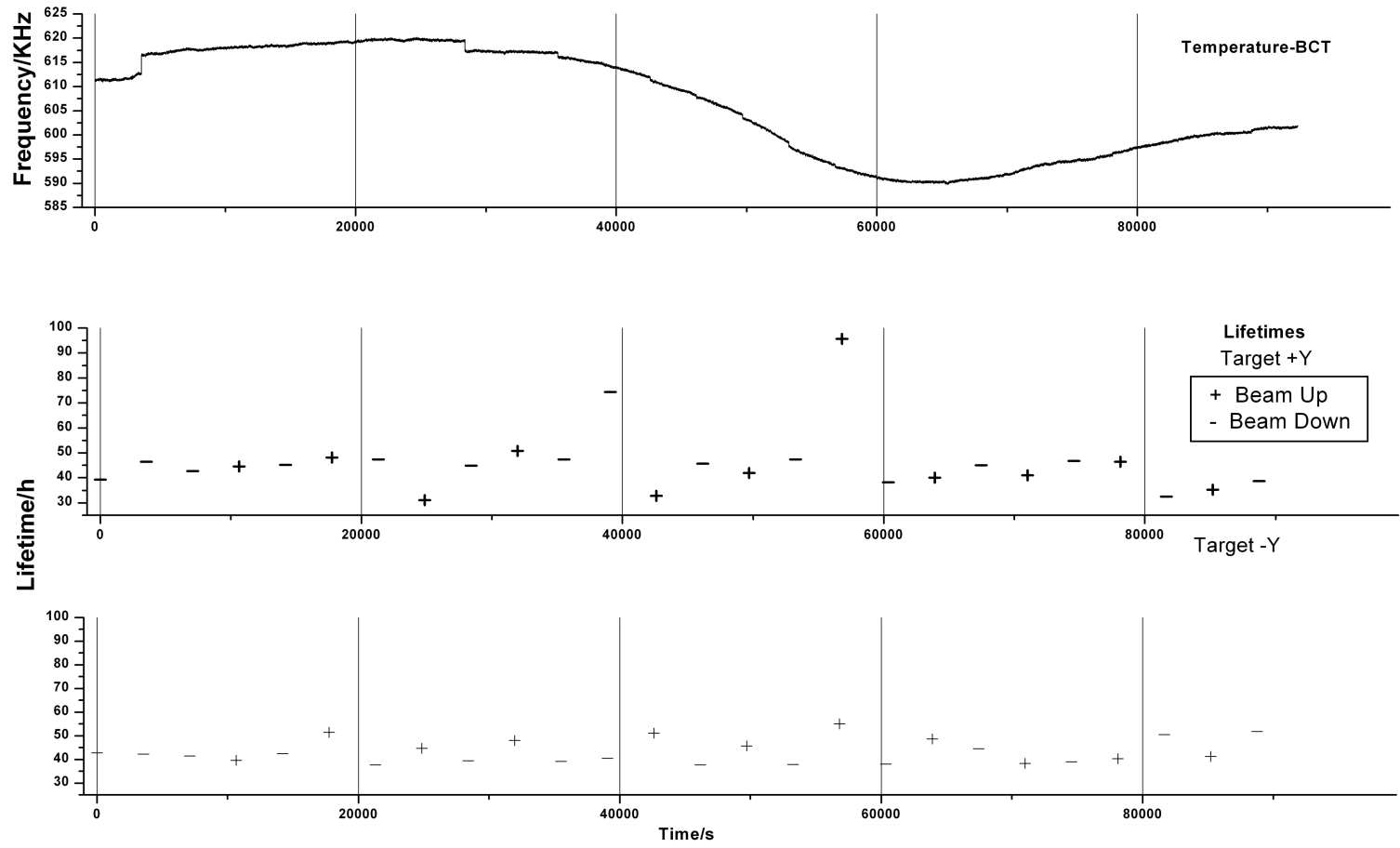
Figure 5.4: Correlation of pressure with lifetime.
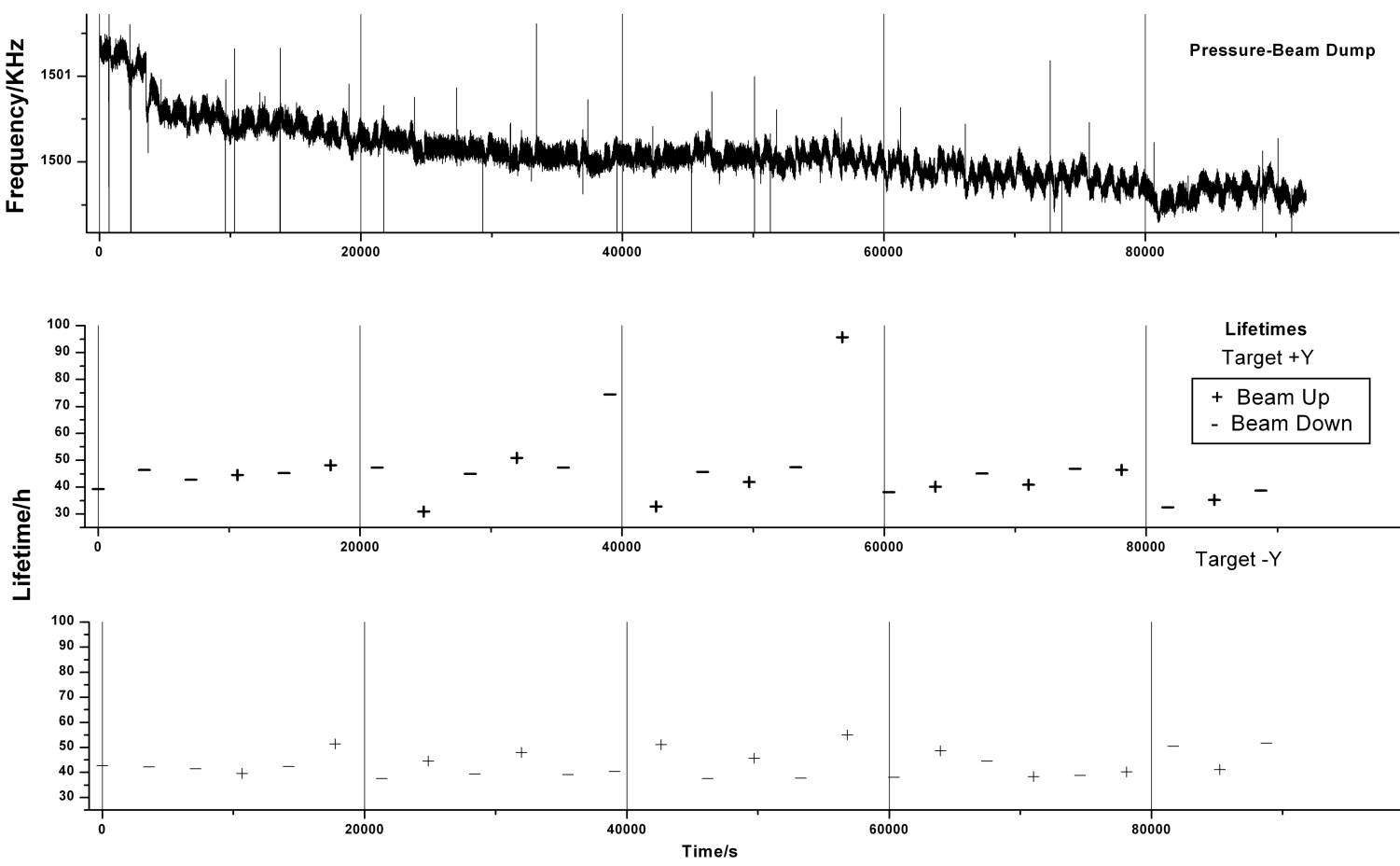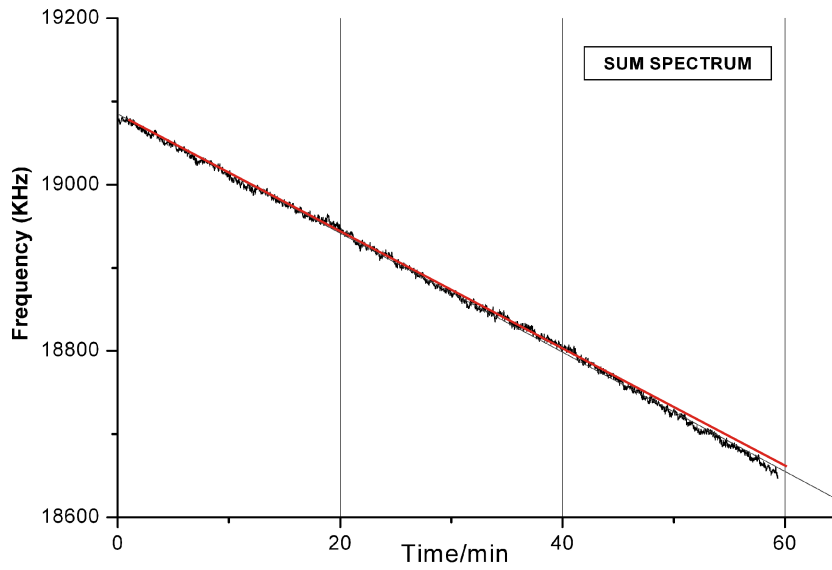
Figure 5.5: The sum spectrum of all the available runs which shows a slight curvature in the final part of the run. The red line is to guide the eye along a straight line that passes through the first 40 minutes.

The reason for this curvature can be attributed to the emittance growth of the beam, which was suggested by previous studies on internal targets [40][41]. The emittance growth function as a function of the turn number is plotted in figure 5.6
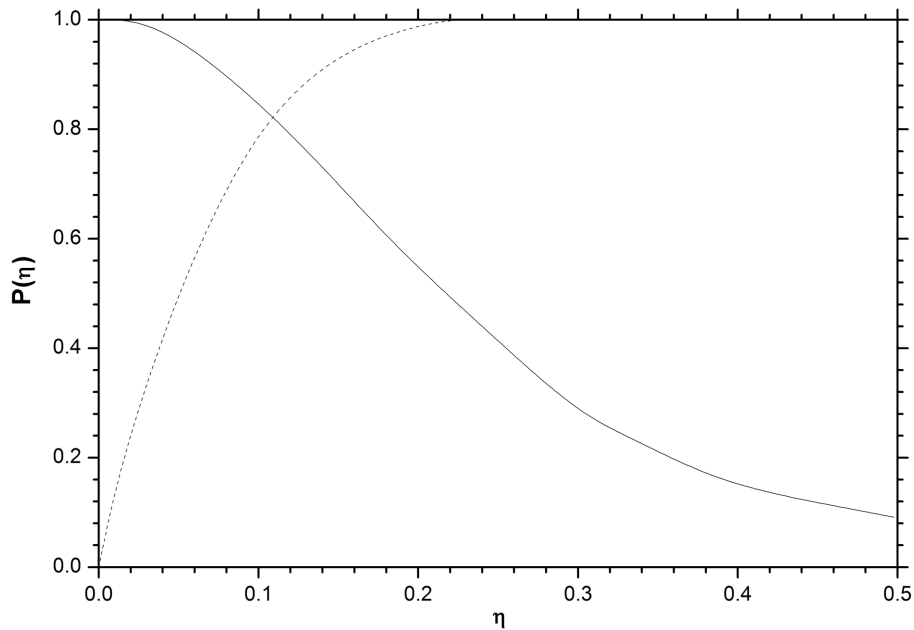
Figure 5.6: The Survival probability (full curve) and the emittance growth function (dashed curve). The dimensionless variable η increases linearly with turn number.

The following sections discuss the analysis made to understand the possible causes of the variation in the lifetime values from run to run.

5.0.5 The Sliding Fit Analysis

In order to understand the lifetime fluctuations, the behavior of the lifetimes within sections of a single run had to be analysed. A sliding fit was used for this analysis. A window of a specific length moves over the data and a linear fit is made on that specific part. The lifetime is calculated for that specific region of the data. The results showed huge fluctuations in the lifetime (cf. Fig 5.7). Lifetime values fluctuated between negative values and values greater than 1000 hours. Ideally, one would expect a constant line for each polarization setup. This was a vital clue to possible fluctuations found in the data which strongly influence the slope estimation. Slow fluctuations were in fact found in the data as shown in figure 5.8.

In order to understand the influence of the beam and target on the slow fluctuations, the FFT of the data with beam and target on was compared with the data taken during the time when the beam and target were switched off. This is the offset of the BCT. The noise content in the offset data was much lower than the noise in the data with beam and target (cf. Fig 5.9).

The results from the sliding fit show that due to the presence of the slow fluctuations in the data, the slope values in each window differ substantially from each other. Also, the presence of substantially high and improbable lifetimes indicate that the slow fluctuations can lead to inaccurate estimates of the lifetime. The FFT of the data shows a small increase toward low frequencies which indicates that these slow fluctuations result from 1/f noise present in the data.

The RF synchronized atomic clock provides the timing signal for the data acquisition
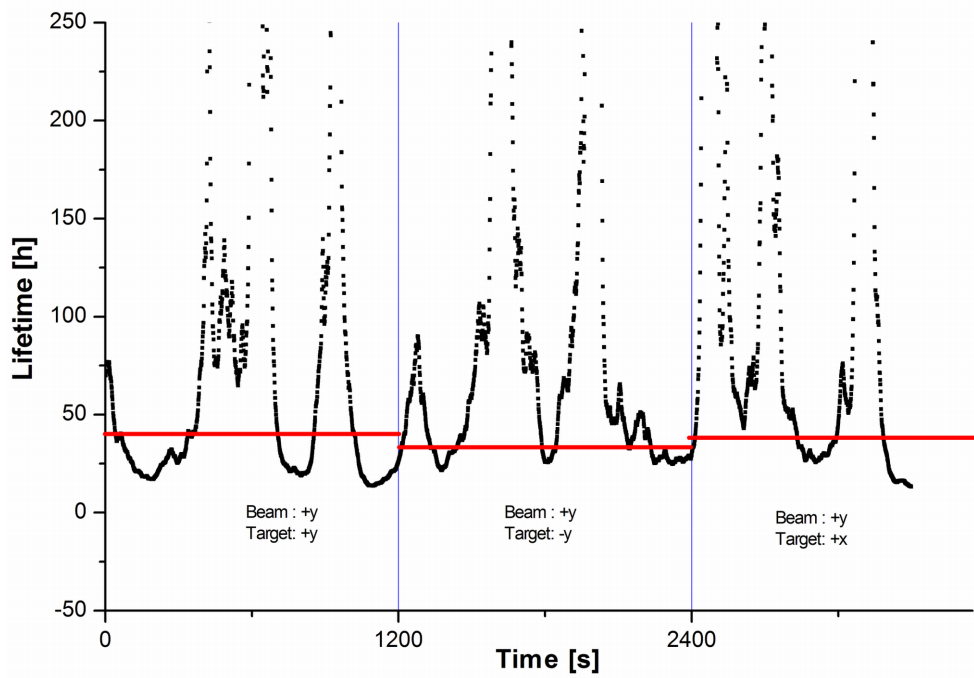
Figure 5.7: Lifetime fluctuations seen from the sliding fit. The red line is an idealization of the expected behavior. A window length of 250s was used for the plot above.
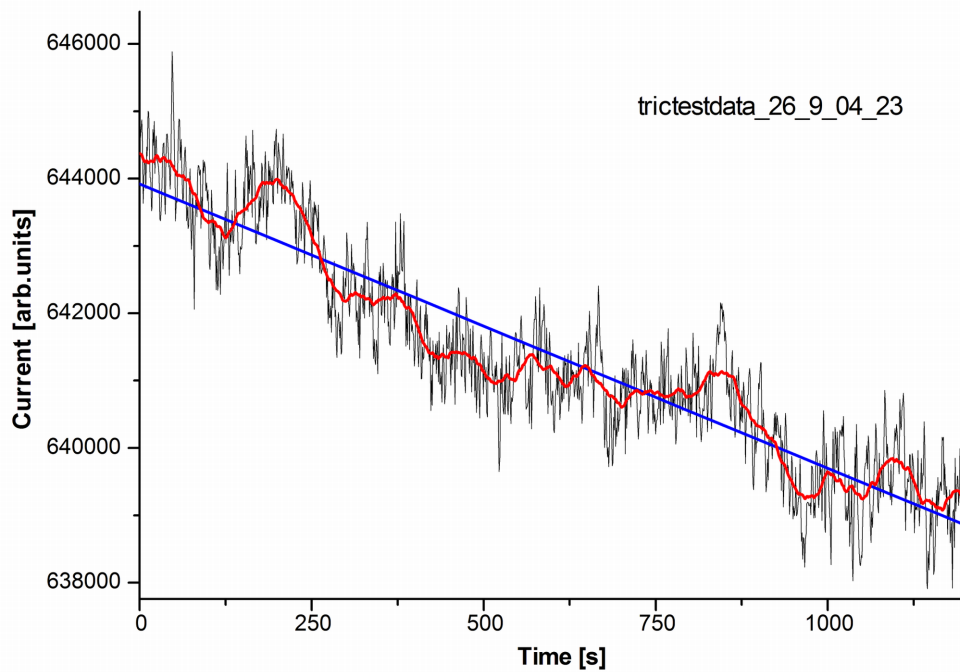
Figure 5.8: The slow fluctuations found in a typical TRIC run. The red line is the smoothed data to guide the eye along the slow fluctuations. The blue line is the linear fit to the data.
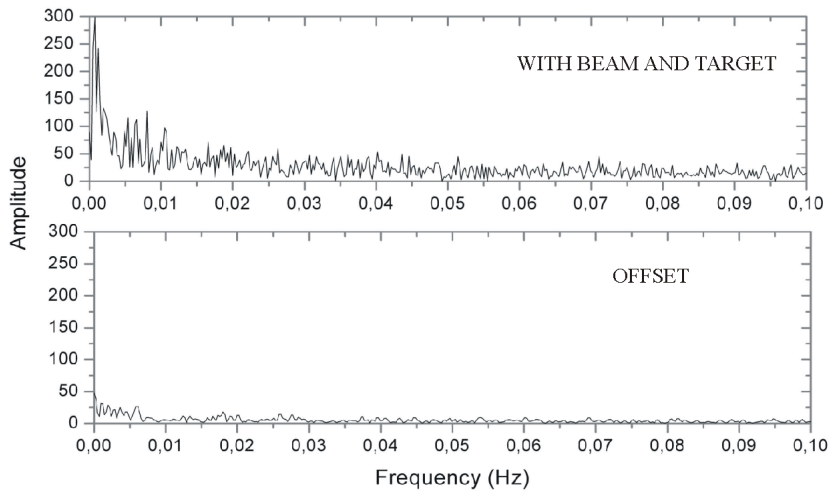
Figure 5.9: The noise spectrum of the data with beam and offset.

(cf. Figure 4.1). An instability of the clock would cause improper synchronization of the read-out of the scalers by the computer which could result in fluctuations in the data. This was however ruled out in systematic studies by replacing the clock by a stable ($\approx 10^{-8}$) oscillator with a preset frequency.

The vacuum tube of COSY runs electrically isolated through the BCT. A voltage drop across the tube would cause a current through the BCT and thus could influence the BCT readings of the cycling COSY beam. To verify this, a differential amplifier was connected across the beam pipe and the output signal was analyzed. The results showed no relevant voltage drops.

5.0.6 Non-Linearities in the BCT

Slow fluctuation can also be caused by non-linearities in the gain of the BCT. To study the non-linearities in the BCT, a modulated current of 1 mA with a precision of $\approx 10^{-6}$ was passed through the BCT via the calibration loop (cf. Figure 4.2). The direction of the current flow was flipped periodically. Once the beam is on, the output signal from the BCT would then read $I \pm \delta I$ depending on the direction of the modulated current (cf. Figure 5.10). I is the beam current and δI is the increment in current. The difference between two neighboring data points is thus proportional to $2\delta I$. A change in gain of the BCT would cause this difference to change proportionately and thus would reveal the non-linearities in the BCT. The circuit diagram of the modulator can be found in Appendix B. The modulator is synchronized with the TRIC timer module to have a systematic readout of the modulated current. The modulator was used in a parasitic measurement during one of the experiments at COSY. The results showed an intensity related change of the BCT gain. The results are plotted in figures 5.10 and 5.11. The effect seen is in the order of 10^{-4} in amplitude. Using all the available data, an universal gain curve was obtained which was used to correct the gain and thus the data. The universal gain curve is shown in figure 5.12 and the corrected gain curve is shown in figure 5.13. However, the correction did not significantly improve the influence of slow fluctuations.
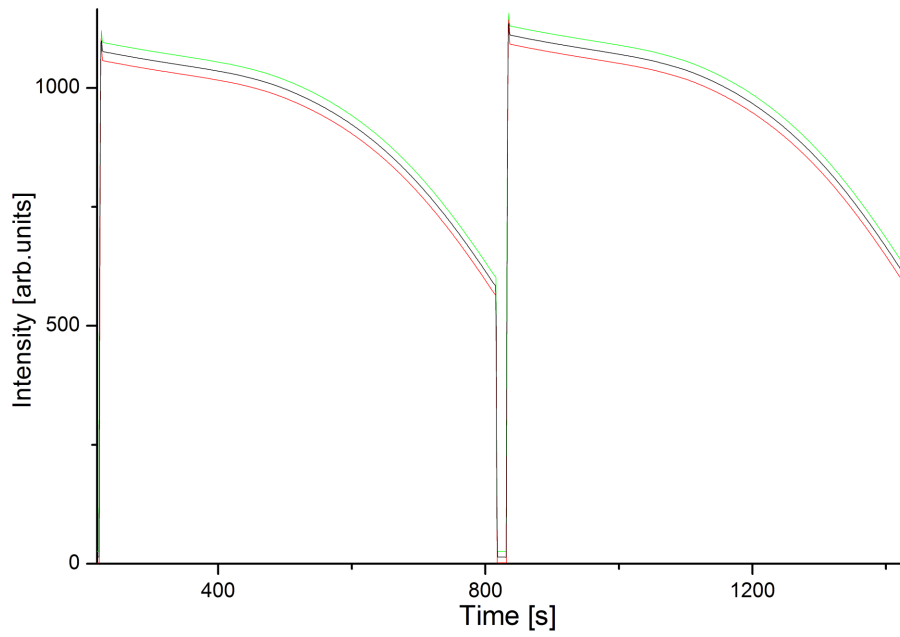
Figure 5.10: The red (lower) and green (upper) lines are due to the addition of a modulated current ($\pm\delta I$) to the beam current. The black (middle) curve is the average of the upper and the lower curves.
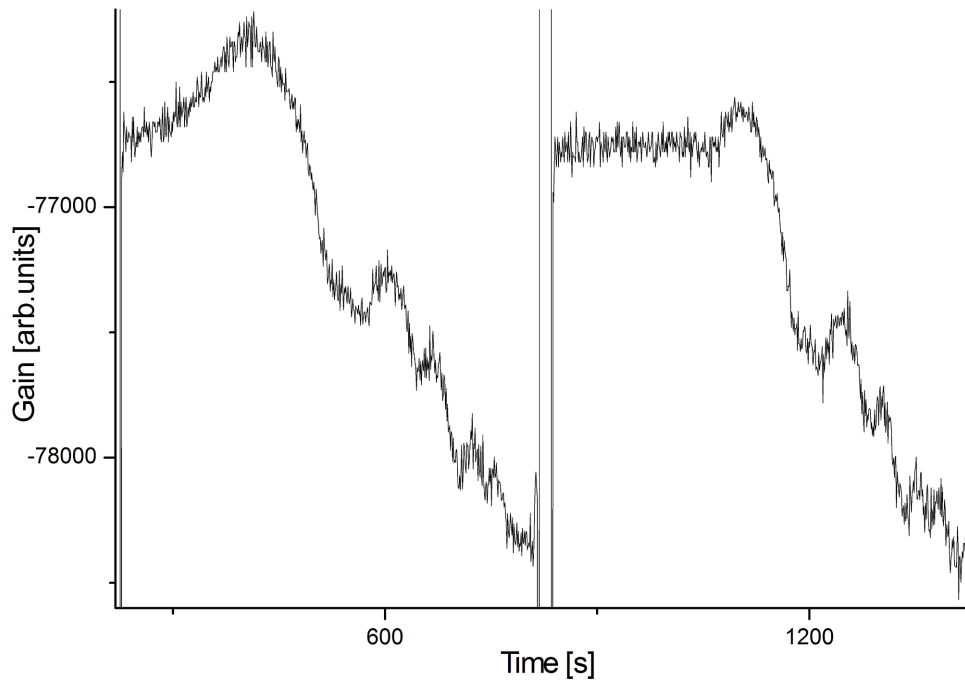
Figure 5.11: The difference between two neighboring data points. Non-linearities are revealed in this plot.
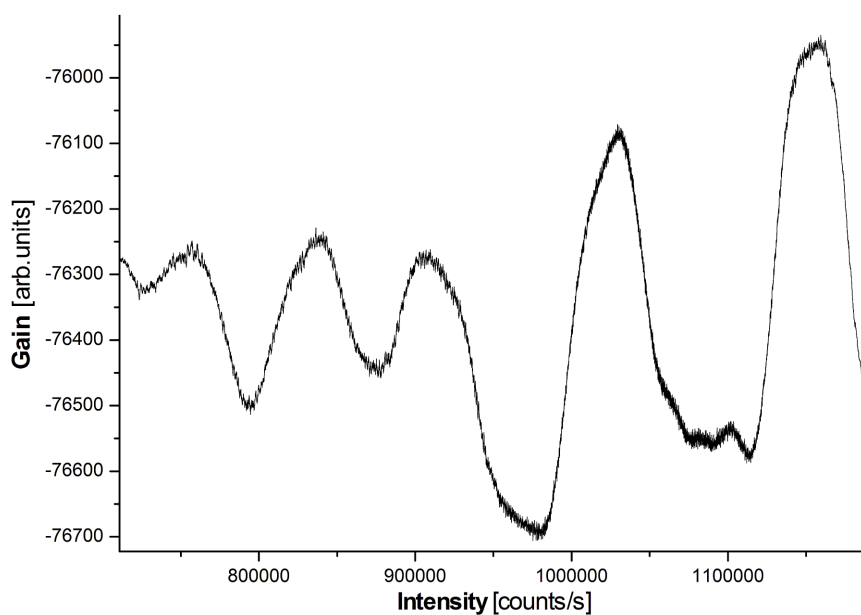
Figure 5.12: The universal gain curve constructed from all available data.
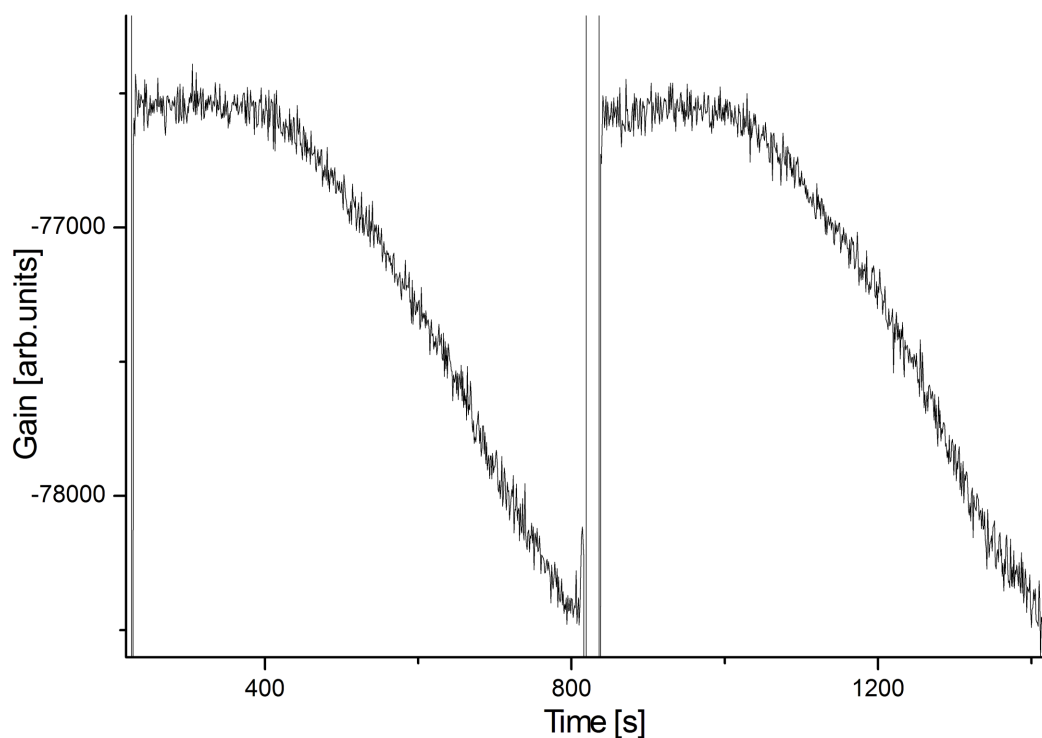
Figure 5.13: The corrected gain curve of figure 5.11 using the universal gain curve.

5.1 Constant Current Analysis

To further understand the BCT noise behavior, a constant current (1 mA) was passed through the calibration loop (cf. Figure 4.2) in the absence of the COSY beam. The
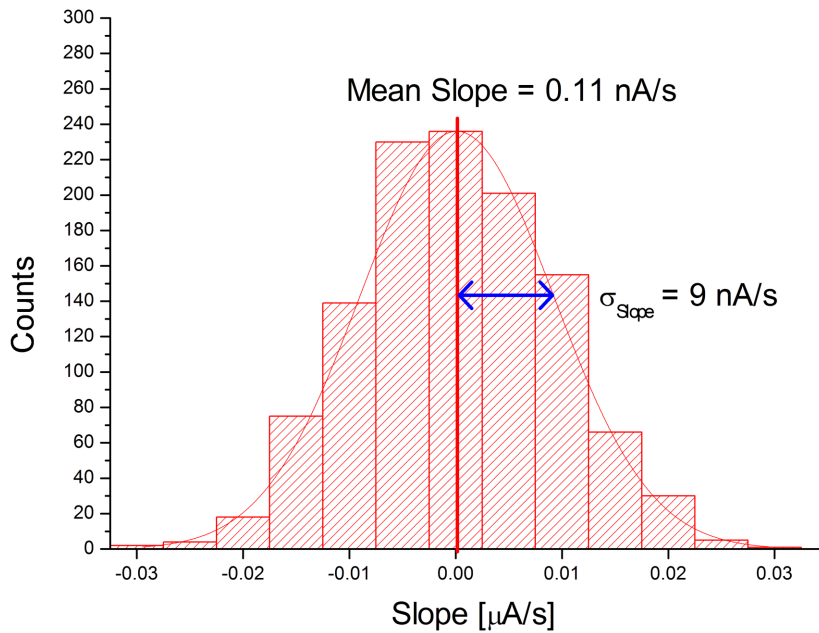
Figure 5.14: The distribution of the slopes of the individual sections.

data was acquired continuously for 16 hours and was analyzed. The data was split into equal intervals and the slope and its error calculated for each of these intervals. From the distribution of the slopes, an estimate of error of the individual slopes can be calculated. The estimated error of the slopes from the distribution is compared with that of the mean of the individual errors. The error from the distribution is a factor 4 greater than the individual errors, an effect which was also seen in the analysis of the lifetimes. The distribution of the slopes and their errors are plotted in figures 5.14 and 5.15.

The fact that the distribution width is greater than the individual errors indicates that the slopes vary from interval to interval. A FFT of the entire data was made to understand the underlying frequency components. The FFT showed that the noise in the data is not white but rather has an 1/f behavior. For comparison, a model straight line to which a suitable random number is added to each data point, so that the noise is comparable to the 1mA data was also analyzed. The FFT of this model data was a flat spectrum, the signature of white noise (cf. Figures 5.16 and 5.17). Thus, 1/f noise in the data is the cause of the unexpected discrepancy found in the analysis of the slopes in the constant current analysis. Therefore, 1/f noise in an inherent problem of the measurement method.

1/f noise in physical systems arises due to a property called as the Self Organized Criticality (SOC) [42]. The Barkhausen effect which is due to the dynamics of ferromagnetic domain wall motion is also an effect of (SOC) [43][44]. The magnetic characteristics of a ferromagnet is determined by its magnetic domain distribution and the response of these domains to applied magnetic fields. The domain wall motion in a ferromagnet in response to a change in the externally applied magnetic fields happens in an irregular manner. As a result of this irregular motion, the magnetization changes in bursts, leading to the phenomenon of Barkhausen noise[45]. The stochastic nature of this motion is due to internal stresses in the material, surface defects or impurities in the material. The spectrum analysis of 1/f noise is seen to have an 1/f dependence[43]. The 1/f noise seen in our data can be due to the domain wall motion in the ferrite core of the BCT.

The only cure to this problem is to use a non-ferrite core in the magnetic sensor of
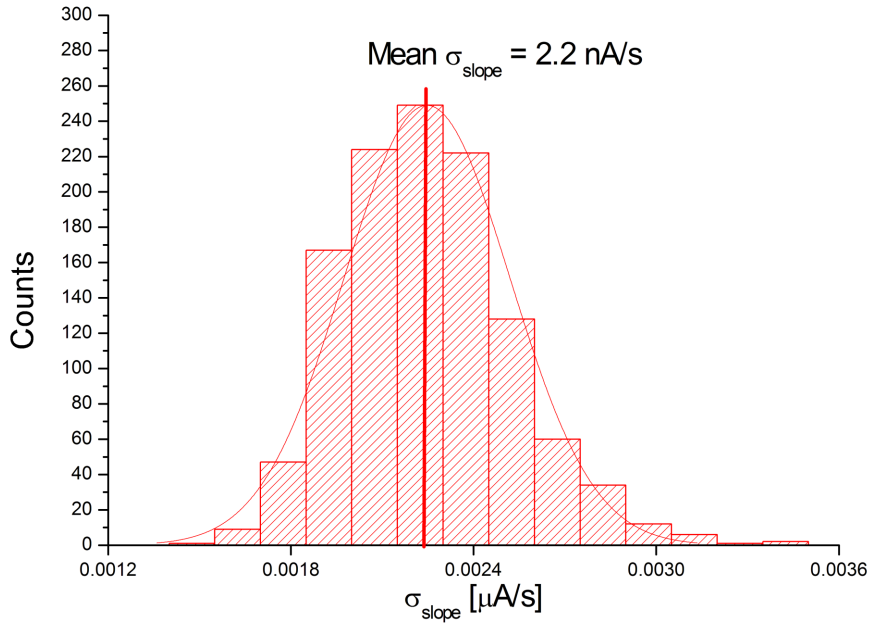
Figure 5.15: The mean individual error of the slope of each section.

the BCT [46]. The other alternative is to treat the data in an appropriate manner so as to suppress the influence of the 1/f noise in the data. This is discussed in the following sections.

5.2 FFT Correction Method

In view of the problems due to the influence of the 1/f noise on the slope, a correction method is needed to suppress the 1/f. Since this noise spectrum is defined in the frequency domain, it is convenient if the data are also represented in the frequency domain.

If the data in the time domain is represented by the straight line y(t)=a+bt, where a is the intercept and b is the slope, then the real and the imaginary parts of the fourier transform (f_n) of y(t) is given by (Refer Appendix F):

$$\Re(f_0) = Na + \frac{N(N-1)}{2}b \quad \text{only for n=0}$$

$$\Re(f_n) = -\frac{N}{2}b \quad \text{for } n > 0$$

$$\Im(f_n) = -\frac{N}{2}b\tan(\theta_n) \quad \text{for } n > 0 \tag{5.9}$$

where, N is the total number of data points in the time domain and n=1,2,3.....N/2 is the harmonic number and θ_n is the phase part. From these relationships, one can get information of the slope b and the intercept a in the frequency domain. If one uses the above equations as model functions, the intercept value can be derived from the real part and the slope from the imaginary part. These values correspond exactly to the results obtained from a linear fit in the time domain.

There are many methods and filters to suppress noise in the frequency domain. The most relevant in our context is the Optimal (Wiener) filtering method. In the Optimal Filtering method, the noise in the high frequency regime where the signal is zero is extrapolated to
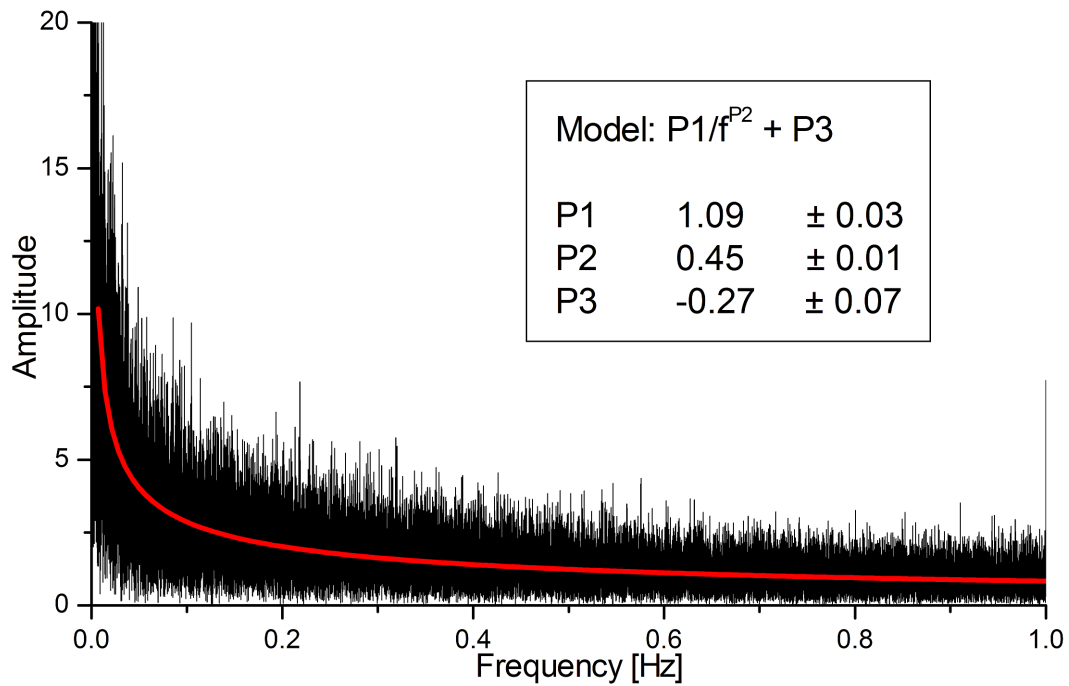
Figure 5.16: The FFT of the 1 mA data. The red line is a fit to the 1/f model function $y = P1/f^{P2} + P3$, where f is the frequency.
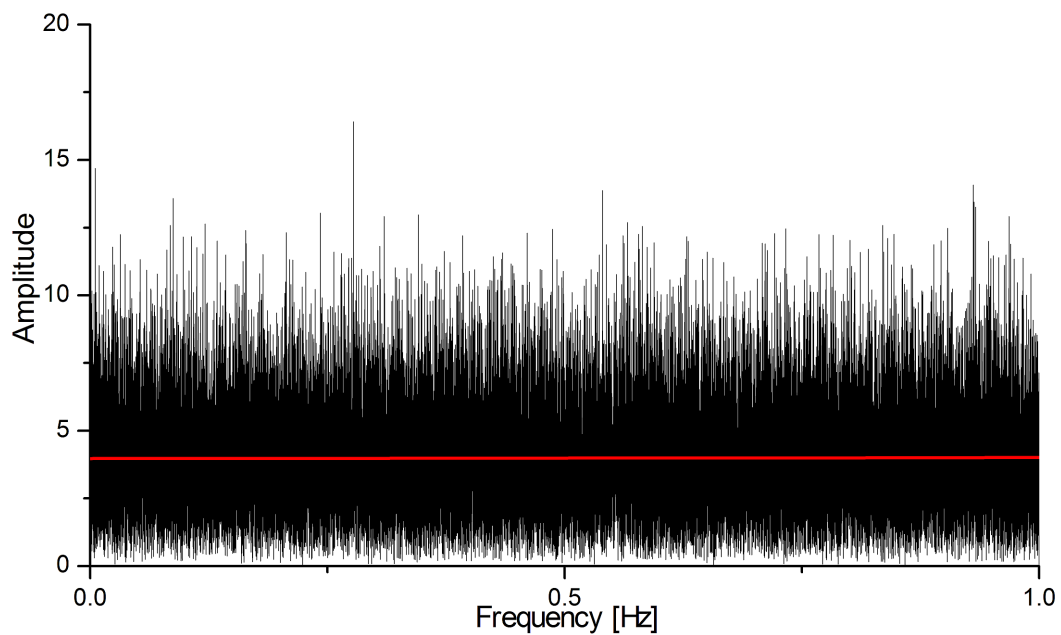
Figure 5.17: The FFT of a straight line with added white noise at a noise level at about 0.05 Hz of Figure 5.16.

all regions [47]. Using this information of the noise the useful signal can be filtered out from the corrupted signal. The optimal filter is given by:

$$\Phi(f) = \frac{|S(f)|^2}{|S(f)|^2 + |N(f)|^2} \tag{5.10}$$
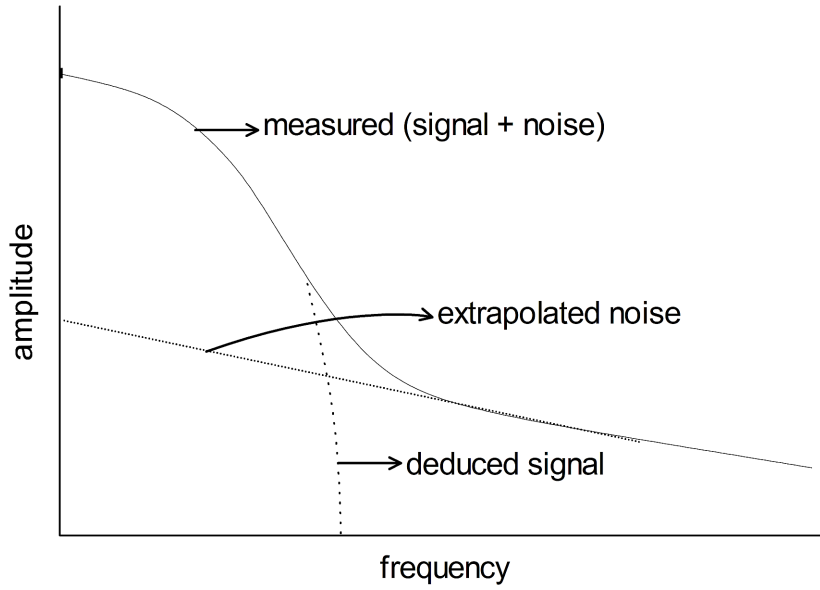
Figure 5.18: The FFT spectrum of the data shows a signal peak added to a noise tail. The tail is extrapolated back into the signal region as a "noise model". Subtracting gives the "signal model".

with S(f) as the true signal and N(f) as the noise in the signal. This is plotted in figure 5.18. The idea of optimal filtering can also be extended to the problem of 1/f noise. As seen from equation 5.9, the slope is found in all the harmonics. But in the case of the optimal filtering method the signal is zero in the high frequency part. Therefore, this method cannot be applied directly to the TRIC data and a new method had to be designed taking this into consideration. The important difference in using the frequency domain fitting is that one can appropriately weight the frequencies so that the effect of the low frequencies can be minimized while simultaneously keeping the slope by construction. Since only the slope of a straight line is obtained from the imaginary part, a direct way to obtain the lifetime value from the slope is to linearize the exponential behavior of the beam decay as follows. From equation (3.3),

$$I_n = I_0 \exp^{(\frac{-t}{\tau})}$$

Taking the logarithm of the above equation, we get,

$$ln(I_n) = ln(I_0) - \frac{t}{\tau} \tag{5.11}$$

This is a straight line equation where $ln(I_0)$ corresponds to the intercept and $-\frac{1}{\tau}$ to the slope. In this form, one can directly get the lifetime of the beam from the imaginary part of the FFT [1]

---

[1] The error in each data point in the linearised data σ_i' is related to the error in the original data σ_i as $\frac{\sigma_i}{y}$. Due to the very small slope in the TRIC data, this effect can be neglected.

5.3 The Weighted FFT Fit

As discussed above, the advantage of using the FFT fit, in the presence of 1/f noise, is the possibility to weight the individual frequency components appropriately. If the uncertainties in the data points are not all equal ($\sigma_n \neq \sigma$), we must include the individual standard deviations σ_n as weighting factors. The usual prescription for introducing weighting is to multiply each term in the sum in the χ^2 by $1/\sigma_n^2$ as shown in equation (F.11) [47]. The values of the σ_ns are not available a priori but have to be deduced in some way. Since, from the previous analysis, we know that the noise has a 1/f behavior, a possible method of suppressing the dominating lower frequencies is to weight the lower frequencies lower than the higher frequencies. Two methods were tried to deduce the weights for the individual frequencies. They are described below.

5.3.1 Weights from the Residuals

In this method, the residuals of the imaginary part of the FFT is taken, the residual R is the difference between the imaginary part of the harmonics f_n and the model function $y(a1, a2, ...)$ i.e.,

$$R_n = \Im(f_n) - y(a1, a2, ...) \tag{5.12}$$

From the residuals, an idea of the standard deviation of the individual points can be derived. Since the residuals are distributed about zero, the absolute value of the residuals of all the available datasets are taken and the mean at each frequency is calculated. This gives an idea of the standard deviation at each harmonic. The mean values are then fit to an 1/f model function of the form $\frac{p1}{n^{p2}} + p3$ where p1, p2 and p3 are the fit parameters. The index n, called the harmonic number is used for the sake of convenience in computations and calculations and is related to the frequency ν at the corresponding index by the relation:

$$\nu = \frac{n}{N\Delta t} \tag{5.13}$$

where, N is the number of data points in the time domain and Δt is the time interval between two datapoints in the time domain. These fit parameters are then used to generate the weights. If we have M datasets, then the mean of the residual at a particular harmonic n is:

$$\sigma_n \approx \frac{1}{M} \sum_{N=1}^{M} |R_{nN}| \tag{5.14}$$

The plot of σ_n at each harmonic is shown in figure 5.19

5.3.2 Weights from the Standard Deviation of the Data

Since we assume that the lifetime is a constant for a given polarization setup, the imaginary part of all the datasets should have the same value at each harmonic. But, the presence of noise would cause a distribution of these values. From the distribution, one can calculate the standard deviation at each harmonic. The parameters from a 1/f fit to these values are then used to generate the weights. If $\Im(f_{nN})$ is the imaginary part of the n'th harmonic in the N'th dataset then the standard deviation σ_n corresponding to that harmonic is given by the equation:

$$\sigma_n^2 = \frac{1}{M-1} \sum_{N=1}^{M} (\Im(f_{nN}) - \mu_n)^2 \tag{5.15}$$
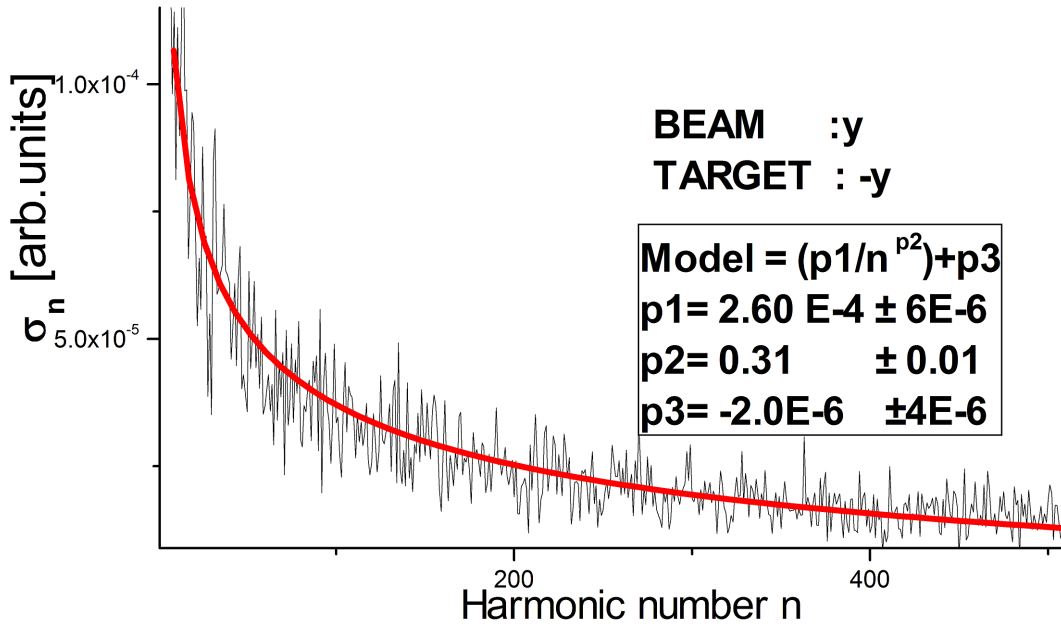
Figure 5.19: The weights from the of mean of residuals. The red line is a fit to the model function $\frac{p1}{n^{p2}} + p3$, where n is the harmonic number which is related to the frequency as given in equation 5.13.

where μ_n is the mean of the values $\Im(f_{nN})$ at a given harmonic n. M is the number of datasets. The above equation is the usual form for the estimate of the standard deviation of a given set of measurements. The 1/f fit values for all the configurations are presented in the tables 5.4 and 5.5. Using these weights, the lifetimes for each dataset were calculated for the various spin configurations of the beam and target. The mean lifetime obtained from the individual lifetime values are presented in table 5.6. The results for the two weighting methods (viz. Weights from Residuals and Weights from Standard Deviation) are comparable. However, the error of the lifetimes did not improve. Therefore, a more effective fitting method was needed to tackle the 1/f noise problem. In this context, the method of global fitting which has been reported to yield better results in measurements where some of the fit parameters are shared among datasets, was used along with the 1/f weighting method to improve the accuracy of the lifetime values.

Beam/Target	p1	p2	p3
- y/ + y	$2.40 \cdot 10^{-4} \pm 4 \cdot 10^{-6}$	0.28 ± 0.01	$3.0 \cdot 10^{-5} \pm 4 \cdot 10^{-6}$
+ y/ - y	$3.00 \cdot 10^{-4} \pm 6 \cdot 10^{-6}$	0.34 ± 0.01	$-2.0 \cdot 10^{-5} \pm 4 \cdot 10^{-6}$
- y/ - y	$2.60 \cdot 10^{-4} \pm 4 \cdot 10^{-6}$	0.31 ± 0.01	$-2.0 \cdot 10^{-5} \pm 4 \cdot 10^{-6}$
+ y/ + y	$3.40 \cdot 10^{-4} \pm 9 \cdot 10^{-6}$	0.50 ± 0.01	$1.5 \cdot 10^{-5} \pm 1 \cdot 10^{-6}$

Table 5.4: The 1/f fit parameters from the mean of residuals method. The fit function is of the form $\sigma_n = \frac{p1}{n^{p2}} + p3$, where n is the harmonic which is related to the frequency as given in equation 5.13.

Beam/Target	p1	p2	p3
- y/ + y	$6.60 \cdot 10^{-4} \pm 9 \cdot 10^{-6}$	0.70 ± 0.01	$1.0 \cdot 10^{-5} \pm 1 \cdot 10^{-6}$
+ y/ - y	$4.40 \cdot 10^{-4} \pm 8 \cdot 10^{-6}$	0.43 ± 0.01	$-1.0 \cdot 10^{-5} \pm 2 \cdot 10^{-6}$
- y/ - y	$4.00 \cdot 10^{-4} \pm 6 \cdot 10^{-6}$	0.45 ± 0.01	$-0.6 \cdot 10^{-5} \pm 2 \cdot 10^{-6}$
+ y/ + y	$5.60 \cdot 10^{-4} \pm 8 \cdot 10^{-6}$	$0.62 \pm 0 \cdot 01$	$1.0 \cdot 10^{-5} \pm 1 \cdot 10^{-6}$

Table 5.5: The 1/f fit parameters from the standard deviation of the data. The fit function is of the form $\sigma_n = \frac{p1}{n^{p2}} + p3$.

Beam/Target	Lifetime [h] using	
	Mean of residuals as weights	std.dev as weights
- y/ + y	45.49 ± 4.16	44.99 ± 3.15
+ y/ - y	42.39 ± 1.91	42.64 ± 2.21
- y/ - y	43.23 ± 1.70	43.21 ± 1.81
+ y/ + y	45.64 ± 3.89	47.07 ± 4.04

Table 5.6: The lifetime values obtained from the two weighting methods.

5.4 The Global Fitting Method

The global fitting method can be used to improve the precision of the results, when a parameter is shared among datasets. This method has been used successfully and reported in determining the fluorescence lifetime from a exponential decay curve [48, 49]. The basic idea behind the global fitting method is that the most probable value is best determined when all the available data are considered in the same fit and when extra information is available a priori. In the case of the TRIC experiment, the lifetime can be used as the shared parameter. The lifetime is now calculated taking all the datasets into account and using as an a priori information that the lifetime is constant. As opposed to normal fitting techniques, the global fitting method minimizes the sum of the χ^2 (Refer Appendix G). To incorporate the weighting for each dataset due to the varying intensity, the weighting methods previously described had to be modified. From the residual R of the imaginary part given in equation 5.12, the standard deviation of the fit σ can be calculated from the equation below:

$$\sigma^2 = \frac{1}{N} \sum_{n=1}^{N} R_n^2 \tag{5.16}$$

The residual is first binned using a constant window width. The standard deviation σ_{bin} is calculated for each bin. Assuming that the 1/f noise behavior to be the same in all the datasets. The ratio σ_{bin}/σ gives an idea of the fraction of the total standard deviation present in each of these bins. The ratio σ_{bin}/σ was fit to 1/f model function as described in the previous methods. Since σ_{bin}/σ is known from the fit parameters and σ is known from the last equation, the weight σ_n for each frequency can be calculated ($\sigma_{bin} \propto \sigma_n$). Since σ is different for different datasets (due to different intensities), σ_n will also differ accordingly, which takes care of the weighting due to the change in the intensity. The values of p1, p2 and p3 were approximately 5.6, 0.17 and -1.7 respectively for all the spin configurations (cf. Figure 5.20).

The global fitting method was also applied to the data with the target polarization in the x direction. This however did not correct the low lifetime values. As shown previously, this effect could be due to the emittance growth inside the ring. This growth is a function
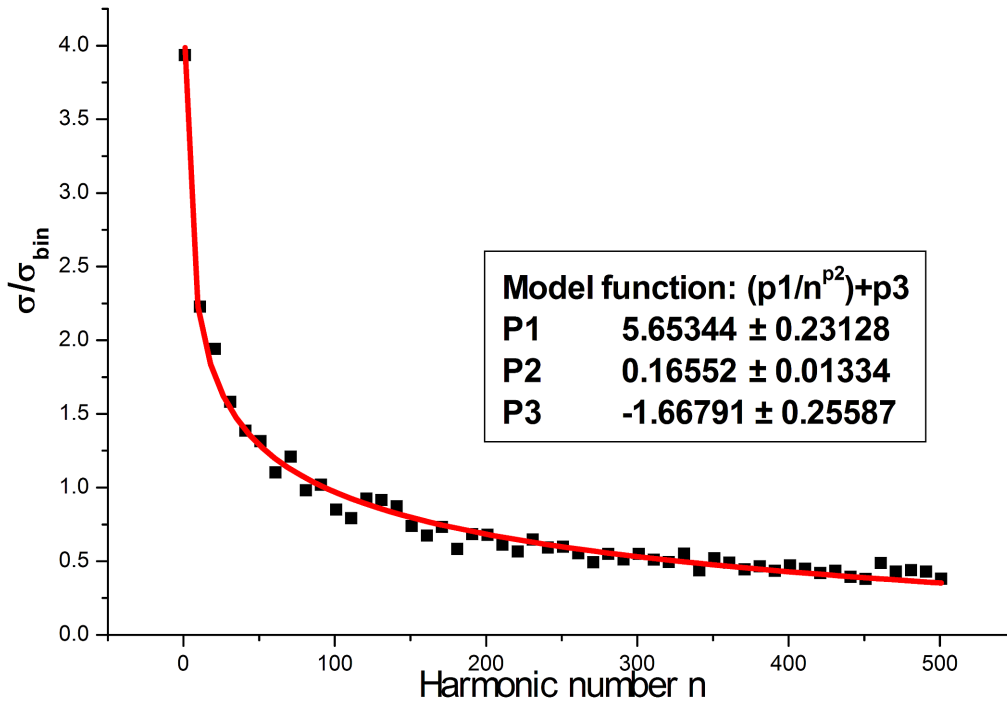
Figure 5.20: 1/f model fit to the ratio σ_{bin}/σ which takes the intensity fluctuations into account. The fit function is of the form $\sigma_n = \frac{p1}{n^{p2}}+p3$, where n is the harmonic which is related to the frequency as given in equation 5.13.

of the turn number. The decay curve can thus be corrected from this relationship but this is beyond the scope this work. A simple approximation is to assume that the decay to be parabolic. Each dataset was therefore fit to a parabola and the quadratic part was subtracted from the data. This data was then used in the global fitting method. The results are presented in table 5.7.

The results show that the parabolic subtraction has worsened the consistency in the lifetime values for the target $\pm y$ polarization. The lifetimes for the data without parabolic subtraction are more consistent within the same polarization configuration. The target x lifetime after the parabolic subtraction seems to be closer to the mean of the parallel and anti parallel lifetimes without parabolic subtraction. This shows that the parabolic subtraction is valid only for the last 20 minutes run section. Using the values in table 5.7 for the data without parabolic subtraction, the value of $A_{y,y}$ was calculated and found to be -0.09 ± 0.23 which corresponds to a value of -3.6 ± 9.2 mb of σ_{1tot}. The existing results of σ_{1tot} are plotted in figure 5.21. This value was calculated using the following equation:

$$A_{y,y} = \frac{\frac{1}{\tau^+} - \frac{1}{\tau^-}}{\frac{1}{\tau^+} + \frac{1}{\tau^-} - 2\frac{1}{\tau^{loss}}} \tag{5.17}$$

This is similar to equation 5.1 with the denominator now substituted by the sum of the inverse of the lifetimes. This avoids the necessity of knowing the uncertainty in the target thickness. However, the sum of the inverse of the measured lifetimes contains the loss lifetime $\frac{1}{\tau^{loss}}$ (representative of σ_{loss} in equation 3.4) which should be subtracted from

Beam/Target	Without parabolic subtraction	With parabolic subtraction
- y/ + y	41.29 ± 0.59	41.98 ± 0.54
+ y/ - y	41.54 ± 0.64	45.13 ± 0.75
Mean	41.41 ± 0.43	43.56 ± 0.46
- y/ - y	41.87 ± 0.59	44.56 ± 0.67
+ y/ + y	41.38 ± 0.62	42.28 ± 0.65
Mean	41.62 ± 0.42	43.42 ± 0.46
- y/ +x	37.98 ± 0.48	41.52 ± 0.54
+ y/ +x	35.46 ± 0.44	40.12 ± 0.65
Mean	36.72 ± 0.33	40.82 ± 0.42

Table 5.7: The Lifetime values in hours obtained using the global fitting method.

these values to get the actual lifetime τ^{target} [50]. That is,

$$\frac{1}{\tau^{target}} = \frac{1}{\tau^{\pm}} - \frac{1}{\tau^{loss}} \tag{5.18}$$

The value of the loss lifetime was measured to be $42.67 \pm 0.23h$. The value of σ_{1tot} is close to the existing results but though the error bar is large. It should be noted that this is due to the fact that the data were taken under poor experimental conditions with very little beam time and very low intensity.

The aim of the experiment was to test the achievable precision in the novel method. Therefore, the main concern was on the error budget and the inner consistency tests in the lifetime results namely the comparison of the parallel and anti-parallel configurations and the comparison with the unpolarized configuration.

The factors that contribute to the error bar in the value of σ_{1tot} are:

- Low Beam Intensity $\approx 0.5mA$ (an order of magnitude lower than the possiple space charge limit of COSY and that given in the proposal $\approx 50mA$.)

- Low target density $\approx 2 \cdot 10^{11} atoms/cm^2$ (a factor of 600 lower than given in the proposal $\approx 1.2 \cdot 10^{14} atoms/cm^2$.)

- Less Beam Time ≈ 1 day (an order of magnitude lower than given in the proposal-10 days).

- The presence of 1/f noise in the data which broadens the width of the distribution of lifetimes, which contributes a factor 3.

The error bar is a factor 3 worse than the expected value derived from equation 3.13. This is mainly caused by the large unexpected contribution of 1/f noise in the system.
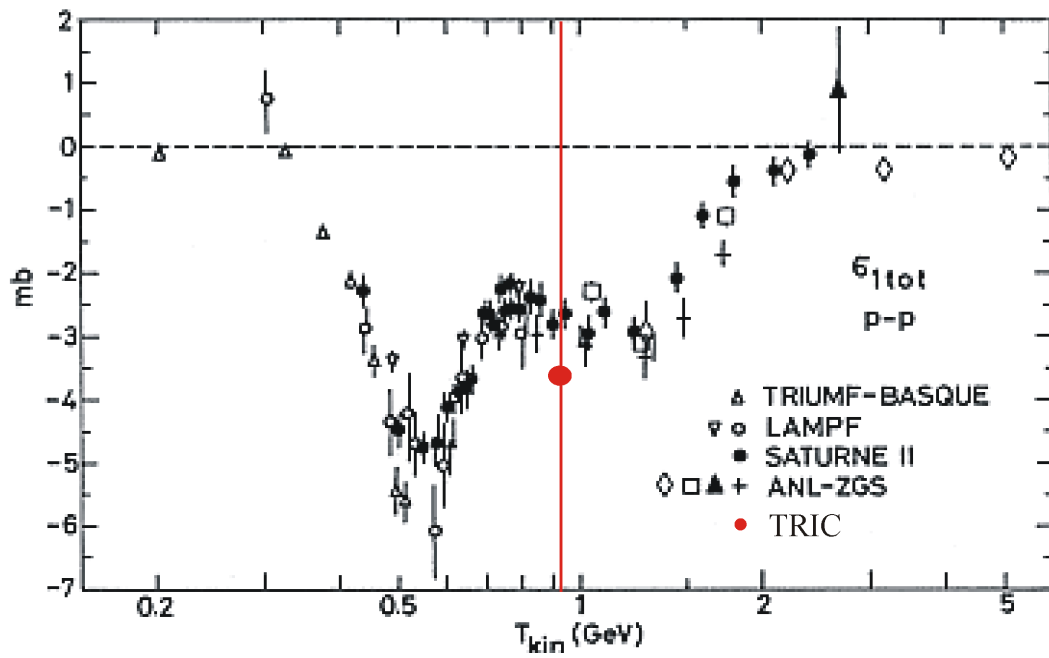
Figure 5.21: The existing results of $\sigma_{1tot} = A_{y,y}\sigma = -3.6 \pm 9.2$ mb[39].

6 Summary and Outlook

In this work, the feasibility of a novel high precision (10^{-6}) test of time reversal invariance has been tested in a measurement of the spin correlation coefficient $A_{y,y}$ in proton-proton (p-p) scattering. This measurement also tested a novel method to measure total cross section utilizing the optical theorem. The total cross section is measured by the slope of the beam current in forward scattering, the precision of which is governed ultimately by the current measuring device viz. the BCT.

The first step in this experiment was the construction of a hard real time data acquisition system under Windows-XP. The special features of the data acquisition are its Graphical User Interface, the Real-Time graphing interface and the remote control via internet. The determinism of the data acquisition was tested under extreme conditions and the operation of the data acquisition in several beam times was stable. Till date, no unconditional stops or crashes were encountered. The data acquisition system with its graphical user interface makes the control of the data acquisition simpler. The remote control feature helped in taking many parasitic measurements during other experiments like COSY11 and ANKE which gave insights into the general noise content and the behavior of the BCT.

For the intended precision of this experiment, a minimum of 10 days beam time is needed. The spin correlation coefficient $A_{y,y}$ is proportional to the difference in the inverse of the lifetime between the parallel and the anti parallel configurations of the polarization (Refer equation 5.1). Considering the noise contributions and the beam decay properties, an optimal measuring period of 1 hour was set for each run which was split into 3 run sections each of 20 minutes for each polarization setup.

The lifetime values and their errors were calculated for each of the 20 minute run sections. The accuracy of the lifetime values of the 20 minute run sections compared well with the expected values from the precision of the BCT. But, the accuracy of the mean lifetime obtained from the distribution of all the relevant 20 minute run were not consistent with the predictions from a single lifetime measurement. The error σ from the width of the lifetime distribution was about a factor 5 to 10 worse than the mean error of the lifetime $(\overline{\sigma})$. Due to fluctuating initial intensities of the beam, it is appropriate to consider the weighting of the lifetimes by their individual variances. The error of this weighted lifetime showed the improvement by a factor of $\sqrt{N}$ that was statistically expected. The reliability of the weighted lifetime values and the unweighted lifetime values was tested by a standard t-test at a significance level of $\alpha = 0.05$. It was seen that the difference between weighted lifetime of the same configuration (parallel/anti parallel) was very significant. The second inherent check for systematic errors, namely the value of the unpolarized lifetime (+x and -x), was seen to be lower than the other two configurations. This was attributed to the non-linear behavior of the beam decay in the last 20 minutes.

The sliding fit analysis revealed slow fluctuations in the data. The slow fluctuations play an important role in the distortion of the slope. The variation of the slope from one run to another can explain the discrepancy between the σ and $\overline{\sigma}$ found in the lifetime analysis. Various tests and analysis were made to further understand the cause of the

slow fluctuations. A constant current of 1 mA was passed through the calibration loop (cf. Figure 4.2) of the BCT and the analysis of this data also showed a similar discrepancy. The frequency spectrum of the data showed the presence of 1/f noise in the data. The following possible reasons for 1/f noise contributions were investigated:

- Fluctuations in the clock signal from the atomic clock.

- A current flowing through isolated part of the ring that passes through the BCT.

- Non-Linearities in the BCT or,

- The Barkhausen noise due to the domain wall motions in the ferrite core of the BCT.

The first two contributions were ruled out after systematic studies and analysis of the data. In a study using a modulated current 1 mA with a precision of $\approx 10^{-6}$, non-linearities in the gain of the BCT were revealed. This effect was corrected which still did not cure the effect of slow fluctuations in the noise. Thus the possible dominating cause of the slow fluctuations is the Barkhausen noise due to the domain wall motion in the ferrite core of the BCT. Thus these fluctuations are inherent in the measurements made by the BCT.

To suppress the 1/f noise in the data a method similar to the Optimal Filtering (Wiener-Khinchin) method was developed [47]. The Optimal Filtering method as such cannot be used for the TRIC data as it assumes that the actual signal power in concentrated in the low frequency regime only. In the case of TRIC data, the information of the slope is spread equally amongst all the harmonics. The fourier transform of a straight line was derived analytically. Thus, any deviation due to noise, especially in the low frequency part, can be easily detected. The new method weights each frequency components appropriately in order to suppress the dominating low frequency components. This method did not yield satisfactory results in terms of accuracy and so an alternative method was used. The frequency weighting technique was incorporated into an Global Fitting algorithm to improve the accuracy of the results [48][49]. The Global Fitting algorithm uses all the available data along with a-priori information (constant lifetime, for e.g) to optimize the parameters. The results were convincing in terms of consistency in the lifetimes of the parallel and anti parallel configurations. Though the accuracy is worse by a factor 3 than that was expected from basic statistics, it is substantially better than the accuracy of the unweighted lifetimes (from linear fit values, refer table 5.3). From the values of the lifetimes from the Global Fitting technique, the value of $A_{y,y}$ was calculated to be -0.09 ± 0.23, which corresponds to a value of -3.6 ± 9.2 mb of σ_{1tot}. The value is close to the existing results. It should be noted however that the large error bar is due to the fact that the data were taken under poor experimental conditions with very little beam time and very low intensity. An improvement in the intensity and the target thickness by a factor 10 would already improve the error by a factor 100 (refer equation C.9).

The aim of the experiment was to test the achievable precision in the novel method. In terms of accuracy, a single 20 minute run section compares well with an usual scattering experiment. The main concern was on the error estimates and the inner consistency tests in the lifetime results namely the comparison of the parallel and anti-parallel configurations and the comparison with the unpolarized configuration. It turned out that the error is worse by a factor 3 compared to the expectations from equation 3.13 which relates the accuracy to the experimental parameters and the basic noise from the BCT.

The error in the figure of merit is due to the following reasons:

- Low Beam Intensity $\approx 0.5mA$ (an order of magnitude lower than given in the proposal $\approx 50mA$.)

- Low target density $\approx 2 \cdot 10^{11} atoms/cm^2$ (a factor of 600 lower than given in the proposal $\approx 1.2 \cdot 10^{14} atoms/cm^2$.)

- Less Beam Time ≈ 1 day (also an order of magnitude lower than given in the proposal (10 days)).

- The presence of 1/f noise in the data which broadens the width of the distribution of lifetimes, which contributes a factor 3.

The first three contributions can be improved in the days to come which would improve the accuracy of the lifetime to the expectations. These poor conditions can be improved and tackled by well known techniques in the domain of accelerator physics. For instance, the implementation of a target cell, which would improve the target density, needs an installation of a minimum β section to avoid scattering from the cell walls. These factors depend in principle on the monetary support granted to the experiment. However, the presence of 1/f noise is conceptually a subject of concern. The extent of 1/f noise was unforeseen at the time of the planning of the experiment. This problem was later reported by another group but at a much lower precision and with larger 1/f noise contributions [37]. Due to the usage of the best quality BCT available then for the TRIC experiment, the noise contributions were substantially lower than that was reported by [37], which is also proved by the accuracy of the lifetime in the individual runs from our data. Nevertheless, the effect of 1/f noise from the BCT in high precision experiments like TRIC demands for a new avenue in improving the quality of the BCT in terms of the suppression of the 1/f noise. The possible cures to the problem of 1/f noise and its effect on the accuracy are:

- Usage of a non-ferrite magnetic core in the BCT.

- Usage of a BCT with further improved precision (better ferrites).

- Installing BCT's at multiple places in the ring and thus improving statistics.

The present frequency weighted global fitting algorithm yields convincing results with respect to consistency but with a compromise on the accuracy. With the improvements stated above, a better estimate of the figure of merit can be expected in the future. The values of the lifetimes correspond in all aspects to the expectations except for the enlarged error (by a factor 3) due to the 1/f noise contribution. Even this factor will vanish if the suggested improvements in the BCT design are realized.

A Polarization and Symmetry Properties

Vector Polarization

Any unequal population of magnetic substates (number of particles in a beam with spin up or spin down) represents a polarization. A proton beam with equal population of spin up and spin down states is unpolarized. A proton beam in only one substate (spin up or spin down) has a maximal vector polarization. In general the vector polarization of a spin $\frac{1}{2}$ ensemble can be represented as follows:

$$p = \frac{1}{A(\theta)} \frac{N^+ - N^-}{N^+ + N^-} \tag{A.1}$$

with $A(\theta)$ being the analysing power discussed in the subsequent sections and $N^{+(-)}$ is the number of particles in the spin up (spin down)substate.

Tensor Polarization

A spin 1 particle has 3 (2S+1) sub states namely up, down and zero. Assume all particles in the beam in the spin "zero" state are eliminated. According to the general definition of polarization given above we know this beam is polarized. On the other hand from the special definition of vector polarized protons we are lead to assume this beam is unpolarized. Therefore, this type of polarization is called tensor polarization. The tensor polarization of rank 2 is given by the difference of the population of the magnetic substates N+ and N- with respect to the population of state N^0, normalized to the particles in the beam.

$$p_{tensor} = \frac{(N^+ - N^0) + (N^- - N^0)}{N^+ + N^- + N^0}$$

where, N^0 is the number of particles in the zero substate. Consequently, the vector polarization for a spin 1 particle is extended to

$$p_{vector} = \frac{N^+ - N^-}{N^+ + N^- + N^0}$$

Polarization in Quantum Mechanics

Polarization is defined to be the expectation value of the spin operator which are expressed by the Pauli spin matrices for spin $\frac{1}{2}$ particles. The polarization of a spin $\frac{1}{2}$ particle is represented by the Pauli spin matrices viz.,

$$\sigma_x = \frac{1}{2} \begin{pmatrix} 0 & 1 \\ 1 & 0 \end{pmatrix}, \sigma_y = \frac{1}{2} \begin{pmatrix} 0 & -i \\ i & 0 \end{pmatrix} \sigma_z = \frac{1}{2} \begin{pmatrix} 1 & 0 \\ 0 & -1 \end{pmatrix}$$

A spin 1 particle has 3 spin substates and the polarization is specified by the vector (rank 1) operators $\mathbf{P}_x, \mathbf{P}_y$ and $\mathbf{P}_z$ and the tensor (rank 2) operators $\mathbf{P}_{xx}$, $\mathbf{P}_{yy}$, $\mathbf{P}_{zz}$, $\mathbf{P}_{xy}$, $\mathbf{P}_{xz}$

and $\mathbf{P}_{yz}$ [23][51]. The vector polarization components are given below.

$$\mathbf{P}_x = \frac{1}{\sqrt{2}} \begin{pmatrix} 0 & 1 & 0 \\ 1 & 0 & 1 \\ 0 & 1 & 0 \end{pmatrix}, \mathbf{P}_y = \frac{1}{\sqrt{2}} \begin{pmatrix} 0 & -i & 0 \\ i & 0 & -i \\ 0 & i & 0 \end{pmatrix}, \mathbf{P}_z = \frac{1}{\sqrt{2}} \begin{pmatrix} 1 & 0 & 0 \\ 0 & 0 & 0 \\ 0 & 0 & -1 \end{pmatrix},$$

The tensor polarization components are[23]:

$$\mathbf{P}_{xy} = \frac{3i}{2} \begin{pmatrix} 0 & 0 & -1 \\ 0 & 0 & 0 \\ 1 & 0 & 0 \end{pmatrix}, \mathbf{P}_{xz} = \frac{3i}{\sqrt{8}} \begin{pmatrix} 0 & -1 & 0 \\ 1 & 0 & 1 \\ 0 & -1 & 0 \end{pmatrix}, \mathbf{P}_{yz} = \frac{3i}{\sqrt{8}} \begin{pmatrix} 0 & 1 & 0 \\ 1 & 0 & -1 \\ 0 & -1 & 0 \end{pmatrix},$$

$$\mathbf{P}_{xx} = \frac{1}{2} \begin{pmatrix} -1 & 0 & 3 \\ 0 & 2 & 0 \\ 3 & 0 & -1 \end{pmatrix}, \mathbf{P}_{yy} = \frac{1}{2} \begin{pmatrix} -1 & 0 & 3 \\ 0 & 2 & 0 \\ -3 & 0 & -1 \end{pmatrix}, \mathbf{P}_{zz} = \frac{1}{2} \begin{pmatrix} 1 & 0 & 0 \\ 0 & -2 & 0 \\ 0 & 0 & 1 \end{pmatrix},$$

These set of operators along with the unit matrix form an overcomplete set which are retained as such for the sake of convenience [23].

The Analysing Power and Spin Correlation Coefficient

Consider the scattering of the form $\vec{\frac{1}{2}} + A \rightarrow \vec{\frac{1}{2}} + B$. The spinor χ_i describing the incoming spin $\frac{1}{2}$ particle is related to the spinor χ_f of the outgoing spin $\frac{1}{2}$ particle by the following relation[23]:

$$\chi_f = M\chi_i$$

where M is a 2 x 2 is the transition matrix whose elements are functions of energy and angle. The density matrix describing the initial state is:

$$\rho_i = \sum_{n=1}^{N} \chi_i^{(n)} [\chi_i^{(n)}]^\dagger$$

The final state density matrix can be defined as

$$\rho_f = M\rho_i M^\dagger$$

The differential cross is then given by:

$$I(\theta, \phi) = Tr[\rho_f] = Tr[M\rho_i M^\dagger]$$

with $I(\theta, \phi)$ being the differential cross section for a polarized beam. If the beam is unpolarized, the initial state density matrix is given by:

$$\rho_i = \frac{1}{2} \begin{pmatrix} 1 & 0 \\ 0 & 1 \end{pmatrix}$$

The corresponding unpolarized cross section is given by

$$I_0(\theta) = \frac{1}{2} Tr[MM^\dagger]$$

The density matrix can be expressed in terms of the Paulis matrices σ_j and their expectation values p_j as

$$\rho_i = \frac{1}{2}(1 + \sum_{j=1}^{3} p_j \sigma_j)$$

and so the final state density matrix can be written as

$$\rho_f = \frac{1}{2}MM^\dagger + \frac{1}{2}\sum_{j=1}^{3}p_j M\sigma_j M^\dagger$$

This gives,

$$I(\theta,\phi) = Tr[\rho_f] = I_0(\theta)(1 + \sum_{j=1}^{3}p_j A_j(\theta))$$

with:

$$A_j(\theta) = \frac{Tr[M\sigma_j M^\dagger]}{Tr[MM^\dagger]}$$

$A_j(\theta)$ is called the analysing power. In case the target is polarized the density matrix is written as a direct product of the beam density matrix and the target density matrix and the cross section involves terms containing the analysing power of the target and cross terms. In general the differential cross section can be written as:

$$I(\theta,\phi) = Tr[\rho_f] = I_0(\theta)(1 + \sum_{j=1}^{3}p_j A_j(\theta) + \sum_{j=1}^{3}p_j^T A_j^T(\theta) + \sum_{j,k}p_j p_k^T A_{j,k}(\theta))$$

where,

$$A_{j,k}(\theta) = \frac{Tr[M\sigma_j\sigma_k^\dagger M^\dagger]}{Tr[MM^\dagger]}$$

$A_{j,k}$ is called the spin correlation coefficient.

General Symmetry Rules For Polarization Observables Written in Terms of the Invariant Amplitudes

In the simplest case consider the reaction $\frac{1}{2} + 0 \rightarrow \frac{1}{2} + 0$. The scattering matrix can be written in terms of the invariant amplitudes a_j's:

$$M(\theta) = \sum_j a_j(\theta)\sigma_j \tag{A.2}$$

where, j = 0,x,y,z, $\sigma_0 = 1$. In general, a polarization observable is denoted by X_{pqik}, with X defining the observable (eg., A for Analysing Power and C for Spin Correlation Coefficient etc.,) and p,q,i and k define the ejectile, recoil, projectile (beam) and the target polarizations respectively. In the projectile helicity frame, these can take values like x,y,z or 0. In the following definitions, the notation n_m refers to the number of times the subscript m occurs in an observable. For the observable $A_{y,xz}$ $n_x = n_y = n_z = 1$.

The following transformations are obtained under P, T operations [18].

$$P : \sigma_x, \sigma_y, \sigma_z \rightarrow -\sigma_x, \sigma_y, -\sigma_z;$$
$$T : \sigma_x, \sigma_y, \sigma_z \rightarrow -\sigma_x, \sigma_y, \sigma_z;$$

Thus the M matrix amplitudes in A.2 and in $M^t = \sum_j a_j^t(\theta)\sigma_j$, the M in the inverse reaction, can be classified according to their P and T symmetries as follows [18]:

$$P : a_j = (-1)^{(n_x+n_z)}a_j \tag{A.3}$$
$$T : a_j = (-1)^{n_x}a_j^t$$

Similarly, the observables namely the analysing powers and the spin correlation coefficients, which are usually expressed as a bilinear combination (bicoms) of these amplitudes can be classified according to their P and T symmetry.

$$P : A_{j,k} = (-1)^{(n_x+n_z)}A_{j,k} \tag{A.4}$$
$$T : A_{j,k} = (-1)^{n_x}A_{k,j}^t$$

The rules based on these relationships are as follows[23]:

Parity Conservation

Conservation of parity requires that an observable vanishes unless the corresponding sum $n_x + n_z$ is an even number. So PC requires a P-odd observable to be zero.

Time Reversal Invariance

Time reversal invariance requires that the polarization transfer coefficients of the inverse reaction be $(-1)^{n_x}$ times the corresponding coefficients of the forward reaction, provided the CM helicity frames are used. Thus this rule requires that an observable be equal to $(+/-)$ a different observable in the inverse reaction.

Rotational Invariance

Rotation invariance requires an observable to be an odd (even) function of the scattering angle θ if $n_x + n_y$ is odd (even).

Therefore, for an observable to be T-odd, P-even and rotationally invariant, the minimum number of indices required is $n_x = n_y = n_z = 1$. The figure of merit $A_{y,xz}$ satisfies this condition.

B Circuit Diagrams
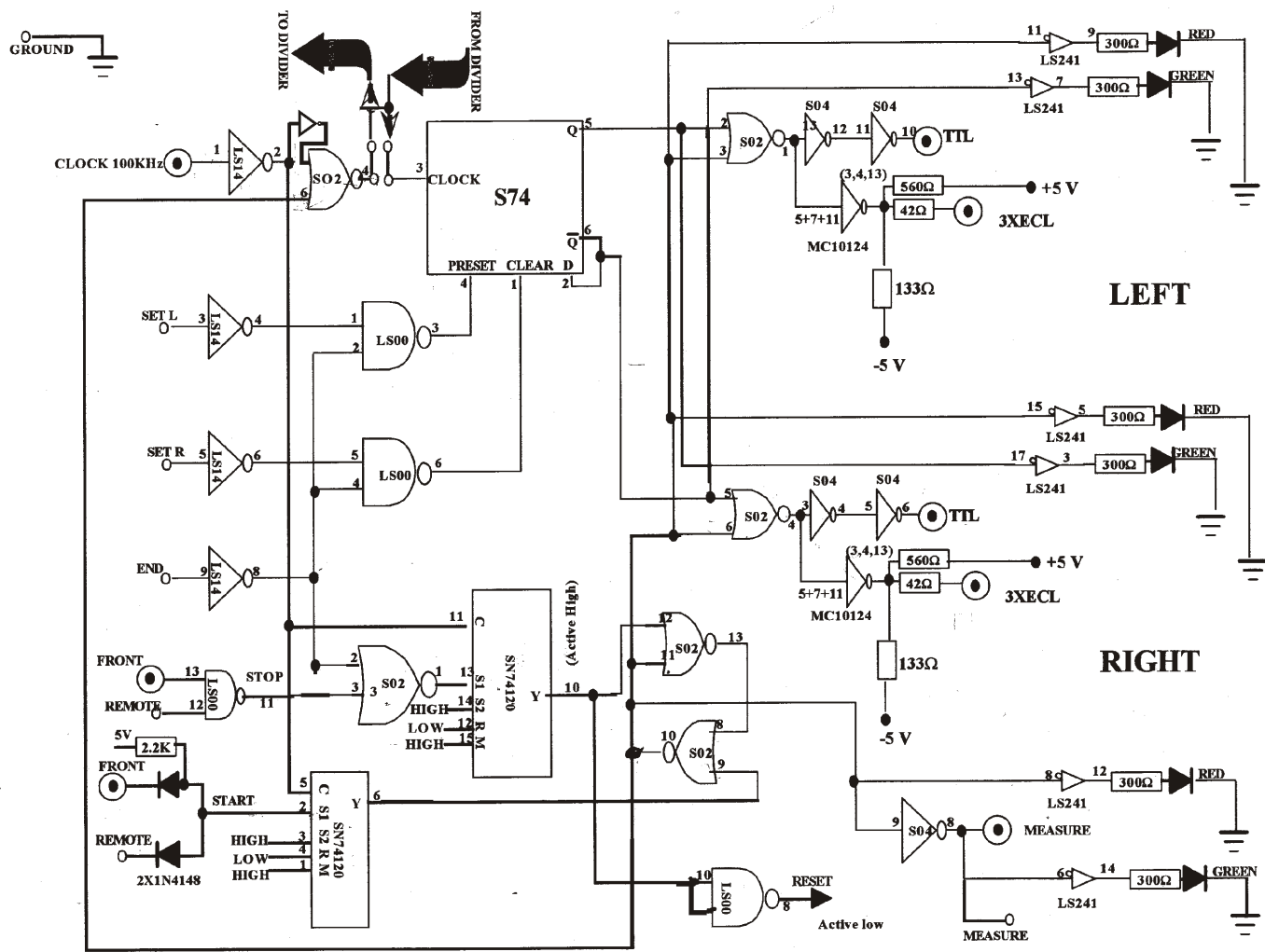
Figure B.1: The TRIC timer module part 1
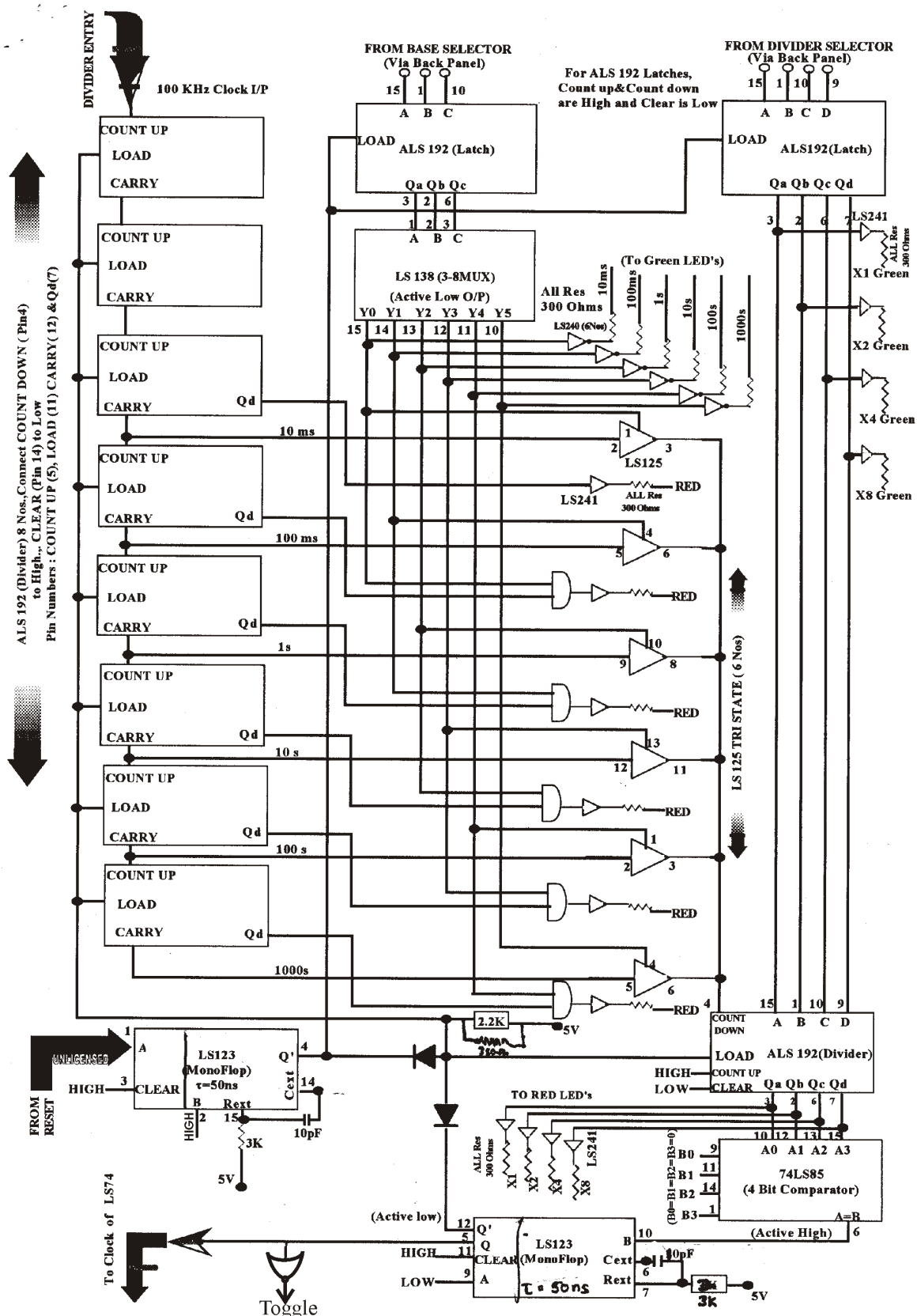
Figure B.2: The TRIC timer module part 2

Figure B.3: BCT MODULATOR

10 V ext

15K

15 V
Vcc

2   AD 780
       PRECISION
       VOLTAGE
       REFERENCE
       2.5 V

6   EXT
    INT

4

GND MECCA

5K
POT

10K

1µF

500 Ohms
Prec. Resistor
Tk = 3ppm/°c

TO GND
MECCA

OP
27

2

3   6

R⊙   A
        A'

L⊙   B
        B'

74 LS 14

MAX 314
1
2
16
15
5
6
9
11

⊙ OUT

24V

GND

TRACO
DC/DC
CONVERTOR

+15V

10µF

10µF

0V

0.2µF

0.2µF

-15V

R

GND
MECCA

5V

0.2µF

POWER SUPPLY CONNECTIONS
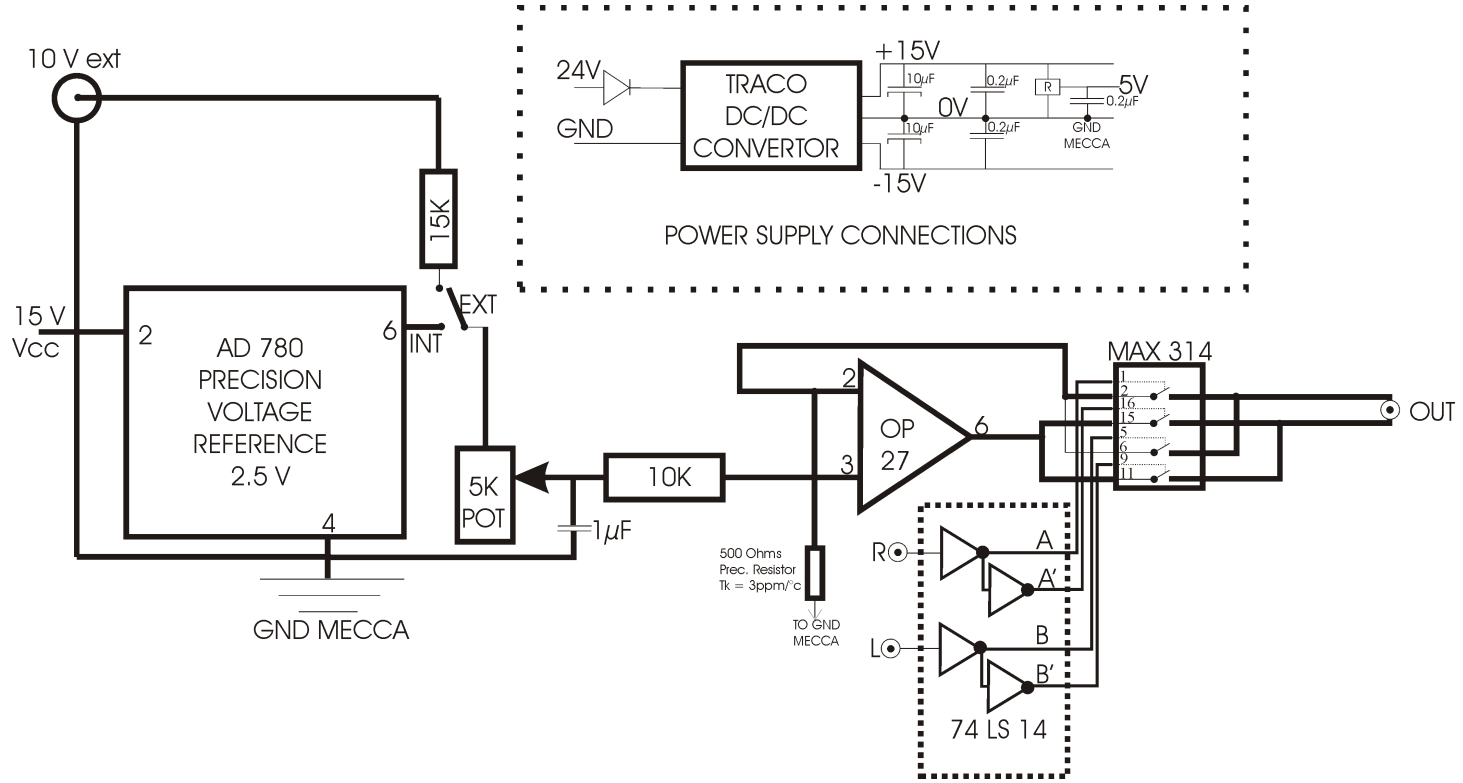
C Accuracy of the Figure of Merit in Terms of the Spin Flip Period and Beam Time

The accuracy of the figure of merit depends on the accuracy with which the slope of the current is determined. Assuming a linear decay of the beam, an equation that relates the accuracy of the slope of the current to the accuracy of the figure of merit in terms of the beam time and the spin flip period is presented in this appendix.

The estimated error in the parameters I_0 and b of a straight line of the form $I = I_0 + bt$ are given by the $\sigma_{I_0} = \sigma_I/\sqrt{k}$ and $\sigma_b = \sigma_I/\sqrt{\Sigma t_k^2}$, with k being the number of data points and t_k s are the independent time values [38]. σ_I is the standard deviation of a single current measurement (typically $0.5\mu A$ in 1s integration time given in the Bergoz Current Transformer (BCT) device manual). The accuracy in the slope can be simplified further by considering that the data points are acquired at equal time intervals so that the independent values of time can be replaced by $\Delta t * k$, where Δt is the time interval between any two consecutive data points and i, the sequential index of the data point. Since $\Sigma k^2 \approx k^3/3$, the accuracy in the slope b can be written as:

$$\sigma_b = \frac{\sqrt{3}\sigma_I}{\Delta t k^{1.5}} = \frac{\sqrt{3}\sigma_I}{t\sqrt{k}} \text{(Since } \Delta tk = t) \tag{C.1}$$

If we combine N measurements of the slope b then the accuracy of the slope is improved by a factor $\sqrt{N}$.

$$\sigma_b = \frac{\sqrt{3}\sigma_I}{\Delta t k^{1.5}} \frac{1}{\sqrt{N}} \tag{C.2}$$

From Chapter 3, the figure of merit is given as:

$$A_{y,xz} = \frac{1}{2\sigma\rho \; d\nu p_y p_{xz}}[\frac{1}{\tau^+} - \frac{1}{\tau^-}] \tag{C.3}$$

From equation (C.3), an estimate of the accuracy $\delta A_{y,xz}$ of $A_{y,xz}$ can be derived from error propagation. Assuming that the pre-term in (C.3) to be constant, the accuracy of the figure of merit depends on the accuracy of the inverse of the lifetime $\sigma_{1/\tau}$. Since $\tau = I_0/b$ the error in the inverse of the lifetime is given by [1]

$$\sigma_{1/\tau} = \frac{1}{\tau}\sqrt{\frac{\sigma_{I_0}^2}{I_0^2} + \frac{\sigma_b^2}{b^2}} \tag{C.4}$$

For currents in the order of 50 mA and with the precision of the current measurement used in the experiment, the ratio $\sigma_{I_0}^2/I_0^2$ can be neglected. The main contribution to the error of the inverse of the lifetime is from the slope of the current and so,

$$\sigma_{1/\tau} \approx \frac{\sigma_b}{I_0} \tag{C.5}$$

---

[1] Error propagation formulas: If $x = au + bv$ then, $\sigma_x^2 = a^2\sigma_u^2 + b^2\sigma_v^2$.

If $x = \frac{au}{v}$ then, $\frac{\sigma_x^2}{x^2} = \frac{\sigma_u^2}{u^2} + \frac{\sigma_v^2}{v^2}$ where, a and b are constants and the covariances are assumed to be zero.

The accuracy of the figure of merit reduces to:

$$\delta A_{y,xz} = \frac{1}{(\sqrt{2}I_0\sigma\rho d\nu p_y p_{xz})}\sigma_b \tag{C.6}$$

The factor $\sqrt{2}$ is due to the addition of two equal uncertainties from the error propagation formulas. If we have a total of H hours of beam time and if the spin is flipped every h hours, so that we have H/2h measurements of the slope for each spin configuration, and if we have k data points in h hours, then using equations (C.2),(C.5) and (C.6),

$$\delta A_{y,xz} = \frac{1}{(I_0\sigma\rho d\nu p_y p_{xz})}\sqrt{\frac{h}{H}}\frac{\sqrt{3}}{\Delta t k^{1.5}}\sigma_I \tag{C.7}$$

Since $\Delta k = 3600h$ (in seconds), $\sqrt{k} = 60\sqrt{h/\Delta t}$ and therefore:

$$\delta A_{y,xz} = \frac{8\cdot 10^{-6}}{(I_0\sigma\rho d\nu p_y p_{xz})}\frac{\sqrt{\Delta t}}{h\sqrt{H}}\sigma_I \tag{C.8}$$

Where I_0 is the current in amperes, σ_0 is the cross section in cm^2, ν is the beam circulation frequency in Hz, ρd is the thickness of the target in atoms/cm^2, p_y, p_{xz} are the polarization of the beam and target respectively. H is the total beam time in hours and h is the spin flip period. Δt is the time interval between two consecutive data points in seconds. The precision of the BCT is a quantity that is dependent on the integration time and so this factor should also be taken into account in the calculation of the accuracy of the figure of merit. In general, from the resolution of the BCT in 1s integration time, the precision of the BCT in a given integration time Δt can be written as:

$$\sigma_I = \frac{0.5}{\sqrt{\Delta t}}\mu A \tag{C.9}$$

Using this in equation (21), we get,

$$\delta A_{y,xz} = \frac{4\cdot 10^{-12}}{(I_0\sigma\rho d\nu p_y p_{xz})}\frac{1}{h\sqrt{H}} \tag{C.10}$$

In equation (C.9), the dimension of the noise has the unit of current though it is normalised by the integration time factor. This factor numerically cancels the time factor in the numerator of equation (C.8),but the dimensions stay as such. In equation (C.10), the units for the terms involved is given in the following table.

Quantity	Unit
I_0	A
σ	cm^2
ρd	$atoms/cm^2$
ν	Hz
h and H	hours

The terms and their units as used in equation (C.10).

D The Real-Time Extension Programming

The Real time Kernel (RTX) provides an essential set of real-time programming interfaces in the Win32 environment. The RTX interfaces are compatible with the Win32 programming interfaces. In addition, RTX provides extensions to Win32 in order to provide a complete set of real-time functions to the application programmer. RTX application programs can use the real-time extensions in both the Win32 (non-deterministic) and Real-Time Sub System (RTSS) environments (deterministic) and programs can use the Win32-supported API (Application Programming Interface) in the RTSS environment. The RTX API is based on the Win32 API. This approach allowed us to draw upon our Win32 experience, code base, and development tools, thus expediting hard real-time application development. Both Win32 and RTSS processes support the full RTX API, however, with different response times and performance characteristics which allowed us to effortlessly share or move code between environments.

RTX supports a subset of Win32 API functions, plus it provides a special set of real-time functions, known as Real-Time API (RTAPI). RTAPI functions are identified by an "Rt" prefix in their names. Some RTAPI functions are semantically identical to their Win32 counterparts, while others are unique to RTX (i.e., there are no similar Win32 calls). For example, RTAPI real-time IPC (Inter Process Communication) functions differ from Win32 IPC functions only in the IPC name space in which they operate and in the determinism possible with real-time IPC objects. On the other hand, the Win32 API does not include any functions related to interrupt management; therefore, unique interrupt management functions are defined in RTAPI. The RTX API was carefully selected to promote efficient development of real-time application components.

RTX intentionally does not include Win32 functions, such as the GUI (Graphical User Interface) related calls, that are normally used by the less time-critical components of an application. In general, Win32 functions that are not essential to real-time programming, and impractical to implement with deterministic behavior, are not included in the RTX API.

E Encoding and Decoding of Data

The data acquired from the TRIC data acquisition system was encoded with unique identification tags to make the source and the time stamp of each individual data point. The encoding procedure enables one to identify the exact origin of the data. The details are presented in this appendix. Each dataset at present contains 18 (time + 12 scaler channels + 5 input/output modules) data of type ULONG (32 bits). The encoded data structure for the time stamp is as follows. If bits 28-31 (4 bits), the identification tags, are all 1's then this indicates that this data is a time stamp. If bit 27 (1 bit) is 0 the data is from the left scaler, 1 if it is from the right scaler, bit 0-26 are the 27 bits of the time stamp in milliseconds. The encoded data structure for the data from scalers and other input/output modules is as follows. The Identification tag for the data from the CAMAC contains 8 bits but range only from 0-239 in order to avoid mixed use with the Identification tag for the time. The rest 24 bits contain the data from the CAMAC. These are described in the table below

Bit(s)	31-28	27	26-0
Data	all 1	0 (1)for Scaler Left (right)	Time stamp in milliseconds

Table E.1: The encoded data structure for time

Bit(s)	31-24	23-0
Data	Identification tag for CAMAC module	CAMAC data

Table E.2: The encoded data structure for data from the scalers and other CAMAC modules. Bits 31-28 can vary only from 0000 to 1110.

F FFT of a Straight Line

The discrete fourier transform is described by the series [47]:

$$f_n = \sum_{k=0}^{N-1} y_k e^{\frac{2\pi itn}{N}} \tag{F.1}$$

where, y is the time series data and n is the harmonic number. If the data are sampled at regular intervals of time, $y_k = y(t_k)$ where, $t_k \equiv k\Delta t$. Δt is the sampling interval and k = 0,1,2...N-1. N is the total number of datapoints in the time domain. For a straight line of the form $y(t) = a + bt$, the fourier transform is given by

$$f_n = \sum_{k=0}^{N-1} (a + bk) e^{\frac{2\pi ikn}{N}} \tag{F.2}$$

The above equation can be derived by substituting $y_k = a + b \cdot k\Delta t$ in equation (F.1) and assuming Δt to be 1. The above equation is written as a sum of real and imaginary components as:

$$f_n = \sum_{k=0}^{N-1} (a + bk)cos\frac{2\pi kn}{N} + i \sum_{k=0}^{N-1} (a + bk)sin\frac{2\pi kn}{N} \tag{F.3}$$

The DC component in the frequency domain corresponds to n=0. Substituting n = 0 in equation (F.3), the imaginary part becomes zero and so we get:

$$f_0 = a + (a + b) + (a + 2b) + ... + (a + (N - 1)b) = Na + \frac{N(N - 1)}{2}b \tag{F.4}$$

The other components (i.e $n \neq 0$) can be written as:

$$\Re\{f_n\} = a \sum_{k=0}^{N-1} cos\frac{2\pi kn}{N} + b \sum_{k=0}^{N-1} kcos\frac{2\pi kn}{N}$$

$$\Im\{f_n\} = a \sum_{k=0}^{N-1} sin\frac{2\pi kn}{N} + b \sum_{k=0}^{N-1} ksin\frac{2\pi kn}{N} \tag{F.5}$$

The first terms in equation (F.5) are equal to the real and imaginary part of

$$a \sum_{k=0}^{N-1} e^{\frac{2\pi ikn}{N}}$$

respectively. Using formulas (a) and (b) found at the end of this section, we get,

$$\Re\left\{\sum_{k=0}^{N-1} e^{\frac{2\pi ikn}{N}}\right\} = \frac{cos\frac{2\pi n(N-1)}{N}sin\pi n}{sin\frac{\pi n}{N}}$$

$$\Im\left\{\sum_{k=0}^{N-1} e^{\frac{2\pi ikn}{N}}\right\} = \frac{sin\frac{2\pi n(N-1)}{N}sin\pi n}{sin\frac{\pi n}{N}} \tag{F.6}$$

$sin(\pi n)$ is zero for all integral values of n. So the real and imaginary parts in equation (F.6) are zero, which makes the first term (of the real and imaginary part) in equations (F.5) zero). The second term in equations (F.5) are simplified and presented below. The second term in the real part in equation (F.5) reduces to:

$$\frac{Ncos\frac{2n\pi}{N} - N}{4sin^2(\frac{n\pi}{N})}$$

$$= \frac{N(cos^2(\frac{\pi n}{N}) - sin^2(\frac{\pi n}{N}) - 1)}{4sin^2(\frac{\pi n}{N})}$$

$$= \frac{-2Nsin^2(\frac{\pi n}{N})}{4sin^2(\frac{\pi n}{N})}$$

which implies,

$$\Re\{f_n\} = -\frac{N}{2}b \ \ (n \neq 0) \tag{F.7}$$

The second term in the imaginary part in equation (F.5) reduces to:

$$\frac{-Nsin\frac{2n\pi}{N}}{4sin^2(\frac{n\pi}{N})}$$

$$= \frac{-2Nsin\frac{n\pi}{N}cos\frac{n\pi}{N}}{4sin^2(\frac{n\pi}{N})}$$

which gives,

$$\Im\{f_n\} = -\frac{N}{2}tan(\theta_n)b \ \ (n \neq 0) \tag{F.8}$$

where $\theta_n = 90 + \frac{n \cdot 180}{N}$ (in degrees).

The sampling interval Δt is a constant and so the above results are equally valid even if $\Delta t \neq 1$ except that the slope b is multiplied by this sampling interval. The resulting equations are

$$\Re\{f_n\} = -\frac{N}{2}b\Delta t \ \ (n \neq 0) \tag{F.9}$$

and

$$\Im\{f_n\} = -\frac{N}{2}tan(\theta_n)b\Delta t \ \ (n \neq 0) \tag{F.10}$$

The following formulas were useful in deriving the above results.

$$(a) \sum_{n=0}^{N} cosnx = \frac{cos\frac{Nx}{2}sin\frac{(N+1)x}{2}}{sin\frac{x}{2}}$$

$$(b) \sum_{n=0}^{N} sinnx = \frac{sin\frac{Nx}{2}sin\frac{(N+1)x}{2}}{sin\frac{x}{2}}$$

$$(c) \sum_{k=0}^{N-1} kcos\frac{2nk\pi}{N} = 1/4((1-N)cos(2n\pi) - 1 + Ncos(\frac{2n(N-1)\pi}{N}))cosec(\frac{n\pi}{N})^2$$

$$(d) \sum_{k=0}^{N-1} ksin\frac{2nk\pi}{N} = -1/4((N-1)sin(2n\pi) + Nsin(\frac{2n(N-1)\pi}{N}))cosec(\frac{n\pi}{N})^2$$

The Most Probable Slope

Using equation (F.8) as the model function, the most probable slope can be found by minimizing the χ^2 with respect to the slope b, i.e. if the imaginary part of the fourier transform of our data is given by Y_n, then

$$\chi^2 = \sum_{n=0}^{N/2} \frac{(Y_n - \Im(f_n))^2}{\sigma_n^2} \tag{F.11}$$

where, $\Im(f_n)$ is the imaginary part of the fourier transform as defined in equation (F.8) and σ_n is the uncertainty of a single datapoint and N the total number of datapoints in the time domain. Due to the symmetric behavior of the fourier components, the summation is restricted to N/2. The most probable value of the slope b is obtained by solving,

$$\frac{\partial \chi^2}{\partial b} = \sum_{n=0}^{N/2} \frac{(Y_n + b \cdot \tan \theta_n) tan\theta_n}{\sigma_n^2} = 0 \tag{F.12}$$

Assuming all the uncertainties σ_n to be equal to σ we get:

$$-b = \frac{\sum (Y_n \tan \theta_n)}{\sum \tan \theta_n^2} \tag{F.13}$$

and the uncertainty in the slope σ_b is obtained by using the error propagation formula in equation (F.13) [38]. Thus one gets:

$$\sigma_b = \frac{\sigma}{\sqrt{\sum \tan \theta_n^2}} \tag{F.14}$$

In the above equation σ is the standard deviation of the fit given by the equation:

$$\sigma^2 = \frac{1}{\nu} \sum (Y_n - f_n)^2 \tag{F.15}$$

where ν is the number of degrees of freedom given by the difference between the total number of data points and the number of parameters to be determined.

G The Global Fitting Method

In the usual fitting methods, the data D_i with errors σ_i is compared to theoretical predictions T_i from a theoretical model with unknown parameters a_i. The merit function is given as [38]:

$$\chi^2 = \sum_{i=1}^{N} \left\{ \frac{D_i - T_i}{\sigma_i} \right\}^2 \tag{G.1}$$

The best estimate for each unknown parameter a_i is obtained by minimizing the merit function with respect to each of the unknowns. If the errors are randomly distributed, then the standard statistical methods can be used to minimize χ^2 to obtain the unknowns and the associated uncertainty. However, cases arise in which above methods cannot be useful. This is especially true when the data points do not come from uniform sets of measurements, the noise of which is different in each set.

Studies have shown that in special cases, when parameters are shared amongst data sets, the accuracy can be improved [48, 49]. The sharing of a parameter is an a priori information which is fed into the fitting routine. In the case of the TRIC data, the lifetime for a specific polarization setup is assumed to be constant and so this parameter can be shared among all the relevant datasets. In the normal fitting method, one dataset is fitted to one equation and χ^2 is minimized. In the global fitting method, N datasets are fitted to N curves simultaneously (i.e., the shared parameter is optimized with respect to all the datasets and not only to a single one), and so the sum of the individual χ^2 values has to be minimized. Now for the global fitting method, the merit function becomes,

$$\chi^2 = \sum_{n=1}^{N} \chi_n^2 \tag{G.2}$$

$$\chi_n^2 = \sum_{i=1}^{m} \left\{ \frac{D_{ni} - T_{ni}(a)}{\sigma_{ni}} \right\}^2 \tag{G.3}$$

Where N is the number of datasets and m is the number of data points in each dataset. a is the shared parameter.

H Software Source Code

```
//*****************************************************************************
*************************************************
//This code was written for the development and testing stage of the TRIC data
acquisition system under Windows XP and Real Time
//Kernel RTX. The code via register programming, accesses a Meilhaus 8100
Digital Input/Output card as well as a CAMAC CC32 PCI
//controller card. The Write_CAMAC_RTX, Read_CAMAC_RTX and Read_Scalers_Twelve_RTX
functions are self contained and can be simply
//copied across and used in other programs on condition that the correct mapping
of memory and base register addressing is set up.
//The Macro:#define MAKE_CC32_OFFSET(N,A,F)  (int)((N<<10) + (A<<6) + ((F & 0xF)<<2))
 must also always be included
//
//This code has NOT been optimized as of yet and improvements can and need
 to be made for possible performance improvements
//as well as better portability as far as the functional code is concerned.
//
//More information on the function calls used and register programming can be
 found in the CAMAC and Meilhaus manuals and detailed
//information of the RTX kernel functions are also supplied in the RTX help files.
//
//Deepak Samuel samuel@iskp.uni-bonn.de
//12/8/2003
//
/*****************************************************************************
*****************************************
/Header files needed for the code. <rtapi.h> is needed for the RTX function calls
/*******************************************************************************
*****************************************
#include <windows.h>

#include <stdio.h>

#include <rtapi.h>

/*******************************************************************************
******************************************/
/Definitions used for base registers for the Meilhaus card as well as for the Camac crate
/
/*******************************************************************************
***********************************/
#define BASE_ADDR(T)        ((unsigned char *) T)        //_base_addr of Meilhaus Control
                                                         //Register this is found at run time
#define BASE_ADDR_PLX(T)  ((unsigned char *) T)        //_base_addr_PLX of Meilhaus PLX this
//is found at run time

// ME8100 register and individual bit definitions

// Registers in register sets A and B are addressed as 16 bit registers,
// so the offset is in words. The code address registers in BYTES (2x address of words)

// ME8100 Register Set A
#define ME8100_ID_REG_A(T)              ( BASE_ADDR(T) + 0x00)
#define ME8100_CONTROL_REG_A(T)         ( BASE_ADDR(T) + 0x00)
#define ME8100_RESET_INT_REG_A(T)       ( BASE_ADDR(T) + 0x02)
#define ME8100_DI_REG_A(T)              ( BASE_ADDR(T) + 0x04)
#define ME8100_DO_REG_A(T)              ( BASE_ADDR(T) + 0x06)
#define ME8100_PATTERN_REG_A(T)         ( BASE_ADDR(T) + 0x08)
#define ME8100_MASK_REG_A(T)            ( BASE_ADDR(T) + 0x0a)
#define ME8100_INT_INPUT_REG_A(T)       ( BASE_ADDR(T) + 0x0a)
// ME8100 Register Set B
```

```
#define ME8100_ID_REG_B(T)             ( BASE_ADDR(T) + 0x0c)
#define ME8100_CONTROL_REG_B(T)        ( BASE_ADDR(T) + 0x0c)
#define ME8100_RESET_INT_REG_B(T)      ( BASE_ADDR(T) + 0x0e)
#define ME8100_DI_REG_B(T)             ( BASE_ADDR(T) + 0x10)
#define ME8100_DO_REG_B(T)             ( BASE_ADDR(T) + 0x12)
#define ME8100_PATTERN_REG_B(T)        ( BASE_ADDR(T) + 0x14)
#define ME8100_MASK_REG_B(T)           ( BASE_ADDR(T) + 0x16)
#define ME8100_INT_INPUT_REG_B(T)      ( BASE_ADDR(T) + 0x16)


// ME8100 82C54 Counter Registers

// 82C54 registers are addressed as 8-bit registers, so the
// offset is in bytes.
#define ME8100_COUNTER_REG_0(T)        ( BASE_ADDR(T) + 0x18)
#define ME8100_COUNTER_REG_1(T)        ( BASE_ADDR(T) + 0x1A)
#define ME8100_COUNTER_REG_2(T)        ( BASE_ADDR(T) + 0x1C)
#define ME8100_COUNTER_CONTROL_REG(T)  ( BASE_ADDR(T) + 0x1E)


// ME8100 Bit definitions
#define ME8100_SET_SOURCE_MODE(T)    ( BASE_ADDR(T) + 0x0000) // Bit 4 To use write 0x0010
#define ME8100_INT_ON_BIT_CHANGE(T)  ( BASE_ADDR(T) + 0x0000) // Bit 5 To use write 0x0020
#define ME8100_ENABLE_INT(T)         ( BASE_ADDR(T) + 0x0000) // Bit 6 To use write 0x0040
#define ME8100_TRISTATE_OFF(T)       ( BASE_ADDR(T) + 0x0000) // Bit 7 To use write 0x0080


// PLX register and individual bit definitions

// Offset Interrupt Control/Status Register PLX
#define PLX_INTCSR(T)              (BASE_ADDR_PLX(T) + 0x4C)

// bit definitions for PLX interrupt status register
#define PLX_INT_I1_ENABLE(T)       (BASE_ADDR_PLX(T) + 0x0000) // 0x01    // Bit 0
#define PLX_INT_I1_POLARITY(T)     (BASE_ADDR_PLX(T) + 0x0000) // 0x02    // Bit 1
#define PLX_INT_I1_STATUS(T)       (BASE_ADDR_PLX(T) + 0x0000) // 0x04    // Bit 2
#define PLX_INT_I2_ENABLE(T)       (BASE_ADDR_PLX(T) + 0x0000) // 0x08    // Bit 3
#define PLX_INT_I2_POLARITY(T)     (BASE_ADDR_PLX(T) + 0x0000) // 0x10    // Bit 4
#define PLX_INT_I2_STATUS(T)       (BASE_ADDR_PLX(T) + 0x0000) // 0x20    // Bit 5
#define PLX_PCI_ENABLE(T)          (BASE_ADDR_PLX(T) + 0x0000) // 0x40    // Bit 6
#define PLX_SOFTWARE_IRQ(T)        (BASE_ADDR_PLX(T) + 0x0000) // 0x80    // Bit 7


// Offset Initialization Control Register PLX
#define PLX_ICR(T)                 (BASE_ADDR_PLX(T) + 0x50)     //Originally 0x50 but now multiplied
                                                                 //by 2 asworking in bytes not words
#define TEST_PLX(T)                (BASE_ADDR_PLX(T) + 0x3C)




// ME8100 82C54 Counter Registers
// 82C54 registers are addressed as 8-bit registers, so the
// offset is in bytes.
//#define ME8100_COUNTER_REG_0(T)        (BASE_ADDR(T) + 0x18)
//#define ME8100_COUNTER_REG_1(T)        (BASE_ADDR(T) + 0x1A)   //Registers for the Counters
  //on Meilhaus card if needed
//#define ME8100_COUNTER_REG_2(T)        (BASE_ADDR(T) + 0x1C)
//#define ME8100_COUNTER_CONTROL_REG(T) (BASE_ADDR(T) + 0x1E)


// Definitions for the CAMAC Crate

#define LCR_BASE(T)    ((USHORT)(T + 0x00009400))
#define MAKE_CC32_OFFSET(N,A,F)  (int)((N<<10) + (A<<6) + ((F & 0xF)<<2))//Macro for calculating
// the correct offset for CAMAC from NAF
#define LSR_CNTRL (LCR_BASE + 0x28)//Base address for CAMAC Control Register
#define LSR_INT  (LCR_BASE + 0x26)// Base address for CAMAC Interrupt Register


/**************************************************************************************
*************************************
/Global variables used for the code
/
/**************************************************************************************
*************************************/
```

```
UCHAR pBuffer,Int_Stat; //Pbuffer is used both in main and ISR, Int_Stat is used only in ISR
// but declared here to avoid calling it in ISR

VOID *hHandle;//Is the pointer returned from mapmemory function used in several different procedures

ULONG PLX;

ULONG CONT_REG;


ULONG Scaler_Value[1000][12];//2D array used to sort data

ULONG Scal_Result_12[12];//1D array passed to Read_Scalers_Twelve_RTX to store all 12
// values from one read of all channels

/**************************************************************************
********************************************
/FUNCTION::::to WRITE to CAMAC - Parameters: Pointer to base memory address obtained
after mapmemory call, NAF values, data to
/ write.
/
/*************************************************************************************
****************************************/
void Write_CAMAC_RTX(ULONG *BASE_MEM_CONST, int N, int A, int F, ULONG data)
{
   ULONG *BASE_MEM;
   BASE_MEM = BASE_MEM_CONST + (MAKE_CC32_OFFSET(N,A,F)/4);
      *BASE_MEM = data;
}


/***************************************************************************************
***********************************
/FUNCTION::::to READ from CAMAC - Parameters: Pointer to base memory address obtained after mapmemory
call, NAF values. returns
/read value to type ULONG
/
/***************************************************************************************
********************************/
ULONG Read_CAMAC_RTX(ULONG *BASE_MEM_CONST, int N, int A, int F)
{
   ULONG *BASE_MEM;
   ULONG Scal_Result;
   BASE_MEM = BASE_MEM_CONST + (MAKE_CC32_OFFSET(N,A,F)/4);
       Scal_Result = *BASE_MEM & 0x00FFFFFF;
   return Scal_Result;
}

/****************************************************************************************
***********************************
/FUNCTION::::to READ from all 12 scalers on CAMAC - Parameters: Pointer to base memory
address obtained after mapmemory call,
/ N value from NAF. 1D array with 12 positions passed to procedure to store read channel values.
/
/****************************************************************************************
*****************************/
void Read_Scalers_Twelve_RTX(ULONG *BASE_MEM_CONST, int N,ULONG Scal_Result[12])
{
ULONG *BASE_MEM;
int i;
for (i = 0; i<12; i++)
  {
BASE_MEM = BASE_MEM_CONST + (MAKE_CC32_OFFSET(N,i,0)/4);
       Scal_Result[i] = *BASE_MEM & 0x00FFFFFF;
  }
}
/***************************************************************************************
********************************
/FUNCTION::::Interupt Service Thread(IST). This function is called on response to interrupt from
 the Meilhaus card,
```

```
//NULL passed
/********************************************************************************
*******************************/
BOOLEAN RTFCNDCL InterruptHandler(PVOID past)
{
        int i;
    Write_CAMAC_RTX(hHandle, 22, 0, 16, 0xff);
        Read_Scalers_Twelve_RTX(hHandle, 20, Scal_Result_12);
    for (i = 0; i<12; i++)
{
    if (Scal_Result_12[i]<1000) //To prevent data overflow and thread crash due to limited
     //size of data structure
{ Scaler_Value[Scal_Result_12[i]][i] = Scaler_Value[Scal_Result_12[i]][i] + 1;
}
}
        Read_CAMAC_RTX(hHandle, 20, 11, 2);
    Write_CAMAC_RTX(hHandle, 22, 0, 16, 0x0);
    return TRUE;
}


/**********************************************************************
********************************************************/
/ FUNCTION::::Interupt Service Routine(ISR). This function is called to determine
 which hardware device on a shard interrupt
//line generated the interrupt and then calls the corresponding IST, NULL passed
/**********************************************************************
*************************************************/
INTERRUPT_DISPOSITION RTFCNDCL Isr_ME (PVOID past)
{
Int_Stat = RtReadPortUchar(PLX_INTCSR(PLX));
Int_Stat = Int_Stat && 0x00000024;
if(Int_Stat != 0){
pBuffer = RtReadPortUchar(ME8100_RESET_INT_REG_A(CONT_REG));
return CallInterruptThread;
}
else
return PassToNextDevice;
}


/********************************************************************************
********************************************/
/ FUNCTION:::Main Function
/********************************************************************************
********************************************/
int main( int argc, PCHAR *argv )
{

//*******************************
//Local variables to Main function
//*******************************

HANDLE interrupt;

ULONG sn; // logical slot number for the PCI adapter

ULONG f; // function number on the specified adapter

ULONG bytesWritten; // return value from RtGetBusDataByOffset

ULONG bus; // bus number

BOOLEAN flag;

LARGE_INTEGER BAR0; // base port address of the MITE quadpart of LARGE_INTEGER used

LARGE_INTEGER BAR1; // base port address of the board registers quadpart of LARGE_INTEGER used

int i,j;//index for read loop for scaler
```

```
ULONG IrqLevel; // interrupt level

ULONG IrqVectr; // interrupt vector

ULONG intbusnumb; // Interrupt bus number

PCI_SLOT_NUMBER SlotNumber;

PPCI_COMMON_CONFIG PciData;// data structure to hold PCI card information see MSDN for declarations

UCHAR buffer[PCI_COMMON_HDR_LENGTH];

BOOLEAN Release;// return variable for released Interrupt vector procedure call

LARGE_INTEGER physAddr;//Conatins address space to be mapped.

ULONG Length = 0x88b8; //32K size of mapped memory
//********************************
//Initialization of local variables
//********************************

BAR0.QuadPart = 0;

BAR1.QuadPart = 0;

PciData = (PPCI_COMMON_CONFIG) buffer;

SlotNumber.u.bits.Reserved = 0;

flag = TRUE;

//*********************************************************************************************

// Search for the Meilhaus Card and CAMAC PCI Card. Here correct base addresses for registers are found

//*********************************************************************************************

for (bus = 0; flag; bus++)
{

for (sn = 0; sn < PCI_MAX_DEVICES && flag; sn++)

 {

    SlotNumber.u.bits.DeviceNumber = sn;

    for (f = 0; f < PCI_MAX_FUNCTION; f++)

    {
 SlotNumber.u.bits.FunctionNumber = f;

 bytesWritten = RtGetBusDataByOffset (PCIConfiguration, bus, SlotNumber.u.AsULONG, PciData, 0,PCI_COMMON_HDR_LENGTH );

 if (bytesWritten == 0)

{

flag = FALSE;  // out of PCI buses

break;

}

if (PciData->VendorID == PCI_INVALID_VENDORID)

{
// no device at this slot number, skip to next slot

break;
```

```
}

82

//*****************************************************************

// A device is found, if this is our card, then

// print out all the PCI configuration information to screen

// and set the variables.

//*****************************************************************

if (((PciData->VendorID == 0x1402) && (PciData->DeviceID == 0x810B))

            || ((PciData->VendorID == 0x10B5) && (PciData->DeviceID == 0x2258)))
            //For the Meilhaus card and  //CAMAC

{

// Set IRQ values for attaching interrupt below

IrqLevel = PciData->u.type0.InterruptLine; // interrupt level

IrqVectr = IrqLevel; // interrupt IRQ

// Put the BusAddresses into other variables

BAR0.QuadPart = PciData->u.type0.BaseAddresses[0];

// MITE address

BAR1.QuadPart = PciData->u.type0.BaseAddresses[1];

// new board address

intbusnumb = bus;

if ((PciData->VendorID == 0x1402) && (PciData->DeviceID == 0x810B))

            {
 printf("Meilhaus 8100:\n");
}

else

{

            if ((PciData->VendorID == 0x10B5) && (PciData->DeviceID == 0x2258))

            {
 printf("CAMAC PCI:\n");
}

else printf("Other PCI device:\n");

}

printf("---------------------------------------\n");

printf("BusNumber:\t\t%d\n", bus);

printf("DeviceNumber:\t\t%d\n", sn);

printf("FunctionNumber:\t\t%d\n", f);

printf("VendorID:\t\t0x%x\n", PciData->VendorID);

printf("DeviceID:\t\t0x%x\n", PciData->DeviceID);
```

```
printf("Command:\t\t0x%x\n", PciData->Command);

printf("Status:\t\t\t0x%x\n", PciData->Status);

printf("RevisionID:\t\t0x%x\n", PciData->RevisionID);

printf("ProgIf:\t\t\t0x%x\n", PciData->ProgIf);

printf("SubClass:\t\t0x%x\n", PciData->SubClass);

printf("BaseClass:\t\t0x%x\n", PciData->BaseClass);

printf("CacheLineSize:\t\t0x%x\n", PciData->CacheLineSize);

printf("LatencyTimer:\t\t0x%x\n", PciData->LatencyTimer);

printf("HeaderType:\t\t0x%x\n",PciData->HeaderType);

printf("BIST:\t\t\t0x%x\n", PciData->BIST);

printf("BaseAddresses[0]:\t0x%08x\n",PciData->u.type0.BaseAddresses[0] & 0xFFFFFFF0);

printf("BaseAddresses[1]:\t0x%08x\n",PciData->u.type0.BaseAddresses[1] & 0xFFFFFFF0);

printf("BaseAddresses[2]:\t0x%08x\n",PciData->u.type0.BaseAddresses[2] & 0xFFFFFFF0);
//Mask out first bit for all  addresses as always 1 to big

printf("BaseAddresses[3]:\t0x%08x\n",PciData->u.type0.BaseAddresses[3] & 0xFFFFFFF0);

printf("BaseAddresses[4]:\t0x%08x\n",PciData->u.type0.BaseAddresses[4] & 0xFFFFFFF0);

printf("BaseAddresses[5]:\t0x%08x\n",PciData->u.type0.BaseAddresses[5] & 0xFFFFFFF0);

printf("ROMBaseAddress:\t\t0x%08x\n",PciData->u.type0.ROMBaseAddress);

printf("InterruptLine:\t\t%d\n",PciData->u.type0.InterruptLine);

printf("InterruptPin:\t\t%d\n",PciData->u.type0.InterruptPin);

printf("MinimumGrant:\t\t%d\n",PciData->u.type0.MinimumGrant);

printf("MaximumLatency:\t\t%d\n",PciData->u.type0.MaximumLatency);

printf("\n");
if ((PciData->VendorID == 0x10B5) && (PciData->DeviceID == 0x2258))
{
  physAddr.QuadPart = PciData->u.type0.BaseAddresses[3] & 0xFFFFFFF0;

}   //The address of the physical memory to
    //map to process space. Stored in QuadPart
    //of LARGE_INTEGER always obtained from BaseAddresses[3]

                      if ((PciData->VendorID == 0x1402) && (PciData->DeviceID == 0x810B))
{
  PLX = PciData->u.type0.BaseAddresses[1] & 0xFFFFFFF0;
  CONT_REG = PciData->u.type0.BaseAddresses[2] & 0xFFFFFFF0;
}
}// dio 96

 } // max_function

} // max_devices
} // flag
//*********************************************************
////Initilization of data structure for stored scaler values
//*********************************************************
for (i = 0; i<= 999; i++)
{
for (j = 0; j<= 11; j++)
```

```
{
   Scaler_Value[i][j] = 0;
}
}
//********************************************************************
// Initilization stage of Meilhaus card as well as CAMAC crate
//********************************************************************
RtEnablePortIo((PUCHAR)LCR_BASE(0),0xea807fff);

RtWritePortUshort(((PUSHORT) LCR_BASE(0x50)), 0x4186);//Initilization of control register CAMAC

hHandle = RtMapMemory(physAddr, Length, TRUE);//Maps the physical memory to
// address space a Handle to mapped memory returned

Write_CAMAC_RTX(hHandle, 31, 0, 0, 0x0);//Reset of CAMAC

Write_CAMAC_RTX(hHandle, 0, 0, 0, 0x0);//CAMAC clear

Write_CAMAC_RTX(hHandle, 0, 1, 0, 0x0);//CAMAC Initialize

Write_CAMAC_RTX(hHandle, 30, 2, 0, 0x0c00);//CAMAC fast access for station N24..N17

Write_CAMAC_RTX(hHandle, 30, 0, 0, 0x00c0);//CAMAC fast access for station N8..N1

RtEnablePortIo(BASE_ADDR(CONT_REG),1280);//Set range of ports that can be used

pBuffer = RtReadPortUchar(ME8100_RESET_INT_REG_A(CONT_REG));

RtWritePortUchar(ME8100_TRISTATE_OFF(CONT_REG), 0x90);

RtWritePortUchar(ME8100_ENABLE_INT(CONT_REG) , 0xD0);

RtWritePortUchar(ME8100_PATTERN_REG_A(CONT_REG), 0x01);

RtWritePortUchar(ME8100_MASK_REG_A(CONT_REG) , 0x00);

RtWritePortUchar(PLX_INTCSR(PLX), 0x43); // Here we have set PLX_I1_STATUS,
// I2_ENABLE, I2_STATUS and PCI_ENABLE to HIGH

pBuffer = RtReadPortUchar(PLX_INTCSR(PLX));

printf("RESPONDING TO INTERRUPTS\n");

Write_CAMAC_RTX(hHandle, 22, 0, 26, 0xff);//Activate output CAMAC Cassette
Write_CAMAC_RTX(hHandle, 22, 0, 16, 0x0);//Initialize output to zero
Write_CAMAC_RTX(hHandle, 20, 11, 9, 0xff);//Clear scalers
Write_CAMAC_RTX(hHandle, 20, 0, 24, 0xff);//Disable Look-At-Me scalers

//******************************************************************************************
//RtAttachInterruptVectorEx attaches the correct vector to the interrupt of the Meilhaus card.
//Creates background child thead with maximum priority
//******************************************************************************************
interrupt = RtAttachInterruptVectorEx(NULL,0,InterruptHandler,NULL,RT_PRIORITY_MAX,2,intbusnumb,I
rqLevel,IrqVectr, TRUE, LevelSensitive, Isr_ME);

if( interrupt == NULL)
{
printf("Could not register interrupt handler\n");
}

//******************************************************************************************
//Sets output bit high and then low to start interrupt generation
//******************************************************************************************
Write_CAMAC_RTX(hHandle, 22, 0, 16, 0xff);//Set output high
     //The high and low starts the interrupt cycle
Write_CAMAC_RTX(hHandle, 22, 0, 16, 0x0); //Set output low
Sleep(40000);//Parent thread to sleep

Release = RtReleaseInterruptVector(interrupt);//Release interrupt vector for Meilhaus card
```

```
for (i = 0; i<=60 ; i++)
{
    if (i%5 == 0)
{
     printf("\n");
}
    printf("%02d  ",i);
        for (j = 0; j< 12; j++)
{
       printf(" %07d",Scaler_Value[i][j]);//Print to screen of stored scaler values
}
printf("\n");
}              printf("I AM AT THE END\n\n");
           return 0;
}//end of main
```

Bibliography

[1] G. Lüders, Annals of Physics **2**, 1 (1957).

[2] J. Schwinger, Proc Natl Acad Sci U S A. **44**, 223 (1958).

[3] W. Pauli, L. Rosenfeld, and V. Weisskopf, *Niels Bohr and the Development of Physics*, McGraw-Hill Newyork, 1955.

[4] C. S. Wu, E. Ambler, R. W. Hayward, D. D. Hoppes, and R. P. Hudson, Phys. Rev. **105**, 1413 (1957).

[5] M. Gell-Mann and A. Pais, Phys. Rev. **97**, 1387 (1955).

[6] A. D. Sakharov, Zhurnal Eksperimental noi i Teoreticheskoi Fiziki **76**, 1172 (1979).

[7] G. R. Farrar, Nuclear Physics B Proceedings Supplements **43**, 312 (1995).

[8] N. Ramsey, Phys. Rep **43**, 409 (1978).

[9] N. Ramsey, Ann. Rev. Nucl. Sci (1982).

[10] S. Lamoreaux, Nuclear Instruments and Methods in Physics Research A **284**, 43 (1989).

[11] A. Angelopoulos et al., First direct observation of time-reversal violation, in *American Institute of Physics Conference Series*, volume 549, pages 957–960, 2000.

[12] J. W. Cronin, Rev. Mod. Phys. **53**, 373 (1981).

[13] E. D. Commins, S. B. Ross, D. DeMille, and B. C. Regan, Phys. Rev. A **50**, 2960 (1994).

[14] D. Cho, K. Sangster, and E. A. Hinds, Phys. Rev. A **44**, 2783 (1991).

[15] M. Beyer, Nuclear Physics A **560**, 895 (1993).

[16] M. Simonius, Physics Letters B **58**, 147 (1975).

[17] W. C. Haxton and A. Höring, Nuclear Physics A **560**, 469 (1993).

[18] H. E. Conzett, Phys. Rev. C **52**, 1041 (1995).

[19] P. D. Eversheim et al., Physics Letters B **256**, 11 (1991).

[20] F. Arash, M. J. Moravcsik, and G. R. Goldstein, Phys. Rev. Lett. **54**, 2649 (1985).

[21] H. E. Conzett, Phys. Rev. C **48**, 423 (1993).

[22] J. Bystricky, F. Lehar, and P. Winternitz, J. Phys. (France) **39**, 1 (1978).

[23] G. G. Ohlsen, Rep. Prog. Phys. **35**, 717 (1972).

[24] P. R. Huffman et al., Phys. Rev. C **55**, 2684 (1997).

[25] M. Beyer, Nuclear Physics A **493**, 335 (1989).

[26] N. K. Cheung, H. E. Henrikson, and F. Boehm, Phys. Rev. C **16**, 2381 (1977).

[27] C. F. Hwang, T. R. Ophel, E. H. Thorndike, and R. Wilson, Phys. Rev. **119**, 352 (1960).

[28] E. Blanke et al., Phys. Rev. Lett. **51**, 355 (1983).

[29] V. E. Bunakov, Phys. Rev. Lett. **60**, 2250 (1988).

[30] Y. Yamaguchi, J. Phys. Soc. Jpn. **57**, 1518 (1988).

[31] P.D.Eversheim, *Proposal for Measurement of the Total Correlation Coefficient $A_{y,y}$ by the TRIC Collaboration.*

[32] M. Glende, *Die Speicherzelle für das EDDA-und das TRI-Experiment am Cooler Synchrotron COSY-Jülich*, PhD thesis, University of Bonn, 2000.

[33] M. Altmeier, *Die Entwicklung und der Bau des polarisierten Wasserstoffatom-strahlteils für das EDDA-Experiment an COSY-Jülich*, PhD thesis, University of Bonn, 1998.

[34] K. Unser, CERN SL/91-42 (1991).

[35] M. Blumenthal, Improvements of a precision voltage to frequency converter system and the developments of a real-time data acquisition system under windows xp, Master's thesis, University of Bonn, 2003.

[36] `http://www.windowsitpro.com/Article/ArticleID/4500/4500.html`.

[37] A. Peters, H. Schmickler, and K. Wittenburg., Proceedings of Workshop on DC Current Transformers and Beam-Lifetime Evaluations, 2004.

[38] P. Bevington and K. Robinson, *Data Reduction and Error Analysis for the Physical Sciences*, McGraw-Hill, 2000.

[39] F. Perrot et al., Nuclear Physics B **278**, 881 (1986).

[40] F. Hinterberger and D. Prasuhn, Nuclear Instruments and Methods in Physics Research A **279**, 413 (1989).

[41] F. Hinterberger, T. Mayer-Kuckuk, and D. Prasuhn, Nuclear Instruments and Methods in Physics Research A **275**, 239 (1989).

[42] P. Bak, C. Tang, and K. Wiesenfeld, Phys. Rev. Lett. **59**, 381 (1987).

[43] P. J. Cote and L. V. Meisel, Phys. Rev. Lett. **67**, 1334 (1991).

[44] P. Cizeau, S. Zapperi, G. Durin, and H. E. Stanley, Phys. Rev. Lett. **79**, 4669 (1997).

[45] O. Narayan, Phys. Rev. Lett. **77**, 3855 (1996).

[46] A. S. Edelstein and G. A. Fischer, Journal of Applied Physics **91**, 7795 (2002).

[47] William H. Press, Brian P. Flannery, Saul A. Teukolsky, and William T. Vetterling, *Numerical recipes in C*, Cambridge University Press, 1993.

[48] J. Pumplin, D. R. Stump, and W. K. Tung, Phys. Rev. D **65**, 014011 (2002).

[49] S. Pelet, M. J. R. Previte, L. H. Laiho, and P. T. C. So, Biophys. J. **87**, 2807 (2004).

[50] R. E. Pollock et al., Nuclear Instruments and Methods in Physics Research A **330**, 380 (1993).

[51] Paetz gen.Schieck, *Lecture Notes on Nuclear Physics with Polarized Particles*, University of Cologne, Germany, 2004.

Acknowledgments

I owe much to many. Dr.Dieter Eversheim, my "Doktorvater" has been an excellent mentor providing consistently good advice and helpful criticisms. He has been instrumental in improving and honing my scientific skills and I am thankful for his friendly and caring attitude and his gentle approach in times of trouble.

I thank Prof.Dr.K.Maier for kindly accepting to be the co-referee of this work and for devoting his time to read my thesis.

I thank the Forschungszentrum Jülich for all their support offered for my research work. I would also like to thank the COSY crew for their suppport offered from the technical and accelerator side of the experiment. Dr.Olaf Felden and Dr.Ralph Gebel deserve special mention for their assistance during our beam time and in running the remote version of our data acquisition system.

I thank the committee members of the Bonn International Graduate School for accepting my application to the graduate school and for the wonderful assistance provided during my initial days in Bonn.

I had spent a significant part of my life in the serene campus of the Madras Christian College School, the place that nurtured me with all goodness of life. Dr.Clement J. Felix, former Head Master and Correspondent of the MCC School, has been a great inspiration right from my childhood. I have always admired his impeccable command over the English language. I consider myself to be fortunate for having been educated by wonderful teachers in my life so far. I would specially like to acknowledge my teachers Mr.Mytran, Dr.P.Chandran and Dr.Samuel Cornelius for the impact they made in my life.

Bonn has been a very delightful place to live and work. It has introduced me to new friends and to an entirely different lifestyle. Mrs&Mr. Chandran Tucker were an awesome host and I cherish the time I spent with them. Saravanan and Preethi, people without whom my days in Bonn would not have been enjoyable, deserve more than just an acknowledgment. I am truly proud of my dear friends N.S.Anand, Rajiv, Santhosh and Shincy and my loving sister Daisy and I am thankful for their love and support. I am also thankful to my uncle Yesupatham and his family for their timely help and for their encouragement.

I thank God for his abundant blessings and I would like to thank the members of the church for keeping me in their prayers. My parents Clarence and Pushpa shoulder most of the blame for my being who I am.

Curriculum Vitae

Personal Data

Name	:	Deepak Samuel
Nationality	:	Indian.
		e-mail: deepaksamuel@gmx.de

Academic Profile

- **Helmholtz Institut für Strahlen- und Kernphysik**   Bonn,Germany
  Ph.D Physics   *Sep 2002-Dec 2007*
  - Research Work: Test of Feasibility of a Novel High Precision Test of Time Reversal Invariance
  - Research Supervisor: P.D.Dr.Dieter Eversheim

- **Madras Christian College**   Chennai, India
  M.Phil Physics   *Aug 2001- Sep 2002*
  - Project Work: *Ab-initio* molecular orbital calculations on group III elements and their halides
  - Research Supervisor: Prof.Dr.P.Chandran

- **Madras Christian College**   Chennai, India
  M.Sc Physics   *Jun 1999- May 2001*
  - Project Work: Self Consistent Field theory calculations on Boron Halides
  - Research Supervisor: Prof.Dr.P.Chandran

- **Madras Christian College**   Chennai, India
  B.Sc Physics   *Jun 1996- May1999*

- **Madras Christian College Higher Secondary School**   Chennai, India
  Schooling   *Jun 1989- May1996*